Loss of Profilin3 Impairs Spermiogenesis by Affecting Acrosome Biogenesis, Autophagy, Manchette Development and Mitochondrial Organization

PFN4 is Required for Acrosome Biogenesis by Regulating Autophagy through PI3K/AKT/mTOR Pathway

Dissertation

zur

Erlangung des Doktorgrades (Dr.rer.nat.)

der

Mathematisch-Naturwissenschaftlichen Fakultät

der

Rheinischen Friedrich-Wilhelms-Universität Bonn

vorgelegt von

Naila Tariq

aus

Lahore, Pakistan , 2022

2022

Angefertigt mit Genehmigung der Mathematisch-Naturwissenschaftlichen Fakultät der Rheinischen Friedrich-Wilhelms-Universität Bonn

1. Gutachter: Prof. Dr. Hubert Schorle

2. Gutachter: Prof. Dr. Walter Witke

Tag der Promotion: 26.10.2022

Erscheinungsjahr: 2022

STATEMENT OF AUTHORSHIP

The content of this Ph.D. thesis is my original work, and has been generated in the Institute of Pathology, Uniklinikum Bonn at AG Schorle research group and was funded by Deutscher Akademischer Austauschdienst (DAAD).

Supervisor : Prof. Dr. Hubert Schorle

Department of Developmental Pathology

Institute of Pathology, Uniklinikum Bonn

Venusberg Campus 1, Building 62

53127, Bonn, Germany

Tel: +49 228 287 16341

Email: Schorle@uni-bonn.de

I hereby declare that

1) this has been written by myself under supervision and describe my own work unless otherwise stated.
2) Present work has not been submitted as a dissertation at any other university

Date and place Signature

Part of this work has been already published in the following Publication using my maiden name (Umer):

Umer, N., Arévalo, L., Phadke, S., Lohanadan, K., Kirfel, G., Sons, D., Sofia, D., *et al.* (2021), "**Loss of Profilin3 Impairs Spermiogenesis by Affecting Acrosome Biogenesis, Autophagy, Manchette Development and Mitochondrial Organization**", *Frontiers in Cell and Developmental Biology*, Vol. 9, available at: https://doi.org/10.3389/fcell.2021.749559.

ACKNOWLEDGEMENT

I would like to take the opportunity to express my gratitude to all those who have helped and encouraged me during the process and writing of my Ph.D. and the thesis. The completion of this work could have not been possible without the participation, help and support of so many people whose names may not all be enumerated. Your contributions are sincerely highly appreciated and gratefully acknowledged.

Above all, I would like to thank my doctoral supervisor Prof. Dr. Hubert Schorle for his supervision, guidance, and support in professional and personal, throughout my journey. I want to express my gratitude for having believe in me from beginning till I am done with my research work. I also would like to thank you for helping and boosting confidence in me during my presentations in conferences and seminars and in writing skills.

I also would like to thank Prof. Dr. Walter Witke for friendly readiness of my publication and report of my work. I would also like to thank Gregor Kirfel for proof reading of publication and successful collaboration. I would like to thank Prof. Dr. Gabriel Schaaf and PD. Dr. Gregor Kirfel for to be the part of the examination committee as external reviewers.

I am grateful to Dr. Lena Arevalo for advising me during my research work and always there to help me in solving the problems and giving me new ideas to implement strategies in research and writing. I am also thankful to all current and former lab members. I am highly obliged to Angela Egert, Andrea Jäger for their endless support in generating and establishing knockout mice and always there to assist me during my animal experiments, without which half of this work would not have been possible. I am thankful for Gaby Beine and Susanne Steiner for their technical help.

In addition, I am thankful to Marc Sylvester, Farhad Shakeri and Andreas Bunnes, members of core facility, Uniklinikum Bonn for helping me in mass spectrometry and data analysis.

I am highly thankful to Deutscher Akademischer Austauschdienst (DAAD) to select me for doctoral grant to support my Ph.D and Boehringer Ingelheim Fonds (BIF) for the travel grant for the initiation of my Ph.D.

Last but not least would like to thank my family especially my mother for her guidance, support, motivation and endless sacrifice during my carrier, my husband to keep me encouraged in my writing phase and my friends, who always had an open ear for me outside of the work group and supported me during this challenging time.

LIST OF ABBREVATIONS

ADF	Actin depolymerizing Factor
AKT	Protein kinase B
AMPK	AMP-activated protein kinase
AR	Acrosomal reaction
CFL-1	Cofilin 1
CFL-2	Cofilin 2
CRISPR	Clustered Regularly Interspaced Short Palindromic Repeats
DSB	Double strand breaks
FS	Fibrous sheath
HDR	Homology driven repair
HRP	Horse reddish peroxidase
IHC	Immunohistochemistry
IP	Immune-precipitation
LC3B	Microtubule-associated proteins 1A / 1B light chain 3A
LRO	Lysosomal related organelle
MS	Mass spectrometry
mTOR	mechanistic target of rapamycin
NHEJ	Non-homologous end joining
ODF	Outer dense fiber
PAM	Protospacer adjacent motive
PAS	Post acrosomal sheath
PFNs	Profilins
PI3K	Phosphoinositide 3-kinases
PT	Perinuclear theca
qRT-PCR	Quantitative real time polymerase chain reaction
SC	Sertoli cells
SQSTM1	Sequestosome 1
STD	Sexually transmitted disease
TSC	Total sperm count

Table of Contents

Loss of Profilin3 Impairs Spermiogenesis by Affecting Acrosome Biogenesis, Autophagy, Manchette Development and Mitochondrial Organization I

PFN4 is Required for Acrosome Biogenesis by Regulating Autophagy through PI3K/AKT/mTOR Pathway I

STATEMENT OF AUTHORSHIP I

ACKNOWLEDGEMENT III

LIST OF ABBREVATIONS V

LIST OF FIGURES X

LIST OF TABLES XIII

SUMMARY I XIV

SUMMARY II XV

1. INTRODUCTION 1

1.1 Male fertility 1

1.2 Spermatogenesis 1

1.2.1 Acrosome biogenesis 2

1.2.2 Development of the manchette and nuclear shaping 4

1.2.3 Sperm tail formation 5

1.3 The role of sperm in fertilization 6

1.3.1 Zona pellucida binding induces the sperm to undergo an Acrosome reaction…. ..... ……..7

1.4 The role of autophagy in acrosome biogenesis 7

1.5 Role of Golgi network in acrosome biogenesis 9

1.6 Actin cytoskeleton 11

1.7 Profilins 11

1.7.1 The Profilin family 12

1.8 Single-cell transcriptome analysis of *Pfn3* and *Pfn4* 13

1.9 Genome editing 14

1.9.1 Use of guided nuclease to generate genetically modified mice 14

2. MATERIALS 15

2.1 Chemicals and Reagents 15

2.2 Buffers and Solutions 18

2.3 Kits 20

2.4 Equipment 21

2.5 Consumables 24
2.6 Primers 25
2.6.1 Genotyping Primers 25
2.6.2 sgRNAs 25
2.6.3 qRT Primers 26
2.6.4 Sequencing primers 27
2.7 Medium 27
2.8 Enzymes 28
2.9 Animals 28
2.10 Antibodies 29
2.10.1 Primary antibodies 29
2.10.2 Secondary antibodies 30
2.11 Software 31
3. METHODS 33
3.1 Animal Experiments 33
3.1.1 Ethics 33
3.1.2 Generation of Transgenic Mice 33
3.1.3 Fertility analysis 34
3.1.4 Morphological analysis 34
3.1.5 In-vitro fertilization (IVF) 34
3.1.6 Isolation of Germ cell population from testes 34
3.2 Histochemical Methods 35
3.2.1 Tissue fixation 35
3.2.2 Hematoxylin and Eosin (H&E) staining 35
3.3 Biochemical Methods 35
3.3.1 BCA Assay 35
3.3.2 Pierce Assay 36
3.3.3 SDS-PAGE 36
3.3.4 Western Blot 37
3.3.5 Immunodetection 37
3.3.6 Immunolabelling and Microscopy 38
3.3.7 Mass Spec Analysis 41
3.4 Molecular Biology Methods 43

3.4.1 Cloning 43
3.4.2 Total DNA preparation 44
3.4.3 Agarose gel electrophoresis 45
3.4.4 RNA extraction 46
3.4.5 Protein extraction 46
3.4.6 Polymerase chain reaction 46
3.4.7 cDNA synthesis 48
3.4.8 qRT PCR 48
3.5 Semen analysis 49
3.5.1 Sperm isolation 49
3.5.2 Hypoosmotic swelling test 50
3.5.3 Eosin-Nigrosin staining 50
3.5.4 Sperm motility analysis 50
3.5.5 Nuclear Morphology analysis 50
3.6 Sequencing 51
3.6.1 Sanger sequencing 51
3.6.2 RNA seq analysis 51
3.7 Statistics 52
4. RESULT I 53
4.1 Ultrastructural analysis of PFN3 localization in mouse testes 53
4.2 *Pfn3* deficient male mice display sub-fertility and low sperm quantity and quality 57
4.3 Sperm head morphology is altered in *Pfn3* deficient mice 60
4.4 Sperm motility is reduced in *Pfn3* deficient mice 61
4.5 Impaired acrosome biogenesis in *Pfn3* deficient mice 62
4.6 Significant decrease of acrosome reacted sperm in *Pfn3* deficient mice 64
4.7 Disrupted Golgi network in *Pfn3* deficient mice 65
4.8 RNA-Seq revealed alterations in expression levels of germ cell development related genes in *Pfn3*$^{-/-}$ mice 67
4.9 Autophagic flux and AMPK/mTOR signaling pathway are affected in *Pfn3* deficient mice 68
4.10 PFN3 interacts with TRIM27 70
4.11 *Pfn3* deficient mice exhibit increased protein levels of ADF/CFL variants compared to WT 71
4.12 PFN3 binding protein is lost in nuclear fraction of sperm 72

4.13 F-Actin organization is not altered in *Pfn3* deficient sperm 73

4.14 Abnormal manchette development in *Pfn3* deficient mice..... 73

4.15 *Pfn3* deficient sperm display flagellar deformities..... 74

5. DISCUSSION I 77

6. RESULT II 83

6.1 Generation and phenotypic characterization of PFN4-deficient mouse lines…….. 83

6.2 Loss of PFN4 results in aberrant sperm nuclear morphology..... 88

6.3 Defective manchette development in *Pfn4*$^{-/-}$ mice..... 88

6.4 Flagellar defects in *Pfn4*$^{-/-}$ sperm 92

6.5 Reduced sperm motility in *Pfn4*$^{-/-}$ mice..... 93

6.6 PFN4 is essential for acrosome biogenesis 94

6.7 Loss of *Pfn4* resulted in fragmented Golgi network 99

6.8 Disrupted PI3K/AKT and AMPK/mTOR signaling pathways leads to inhibited autophagy in *Pfn4*$^{-/-}$ mice..... 101

6.9 Acrosomal reaction significantly reduced in *Pfn4*$^{-/-}$ sperm..... 105

6.10 *Pfn4* deficient sperm are able to fertilize zona-free oocytes..... 106

6.11 Actin cytoskeletal organization is normal in *Pfn4*$^{-/-}$ seminiferous epithelium..... 106

6.12 Apoptosis and phagocytosis are not observed in *Pfn4*$^{-/-}$ mice..... 107

7. DISCUSSION II..... 109

8. REFERENCES 114

LIST OF FIGURES

Figure 1: Spermatogenesis in the testes..…….2

Figure 2: Process of acrosome biogenesis: the Golgi, Cap, acrosomal, and maturation Phases…….……...3

Figure 3: Development of the manchette during spermatogenesis……..5

Figure 4: Development of sperm flagellum during mouse spermiogenesis……6

Figure 5: Sperm acrosome reaction…….7

Figure 6: The process of autophagy…….....9

Figure 7: Role of Golgi network in acrosome biogenesis……..10

Figure 8: Localization of PFN3 and PFN4 to the acroplaxome-manchette complex in Spermatids……...12

Figure 9: Single-cell RNA-Seq captures a continuum of germ cell-types…….13

Figure 10: Immunogold labelling using PFN3 antibody on testes sections...……57

Figure 11 : PFN3-Deficient mice generation and establishment……..…….59

Figure 12: Amorphous nuclear morphology of sperm cells in *Pfn3* deficient mice..61

Figure 13: Impaired acrosome biogenesis in *Pfn3* deficient mice…..……64

Figure 14: The acrosomal reaction (AR) using calcium ionophore……...65

Figure 15: *Cis*-and *trans*-Golgi staining on testes sections……....66

Figure 16: Changes in gene expression profile of *Pfn3* deficient mice……..68

Figure 17: Disruption in autophagic flux and AMPK/MTOR signaling pathway of *Pfn3* deficient mice……...70

Figure 18: Co-immunoprecipitation using anti-PFN3 and anti-TRIM27 antibody on testis lysates……..71

Figure 19: Immunoblotting against ADF, CFL1 and CFL2 on protein lysates from

Pfn3$^{+/+}$, *Pfn3*$^{+/-}$ and *Pfn3*$^{-/-}$ testes…….72

Figure 20: Western blot analysis and IHC (immunohistochemical analysis) was performed using anti-ARPM1 antibody……..72

Figure 21: Stimulated emission depletion (STED) microscopy……73

Figure 22: Manchette structure stained by using α-tubulin antibody……74

Figure 23: Flagellum analysis on mature sperm cells……...75

Figure 24: Working hypothesis on the PFN3 role in acrosome biogenesis……..81

Figure 25: Generation and characterization of PFN4-deficient mice……...85

Figure 26: Histological analysis on PFN4-deficient mice……87

Figure 27: Nuclear morphology analysis on WT, *Pfn4*$^{+/-}$ and *Pfn4*$^{-/-}$ sperm cells....88

Figure 28: Immunofluorescence staining for manchette using α-tubulin antibody (green) on germ cell population……..93

Figure 29: Flagellar staining and ultrastructural analysis using MitoRed, TEM, and SEM on WT, *Pfn4*$^{+/-}$ and *Pfn4*$^{-/-}$ sperm……...…96

Figure 30: Immunofluorescence staining and PAS staining for acrosome biogenesis on testes sections and mature sperms of WT, *Pfn4*$^{+/-}$ and *Pfn4*$^{-/-}$ mice…98

Figure 31: Ultrastructural analysis using TEM on testes sections of WT, *Pfn4*$^{+/-}$ and *Pfn4*$^{-/-}$ mice……...101

Figure 32: *Cis*-and *trans*-Golgi immunofluorescence staining using GM130 (green) and TGN46 (green) antibody……104

Figure 33: Mass spectrometry and western blot analyses……...105

Figure 34: The acrosomal reaction (AR) using calcium ionophore WT, *Pfn4*$^{+/-}$ and *Pfn4*$^{-/-}$ sperm cells……106

Figure 35: In-vitro fertilization performed on zona free oocytes with WT and *Pfn4*$^{-/-}$ Sperms……107

Figure 36: Phalloidin Staining on testes sections of WT, *Pfn4*$^{+/-}$ and *Pfn4*$^{-/-}$ mice.

……..108

Figure 37: Apoptosis and phagocytosis analysis…….109

LIST OF TABLES

Table 1 : Chemicals and reagents used in this study…….……15

Table 2 : Buffers and Solutions used in this study…….……18

Table 3: Kits used in this study…….……..20

Table 4: Equipment used in this study……..……..21

Table 5: Materials used in this study…….…….24

Table 6: Genotyping Primers used in this study…….25

Table 7: Single guide RNAs used in this study…….…….25

Table 8: qRT Primers used in this study…….26

Table 9: Sequencing primers used in this study……..27

Table 10: Medium used in this study…….....27

Table 11: Enzymes used in this study…….....28

Table 12: Animals used in this study……..……....28

Table 13: Antibodies used in this study……. 29

Table 14: Software used in this study…….31

Table 15 : Components for a small SDS Polyacrylamide gel…….36

Table 16: PCR reaction mixture……..46

Table 17: Genotyping PCRs……...47

Table 18: DNase I digest mixture……48

Table 19: qRT PCR reaction mixture……..49

Table 20 : qRT PCR program cycling conditions……...49

Table 21: Motility parameters…….61

Table 22: Motility parameters…….....94

SUMMARY I

Profilins (PFNs) are key regulatory proteins for the actin polymerization in cells and are encoded in mouse and humans by four *Pfn* genes. PFNs are involved in cell mobility, cell growth, neurogenesis, and metastasis of tumor cells. The testes-specific PFN3 is localized in the acroplaxome–manchette complex of developing spermatozoa. I demonstrate that PFN3 further localizes in the Golgi complex and proacrosomal vesicles during spermiogenesis, suggesting a role in vesicle transport for acrosome formation. Using CRISPR/Cas9 genome editing, I generated mice deficient for *Pfn3*. *Pfn3*$^{-/-}$ males are sub-fertile, displaying a type II globozoospermia. I revealed that *Pfn3*$^{-/-}$ sperm display abnormal manchette development leading to an amorphous sperm head shape. Additionally, *Pfn3*$^{-/-}$ sperm showed reduced sperm motility resulting from flagellum deformities. I show that acrosome biogenesis is impaired starting from the Golgi phase, and mature sperm seems to suffer from a cytoplasm removal defect. An RNA-seq analysis revealed an upregulation of *Trim27* and downregulation of *Atg2a*. As a consequence, mTOR was activated and AMPK was suppressed, resulting in the inhibition of autophagy. This dysregulation of AMPK/mTOR affected the autophagic flux, which is hallmarked by LC3B accumulation and increased SQSTM1 protein levels. Autophagy is involved in proacrosomal vesicle fusion and transport to form the acrosome. I conclude that this disruption leads to the observed malformation of the acrosome. TRIM27 is associated with PFN3 as determined by co-immunoprecipitation from testis extracts. Further, actin-related protein ARPM1 was absent in the nuclear fraction of *Pfn3*$^{-/-}$ testes and sperm. This suggests that lack of PFN3 leads to destabilization of the PFN3–ARPM1 complex, resulting in the degradation of ARPM1. Interestingly, in the *Pfn3*$^{-/-}$ testes, I detected increased protein levels of essential actin regulatory proteins, cofilin-1 (CFL1), cofilin-2 (CFL2), and actin depolymerizing factor (ADF). Taken together, our results reveal the importance for PFN3 in male fertility and implicate this protein as a candidate for male factor infertility in humans.

SUMMARY II

Profilin4 (*Pfn4*) is a member of profilin gene family and during spermiogenesis localizes to the acrosome-acroplaxome-manchette complex. Yet, the role of PFN4 in male fertility is not fully understood. We generated PFN4-deficient mice and observed structural defects in manchette formation resulting in amorphous heads, and flagellar defects. Further, sperm quantity, and motility were reduced. Interestingly, we observed manchette defects by using HOOK1 and ARL3 antibodies in PFN4-deficient mice. Disrupted *cis*- and *trans*-Golgi networks and aberrant production of proacrosomal vesicles resulting in impaired acrosome biogenesis. Acrosome formation requires the contribution of autophagic machinery during proacrosomal vesicle fusion and transportation. Proteomic analysis showed, that proteins ARF3, SPECC1L and FKBP1, involved in Golgi membrane trafficking and the PI3K/AKT pathway, to be higher abundant in testes of PFN4-deficient mice. In $Pfn4^{-/-}$ mice, protein levels of PI3K, AKT, and mTOR were elevated while, AMPK level was reduced consistent with an inhibition of autophagy. This seems to result in blockage of autophagic flux, by the accumulation of LC3I/II and SQSTM1 in $Pfn4^{-/-}$ mice. In addition, IVF revealed that $Pfn4^{-/-}$ sperms were capable of fertilizing only zona free oocytes. Our results depict for the first time that PFN4 is essential for manchette development, protein transport affecting formation of sperm head, flagella, and acrosome biogenesis.

1. INTRODUCTION

1.1 Male fertility

Male fertility has been declining over the years between 1973 and 2011. There was a significant reduction in both the Total Sperm Count (TSC) and Sperm Concentration (SC) (Levine et al., 2017). Males with below the normal values of sperm parameters according to WHO criteria are thought to display male infertility (Plachot et al., 2002). The most significant of these are Oligospermia (low sperm concentration), Asthenospermia (poor sperm motility) and Teratospermia (abnormal sperm morphology) (Bansal et al., 2015). While some men are infertile, others are sub-fertile. Subfertility usually describes a prolonged period of inability to conceive (Gnoth et al., 2005). Subfertility affects 5% of men (1 in 20) all over the world. The causes of male subfertility are reduced sperm count, reduced fertilization capacity of spermatozoa, STDs, drugs, improper lifestyle and endocrine deficiency (Hirsh, 2003).

Infertility is described as a failure to conceive for a period of two years in a couple trying to reproduce. It is a major clinical problem affecting 13-15% couples globally (Agarwal et al., 2015). Overall males contribute to 50% cases of infertility (Miyamoto et al., 2012). Male infertility is a multifactorial syndrome comprising a wide range of disorders. In male infertility etiology, abnormal production and function of sperm are relating to numerous pre- and pos-testicular or sometimes even directly at testicular level factors. These include- Sexually Transmitted Diseases (STDs), Oxidative Stress, Sexual Dysfunction, Physical Deformities and High BMI (Body-Mass Index) (Bisht et al., 2017) (Tolahunase et al., 2017) (Lotti and Maggi, 2018). Primary testicular abnormality results in about 75% of total male factor infertility (Krausz et al., 2011).

1.2 Spermatogenesis

Spermatogenesis is the process of producing sperm cells from undifferentiated immature germ cells in the seminiferous tubules of testis. Seminiferous tubules are highly organized and complex structures (Figure 1). The process of spermatogenesis involves the conversion of spermatogonial stem cells into the tetraploid primary spermatocytes via mitosis. These tetraploid primary spermatocytes then undergo meiosis to form haploid spermatids (Nishimura and L'Hernault, 2017). Spermatids develop into mature spermatozoa by a process known as

spermiogenesis. During spermiogenesis, round spermatids are transformed into elongated spermatozoa with one-fifth their original sizes (Oakberg, 1956) (Fawcett, 1975) (Figure 1). This is made possible by a series of cellular reconstruction processes such as formation of acrosome and sperm tail, chromatin remodeling, removal of most of cytoplasm and rearrangement of mitochondria along the sperm neck and tail region. Spermiogenesis requires the extensive sperm head reshaping by the interaction of F-actin filaments with actin-interacting proteins such as cofilins and profilins (Rato et al., 2012)(Allais-Bonnet and Pailhoux, 2014).

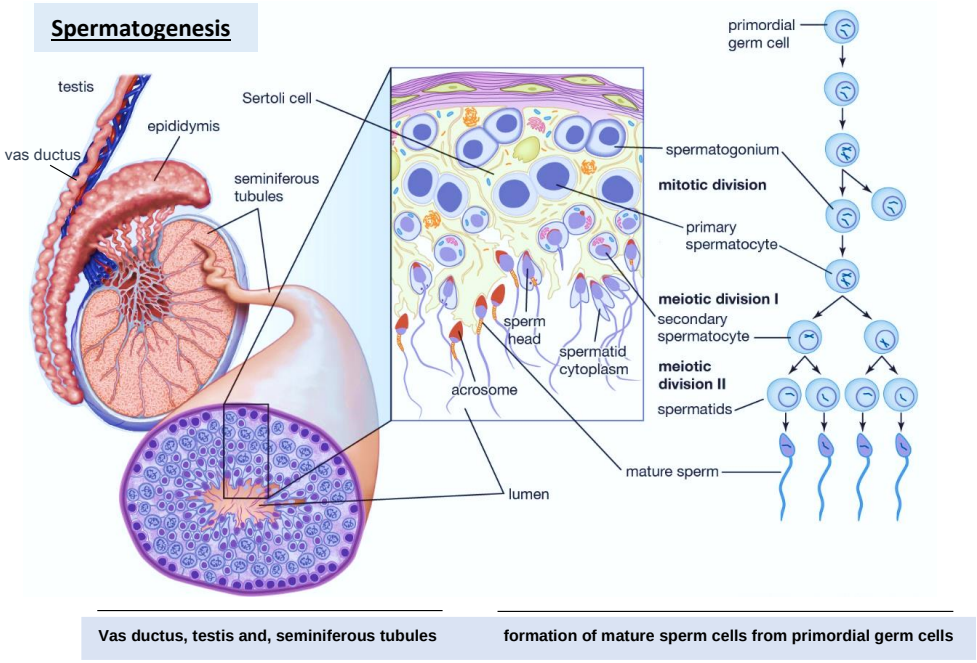

Figure 1: Spermatogenesis in the testes. Process of spermiogenesis in the seminiferous tubules of testes section within the germinal epithelium. Mitosis and meiosis happened on spermatogonia to divide them into primary, secondary spermatocytes and mature spermatozoa. SCs (Sertoli Cells) provide nutritional supplements during this process to the developing germ cells (Adapted from Encyclopedia Britannica., 2013).

1.2.1 Acrosome biogenesis

The acrosome is derived from Golgi and secretory vesicle with an acidic pH, lysosomal hydrolases and proteins such as acrosin and acrosin-binding proteins (Moreno and Schatten, 2000)(Martínez-Menárguez et al., 1996)(Tang et al., 1982). The process of acrosome formation

is formally termed as acrosome biogenesis. Acrosome biogenesis consists of four phases- i) Golgi-, ii) Cap-, iii) Acrosomal- and iv) Maturation phase (Ramalho-Santos et al., 2002). Proacrosomal granules merge to create a single spherical acrosomal vesicle during the Golgi phase (Leblond and Clermont, 1952). The acrosomal granule then forms a head cap like structure during the Cap Phase. Initially, there is vesicle transport from Golgi to the acrosome. However, in the Cap Phase, the Golgi network moves towards the front pole of the cell, and transport of glycoproteins through the Golgi-biosynthetic pathway (Martínez-Menárguez et al., 1996)(Ramalho-Santos et al., 2002). This is followed by the acrosomal phase which involves the apical elongation of the head-cap like structure along the dorsal edge of the cell. The final phase of acrosome biogenesis is the maturation phase which involves the formation of mature acrosome with hydrolytic enzymes (Figure 2).

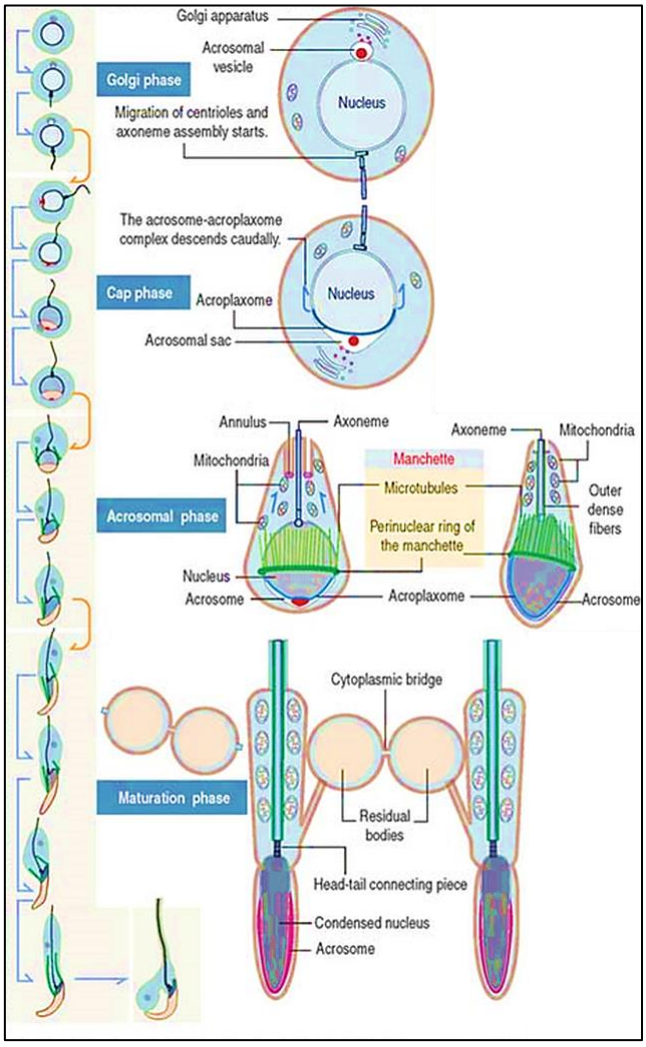

Figure 2: Process of acrosome biogenesis: divided into the Golgi, Cap, acrosomal, and maturation phases. In the Golgi phase, proacrosomal vesicles released from Golgi network and capable of forming single giant acrosomal granule and get attached along the acroplaxome. In

Cap phase, acrosomal granule start to spread over the anterior half of developing spermatid in a cap like structure. This is followed by the acrosomal phase which further requires the formation and apical elongation of cap-like structure on the sperm nucleus. The final phase- the maturation phase entails the formation of a mature acrosomal covering on 2/3rd of the sperm head (Adapted from Basic medical key).

1.2.2 Development of the manchette and nuclear shaping

During the process of sperm nuclear elongation and condensation, the post acrosomal sheath (PAS) of the perinuclear theca (PT) is formed (Figure 3). Formation of the caudal manchette starts during spermiogenesis, and known as temporary microtubular structure present along the base of developing spermatid nucleus (Long and Cook, 1991). Correspondence to the sub acrosomal layer (SAL) formation vital for developing acrosome, removal of manchette after giving the proper shape to sperm nucleus is essential for PAS assembly (Kierszenbaum, Abraham L. and Tres, 2004)(Wu et al., 2007). At the beginning of nuclear elongation, the microtubular manchette posteriorly extends from the nuclear marginal ring to the cytoplasmic lobe at the distal end, creating a ring-like structure that surrounds the spermatid head underneath the acrosome (Figure 3). Protein synthesis and storage occur in the cytoplasmic lobe and the proteins are transported to the manchette microtubule structure in an intra-manchette transport (IMT) process. Proteins such as kinesins and dyneins, known as microtubule motor proteins, are localized in the manchette and play a supportive role in transport of proteins (Moreno and Schatten, 2000; O'Donnell et al., 2012; Russell et al., 1991). In mice, the manchette starts to disappear between steps 13 and 14 of spermiogenesis, after which time the manchette starts to fade in the cytoplasmic lobe.

Abnormalities in the manchette lead to amorphous shape of sperm head and ultimately leads to male sub/infertility. Russell and Calvi reported that manchette is vital for proper shaping to sperm head, and in its absence deformations in sperm head shape ware observed (Russell et al., 1991). This happened because of misplaced manchette on nuclear caudal edge as well as lack of nuclear-manchette connections in mutants (Calvi et al., 2015). For example, HOOK1 deficient mice showed misplaced caudal manchette microtubular structure that led to the crescent or club-shaped sperm head (Mendoza-Lujambio et al., 2002). Similarly, in CLIP-170 deficient mice, abnormal elongation of manchette resulted in amorphous sperm head shape and led to male subfertility (Akhmanova et al., 2005). There are also numerous reports on the loss

of function of KIF3A, IFT88, KATNB1, LRGUK1, CEP131, SPEM1, SPEF2 and PARCG proteins showed abnormally formed manchette leading to the improper shape of sperm head (Mendoza-Lujambio et al., 2002)(Lehti et al., 2013)(O'Donnell et al., 2012)(Gunes et al., 2020). Manchette is connected with sperm nucleus by the fuzzy material/linkers in order to give the proper shape to sperm head. (Figure 3).

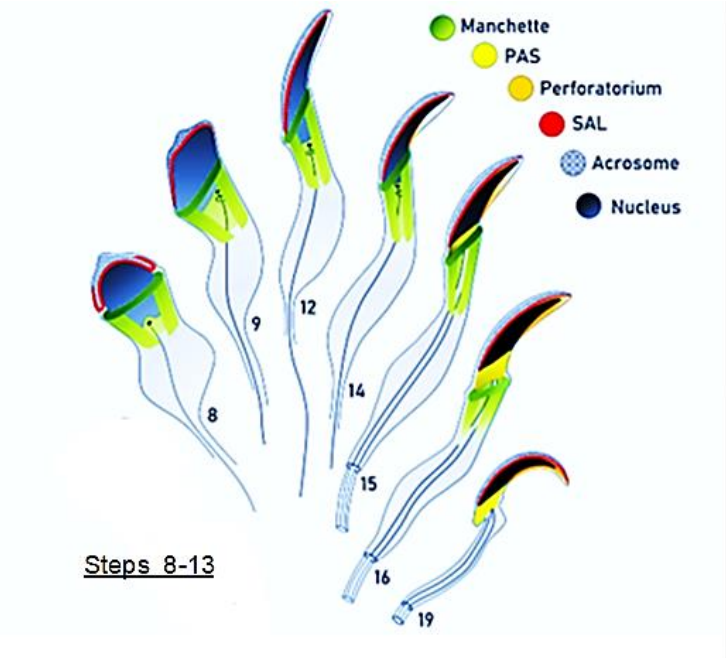

Figure 3: Development of the manchette during spermiogenesis. The manchette (green) starts to develop at the beginning of sperm elongation phase (step 8) and disappears at step 13 after giving the proper shape to sperm head, showed by successive darkening of the nucleus (gray/black). The three regions of the perinuclear theca (PT) in spermatozoa are shown in spatial and temporal order, in the beginning of spermiogenesis the sub-acrosomal layer (SAL, red) is connected to the acrosome (cross-hatched), and the post-acrosomal sheath (PAS, yellow) formed in the later stages of spermiogenesis (Adapted from Wu et al., 2007).

1.2.3 Sperm tail formation

In addition to sperm head, there is another essential structure, a flagellum is present and comprises of about 90% length of the sperm responsible for its propelling and movement in the journey of fertilization. Flagellum plays vital role in male fertility and abnormalities in sperm tail result in impaired motility which ultimately leads to male sub/infertility. Abnormalities in sperm flagella includes, absent, bent, short, coiled, two/multiple tails, thick or irregular mid/principal piece with cytoplasmic droplets. These abnormalities arise because

of defects in any of the internal structures present in sperm tail. Flagellum ultrastructure in the mammals is extremely well conserved and comprised of peri-axonemal and axoneme structures. Peri-axonemal structure further composed of major structural parts outer dense fibers (ODF), fibrous sheath (FS), and the mitochondrial sheath (MS). These parts divided the sperm flagellum into four main sections, the connecting piece, the mid piece, the principal piece, and the end piece (Figure 4) (Lehti and Sironen, 2017).

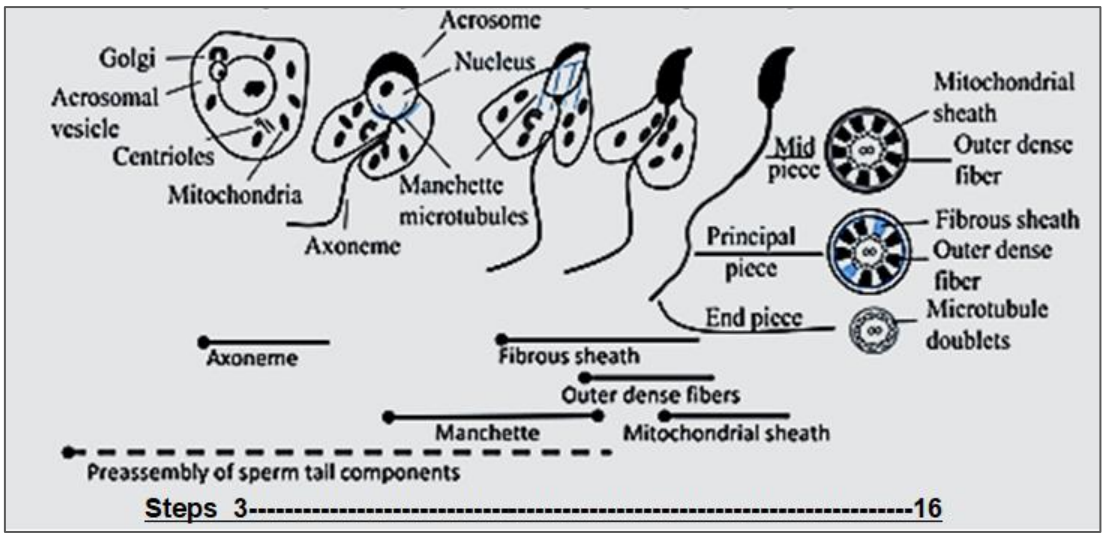

Figure 4: Development of sperm flagellum during mouse spermiogenesis. At step 3 (early stage of spermatogenesis) axonemes developed from the distal centriole. In the mid piece, mitochondrial sheath and ODF are found in, and a fibrous sheath with ODF are located in the principal piece from step 9 to 16. The exact timing for sperm tail formation is indicated with solid line and possible timing of preassembly of sperm tail components with dashed line. (Adapted from Lehti and Seronen).

1.3 The role of sperm in fertilization

A sperm is very specific in its function, in order to fuse and gain entry into an oocyte for delivery of two sub-cellular structures: i) the male pronucleus consist of the genetic material and ii) the centrioles that are structures that help to organize the microtubular cytoskeleton. In order to fertilize an oocyte, spermatozoa must have to undergo the series of steps including capacitation, acrosome reaction (AR) and penetration by breaking the zona pellucida (Sun et al., 2011).

1.3.1 Zona pellucida binding induces the sperm to undergo an Acrosome reaction

Acrosome reaction (AR) is considered as essential step in order to ensure successful entry into an oocyte. Sperm fusion with oocytes is dependent on the interaction of various glycan-binding molecules, carbohydrates in nature and present on sperm's plasma membrane, further enable it to fuse with their respective glycans molecules present on the zona pellucida of an oocyte. Special transduction pathway, known as calcium-mediated signal takes place, which help in the release of many hydrolytic and proteolytic acrosomal contents via exocytosis and AR phenomena happens. (Ikawa et al., 2010). Any structural or functional abnormality in the acrosome could impair sperm fusion, and ultimately result in infertility (Figure 5).

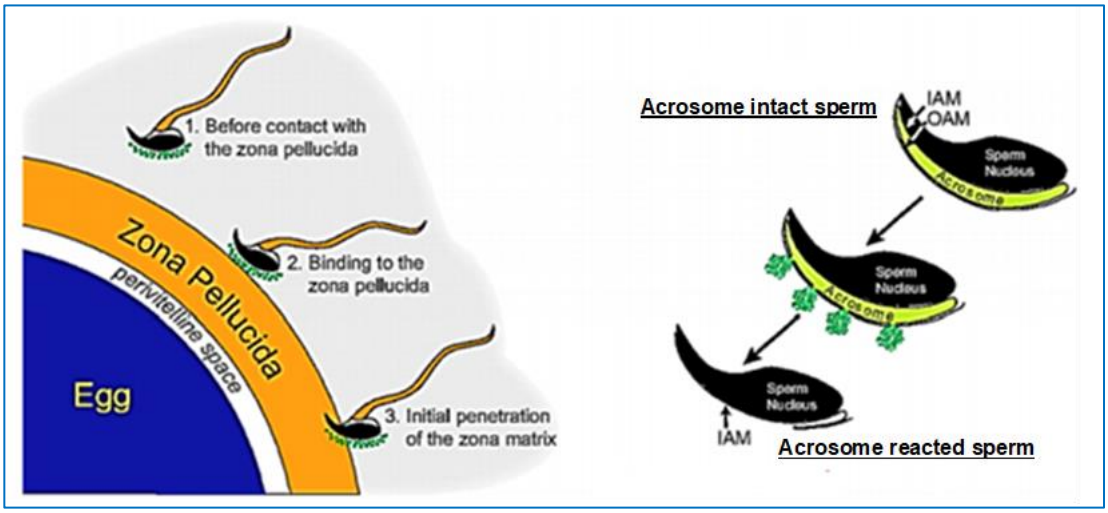

Figure 5: Sperm acrosome reaction. Spermatozoa before undergo fertilization perform the acrosome exocytosis in order to fuse with the oocyte in the perivitelline space. The acrosomal reaction requires the OAM (Outer Acrosomal Membrane) fusion with the oocytes PM (Plasma Membrane), which resulted in the release of acrosomal hydrolytic enzymes. These enzymes help in the degradation of the zona pellucida and assist in oocyte fertilization (Adapted from Avella and Dean, 2011).

1.4 The role of autophagy in acrosome biogenesis

The acrosome is a specialized lysosomal related organelle (LRO) that covers the anterior of the sperm head and is essential for fertilization process. There are only few reports on this lysosome-related organelle (LRO) supporting autolysosome origin of acrosome rather than a mere lysosome. As a result, it was reported that autophagy machinery is involved in the acrosome development. Acrosome biogenesis is propelled by various proteins known to play a

role in autophagy. There, the microtubule associated protein LC3B plays an important role in autophagosome formation and is a widely used biomarker to detect autophaghic flux. Further, autophagy related genes such as *Atg7* (Wang et al., 2014), *Atg9* (Yefimova et al., 2019) and *Atg5* (Huang et al., 2020) are important for the acrosome biogenesis and male fertility. Autophagy itself is regulated, amongst others, by members of the TRIM protein family (Di Rienzo et al., 2020). In colorectal cancer cells, it has been shown, that overexpression of *Trim27* results in activation of AKT signaling (Zhang et al., 2018). AKT is a serine threonine kinase, a downstream class of PI3K and an activator of mTOR (Hahn-Windgassen et al., 2005). In turn, activated mTOR inhibits AMPK signaling, which leads to the suppression of autophagy (Liang et al., 2018).

Autophagy is an intercellular degradation system that transports cytoplasmic components or organelles to lytic organelles for breakdown and recycling, such as lysosomes in humans and vacuoles in yeast (Hamasaki et al., 2013). In the initial, phagophore start to develop as double membrane cup like structure to engulf some cytoplasmic contents and then closes itself into the double membranous vesicle called autophagosome. The process of autophagosome formation is further divided into three main steps: (i) induction of membrane development, (ii) elongation of the isolation membrane, and (iii) closure of the membrane (Abada and Elazar, 2014). Autophagy is generally started to happen in the starvation condition, but now several studies reported its induction in many pathological and physiological conditions including, normal development, placental detachment in mammal's birth, cancer, programmed cell death, diabetes, neurodegenerative disorders and various infections (Hamasaki et al., 2013)(Mizushima et al., 2011; Mizushima and Levine, 2010).

Atg (autophagy related genes) were identified in yeast and are very well conserved in mammals (Mizushima et al., 2011). Of the most important member of ATG protein family is, ATG7, and act as an E1-like activating enzyme, enables the conjugation of LC3B and ATG12. LC3B is known as microtubule-associated light protein chain 3. Upon autophagy induction, LC3B-I is conjugated to phosphatidylethanolamine to generate its second form, LC3B-II, known as the

marker for autophagosome, because of its attachment on autophagosome membrane (Figure 6).

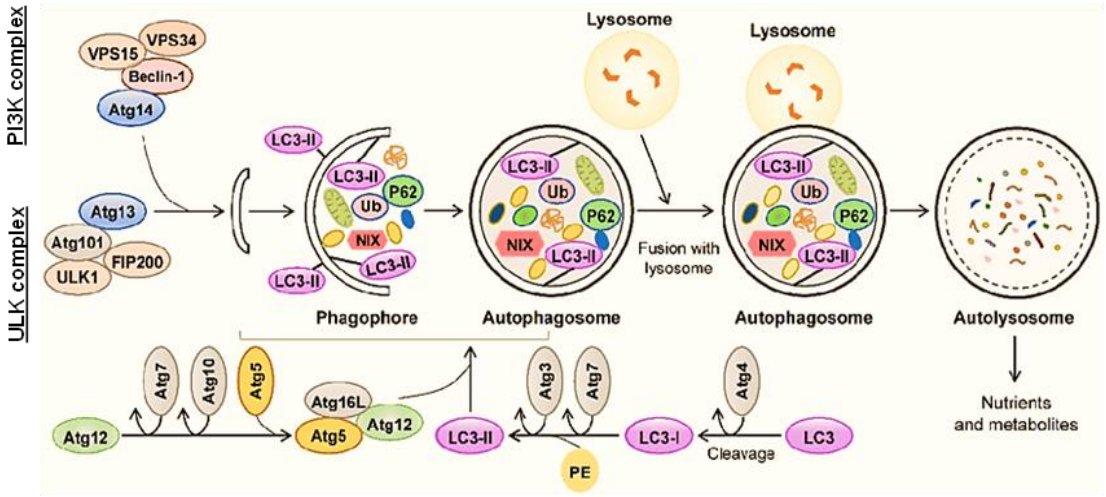

Figure 6: The process of autophagy. Autophagy is the key machinery for the formation of autophagosome, and auto-phago-lysosome formed by its fusion with the lysosome and finally lead to degradation of autophagolysosomal contents. The ULK complex (ULK1, ATG13, ATG 101 and FIP200) and PI3K complex (ATG14, BECLIN-1, VPS15 and VPS34) participates in the formation of phagophore. At once, LC3B as well as ATG12-5-16 conjugated systems play a role in autophagosome formation. Autolysosome formed by the fusion of autophagosome and lysosome, after engulfing the damaged organelles and proteins. In the last step, engulfed contents are degraded by lysosomal hydrolases and released nutrients and metabolites. Atg: autophagy-related gene; LC3: Light chain 3 (Adapted from Li et al., 2020).

1.5 Role of Golgi network in acrosome biogenesis

The Golgi apparatus contains glycosylates and responsible for sorting and export of newly made proteins imported from the endoplasmic reticulum (ER) because it is polar to Golgi's cisternal region. Golgi network possess the tightly stack-like structure made up of numerous flattened cisternae, each cisterna has two faces: (i) *Cis*-Golgi known as entry side and, (ii) *Trans*-Golgi known as exit side of the Golgi apparatus for exporting modified proteins.

Golgi network is the main site for the formation and active trafficking proacrosomal granules in the process of acrosome biogenesis. It helps in controlling, shaping and proper delivery of acrosomal contents to the emerging secretory vesicles. During spermiogeneis, several *cis*-Golgi

proteins such as, Golgin97, Giantin, Beta-COP and MannosidaseII are also found in acrosomal vesicle (Moreno and Schatten, 2000)(Ramalho-Santos et al., 2002). Golgi apparatus is responsible for the synthesize and delivery of acrosomal proteins in membrane bound vesicles for acrosome development. There are various molecular mechanisms involved in the docking and fusion of transporting vesicles in the somatic cells.

Furthermore, Golgi network is also in charge of providing continuous vesicle flow to the developing acrosome as a giant like structure in the later stages Golgi- and Cap-phase of acrosome biogenesis (Ramalho-Santos et al., 2002). In addition to this, it is also reported that numerous Golgi proteins localized in developing acrosome are vital for providing membranous structure to the acrosome during vesicle emerging stage from various Golgi stacks (Figure 7) (Moreno and Schatten, 2000).

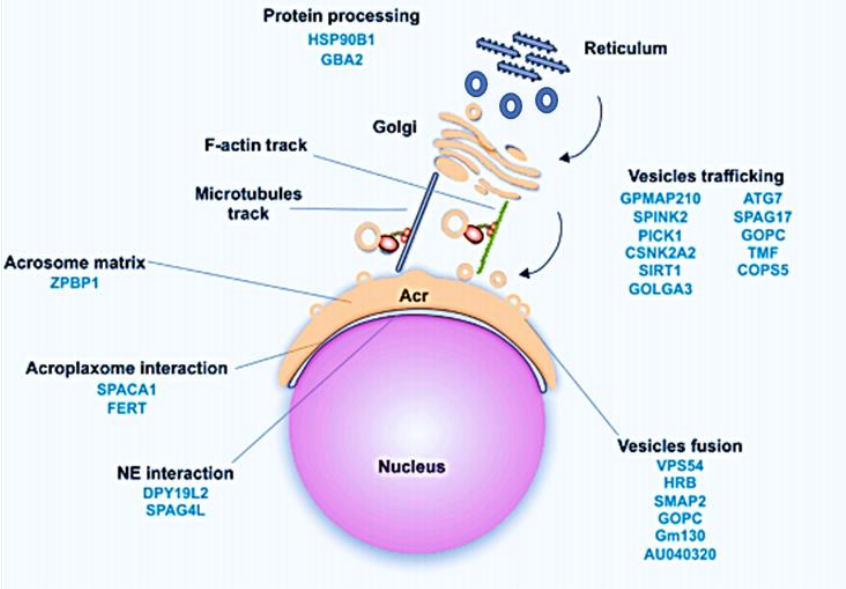

Figure 7: Role of Golgi network in acrosome biogenesis. Many Golgi derived proteins participated in vesicle trafficking and fusion during development of acrosome. As part of the Golgi transport process, proteins are transported from the endoplasmic reticulum (ER) to the Golgi apparatus, vesicles are transported with the use of microtubules and F-actin tracks, vesicles fuse with the acroplaxome, and they are bound to nuclear envelopes (NE) and with the acrosomal matrix (Adapted from Teves et al., 2020).

1.6 Actin cytoskeleton

The cytoskeleton is a system of intracellular filaments critical for cell shaping, cell division and cellular function (Wickstead and Gull, 2011). Among all eukaryotes, actin is the most conserved protein, whereas microtubules and intermediate filaments represent the other two components of the cytoskeleton. It exists in two forms- globular actin (G-actin) and filamentous actin (F-actin) and has been shown to interact with a great multitude of different proteins. It is thought to play a role in cell motility and the maintenance of cell shape and polarity. Actin also plays a role in the growth of the cytoskeleton via extensions formally labeled as the lamellipodia and filopodia (Wioland et al., 2017). During the process of spermatogenesis, spermatogonia undergo extensive alterations to their gross morphology in order to assume the hydrodynamic shape that is characteristic to spermatozoa. This alteration in shape requires the interaction of F-actin filaments with the cytoskeleton and cell membrane (Kierszenbaum, Abraham L. and Tres, 2004).

1.7 Profilins

Profilin was originally identified as a small actin binding protein, ubiquitously expressed and a key player in regulating actin polymerization dynamics (Theriot' and Mitchisont, 1993). Profilin was described to be as a sequestering protein for G-actin. Further reports demonstrate that profilin is now playing a role as a nucleotide exchange factor and help in fasting the rate of 1000 fold for ADP to ATP exchange on G-actin, by this way it replenishes the charging pool of ATP-actin in the cell (Theriot et al., 1994). Newly formed actin filaments consist of ATP–actin and, due to the intrinsic ATP–actin is slowly transformed to ADP–actin in the older part of the filament due to actin ATPase activity (Figure 8). ATP filaments are secured from depolymerizing proteins such as gelsolin and cofilin, whereas ADP filaments are rapidly detached, which provides the cell with an appropriately means to actin-filament turnover. Another mechanism for filament length regulation is the capping and blocking of the growing end (barbed end) by proteins such as the capping proteins capG and capZ. Profilin can speed up the elongation of filament at free ends following the dissociation of capping proteins, in addition to increasing nucleotide exchange on actin monomers.

1.7.1 The Profilin family

PFN3 and PFN4 are mainly expressed in the testes and seem to have roles during spermatogenesis (Behnen et al., 2009). PFN3 protein is detected in the acroplaxome manchette complex of elongating spermatids during the early stages of spermatogenesis (Behnen et al., 2009). However, during the progression through spermiogenesis, PFN3 can be visualized in the developing manchette of spermatids. Similarly, PFN4 is mainly located in the acroplaxome in early S8 spermatids and later in the manchette in S14 spermatids (Behnen et al., 2009). (Figure 8). This indicates that *Pfn4* may play a role in acrosome biogenesis and spermatid nuclear shaping (Obermann et al., 2005). Studies on PFN3 and PFN4 deficient mouse lines have not been published so far.

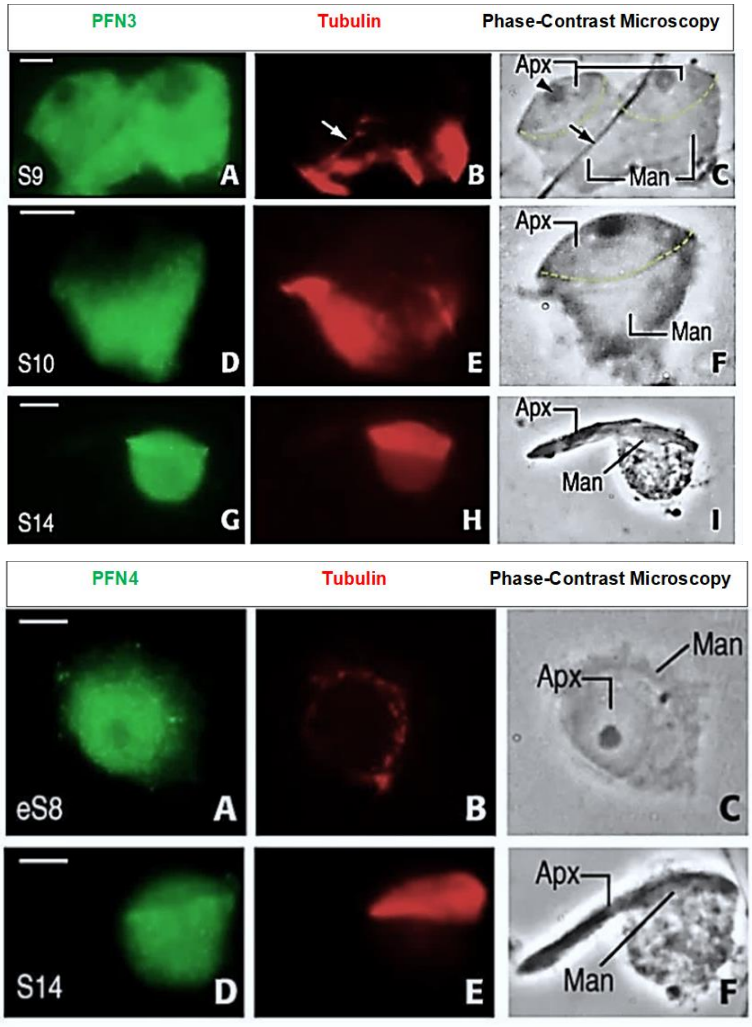

Figure 8: Localization of PFN3 and PFN4 in the acroplaxome-manchette complex in spermatids Panel 1: **(A)** PFN3 is localized in acroplaxome (Apx) and manchette (Man) of S9 spermatids **(B)** Manchette is caudally present to acroplaxome**. (C)** Acrosomal granule is

indicated by arrowhead, howe arrows indicate tubulin reacted sperm tail indicated by arrows. **(D-F)** S10 spermatid. PFN3 is mainly localized in manchette. (G-I) S14 spermatid. PFN3 further localized into cytoplasm of caudally manchette. Panel 2: **(A-C)** Early S8 spermatid (eS8). PFN4 is mainly present in acroplaxome at the beginning of the manchette development **(D-F)** in S14 spermatid, PFN4 is localized only in manchette but not in acroplaxome (Adapted from Behnen et al., 2009).

1.8 Single-cell transcriptome analysis of *Pfn3* and *Pfn4*

Single-cell transcriptome analysis was performed on mouse testis (Ernst et al., 2019). *Pfn3* shows expression in round to elongating spermatocytes and mature spermatozoa. However, *Pfn4* expressed in somatic cells (Sertoli and Leydig cells) at the age of post-natal day 5 (P5), and continue to express till mature spermatozoa formed in adults (Figure 9).

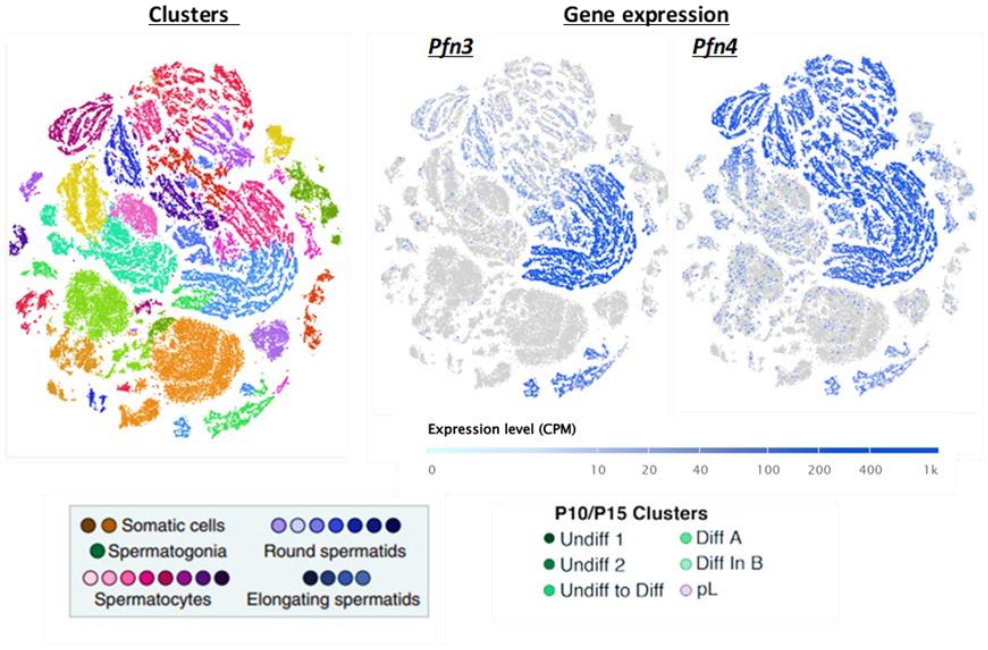

Figure 9: Single-cell RNA-Seq captures a continuum of germ cell-types. Blue indicates high expression whereas grey represents low to no expression. Each cluster is comprised of germ cells in a particular stage of development and is represented by a specific color and cluster. Each dot represents a single cell (Adapted from Ernst et al., 2019).

1.9 Genome editing

1.9.1 Use of guided nuclease to generate genetically modified mice

Yang reported that CRISPR/Cas9 was also useful for genome editing in mice and that co-injection of multiple guide RNAs could induce multiple mutations in mouse genome, simultaneously (Yang et al., 2014).

Rather than requiring complicated constructs or high targeting efficiencies, the CRISPR/Cas9 system and developed methods can produce mice carrying mutations in a single or multiple genes in a single step, as well as mice expressing reporter and conditional alleles (Qin et al., 2015). This method can reduce the time required for the generation of genetically altered mice enormously. Using RNA microinjection into the cytoplasm of the fertilized egg can also be used to make genetically changed mice (Yang et al., 2014), CRISPR compounds were similarly effective when electroporated into oocytes (Qin et al. 2015), as well as when plasmid DNA coding for Cas9 and sgRNA were injected pronuclear (Mashiko et al. 2013).

2. MATERIALS

2.1 Chemicals and Reagents

Table 1 : Chemicals and reagents used in this study

Reagents	Company name	Catalog Number
β-mercaptoethanol	Carl Roth, Karlsruhe, Germany	60-24-2
Ampicillin (Amp)	AppliChem, Darmstadt, Germany	69-52-3
Agar-agar	Carl Roth, Karlsruhe, Germany	9002-18-0
2,4,6-Tris-(dimethylaminomethyl)phenol	Serva, Heidelberg, Germany	90-72-2
Ammonium persulfate (APS)	Carl Roth, Karlsruhe, Germany	7727-54-0
Ammonium sulphate	Carl Roth, Karlsruhe, Germany	7783-20-2
Albumin fraction V (BSA)	AppliChem, Darmstadt, Germany	9048-46-8
Aceton	VWR, Radnor, USA	67-64-1
Calcium chloride	Merck, Darmstadt, Germany	10043-52-4
Chloroform	Sigma-Aldrich, St. Louis, USA	67-66-3
ChemiBLOCKER	Merck Millipore, Darmstadt, Germany	
Collagenase/dispase	Roche, Basel, Switzerland	10269638001
cOmplete™ ULTRA Tablets, Mini Protease Inhibitor Cocktail	Roche, Basel, Suisse	
Coomassie Brillant Blue G250 (CBB)	Biomol, Hamburg, Germany	6104-58-1
CRISPR Cas9 mRNA	Sigma-Aldrich, St. Louis, USA	
6-Diamidino-2-phenylindole dihydrochloride (DAPI)	Thermo Fisher, Waltham, USA	28718-90-3
D-fructose	Merck, Darmstadt, Germany	57-48-7

Diethyl pyrocarbonat (DEPC)	Sigma-Aldrich, St. Louis, USA	1609-47-8
dNTPs	Thermo Fisher Scientific, Waltham, USA	0191
Dulbecco's Modified Eagle Medium (DMEM)	Thermo Fisher Scientific, Waltham, USA	
Ethylenediaminetetraacetic acid (EDTA)	AppliChem, Darmstadt, Germany	60-00-4
Eosin Y solution 0.5 % in H_2O	Carl Roth, Karlsruhe, Germany	17372-87-1
Epon 812	Serva, Heidelberg, Germany	90529-77-4
Formaldehyde (37 %)	AppliChem, Darmstadt, Germany	
Formaldehyde (4%) for immunofluorescence and immunohistochemistry	Merck, Darmstadt, Germany	
Ethanol (EtOH) absolute	VWR, Radnor, USA	64-17-5
Ethidium bromide (Etbr) solution	Carl Roth, Karlsruhe, Germany	1239-45-8
Fluorinert® FC-770	Sigma-Aldrich, St. Louis, USA	86508-42-1
Glacial acetic acid	AppliChem, Darmstadt, Germany	64-19-7
Glucose	AppliChem, Darmstadt, Germany	50-99-7
Glutaraldehyde	Serva, Heidelberg, Germany	111-30-8
Glycine	Carl Roth, Karlsruhe, Germany	56-40-6
HEPES	Sigma-Aldrich, St. Louis, USA	
Hyaluronidase	Sigma, St. Louis, MO, USA	H3506;
Hydrochloric acid	VWR, Radnor, USA	7647-01-0
Ionic Detergent Compatibility Reagent	22663, Thermo Fisher, Waltham, USA	7365-45-9
Methanol (MeOH)	VWR, Radnor, USA	67-56-1
Mineral oil GM-501	GYNEMED, Lensahn, Germany	

MitroTracker Red CMXRos	Thermo Fisher, Waltham, USA	
Nigrosin	Carl Roth, Karlsruhe, Germany	8005-03-6
Nonidet® P40 (substitute)	AppliChem, Darmstadt, Germany	127087-87-0
PageRuler Prestained Protein Ladder	Thermo Fisher Scientific, Waltham, USA	26619
Paraffin Wax Paraplast Plus	McCormick Scientific, St Louis, USA	125387-89-5
Phosphate buffered saline (PBS) tablets	AppliChem, Darmstadt, Germany	524650
Phenol/chlorofom/isoamylalcohol	Carl Roth, Karlsruhe, Germany	
Picric acid	Sigma-Aldrich, St. Louis, USA	88-89-1
Pierce™ 660 nm Protein Assay Reagent	Thermo Fisher, Waltham, USA	1861426
Potassium acetate	AppliChem, Darmstadt, Germany	127-08-2
Potassium chloride (KCl)	Merck, Darmstadt, Germany	7447-40-7
Peanut agglutinin (PNA)-FITC	Thermo Fisher, Waltham, USA	L21409
Ponceau S	Sigma-Aldrich, St. Louis, USA	
Propidium Idodide (PI)	Sigma-Aldrich, St. Louis, USA	
RNAse A	AppliChem, Darmstadt, Germany	
Rotiphorese Gel 30	Carl Roth, Karlsruhe, Germany	
Roti-Load (4× concentrated)	Carl Roth, Karlsruhe, Germany	
Skim milk powder	Merck, Darmstadt, Germany	999999-99-4
Sodium chloride (NaCl)	AppliChem, Darmstadt, Germany	7647-14-5
Sodium dodecyl sulphate (SDS)	VWR, Radnor, USA	151-21-3
Sodium hydrogen carbonate ($NaHCO_3$)	Carl Roth, Karlsruhe, Germany	144-55-8
Sodium hydroxide	VWR, Radnor, USA	1310-73-2
Sodiumacetate (NaAc)	Carl Roth, Karlsruhe, Germany	127-09-3

Sodiumiodoacetat	Acros organics, New Jersey, USA	305-53-3
Tetramethylethylendiamine (TEMED)	Carl Roth, Karlsruhe, Germany	110-18-9
Tris hydrochloride	Carl Roth, Karlsruhe, Germany	1185-53-1
Tris(hydroxymethyl)aminomethane	VWR, Radnor, USA	77-86-1
Triton® X-100	AppliChem, Darmstadt, Germany	9036-19-5
TRIzol™	Invitrogen™, Thermo Fisher Scientific, Waltham, USA	-
Tryptone/peptone	Carl Roth, Karlsruhe, Germany	91079-40-2
Tween® 20	AppliChem, Darmstadt, Germany	9005-64-5
UltraPure™ agarose	Invitrogen™, Thermo Fisher Scientific, Waltham, USA	-
Urea	Merck, Darmstadt, Germany	57-13-6
Xylene	VMP Chemiekontor, Siegburg, Germany	1330-20-7
Yeast extract	Merck, Darmstadt, Germany	8013-01-2

2.2 Buffers and Solutions

Table 2 : Buffers and Solutions used in this study

Buffers	**Recipes**
10% APS	10% (m/v) APS in $_{dd}H_2O$
3 M Sodium acetate	24.61 g sodium acetate, $_{dd}H_2O$ ad 100 ml
575 mM DTT	0.1773 g DTT $_{dd}H_2O$ ad 2 ml
Alkaline lysis buffer (HotShot)	25 mM NaOH, 0.2 mM EDTA
Annealing buffer (x10)	100 mM NaCl, 50 mM HEPES pH7.4
Bouin´s solution	75 ml saturated picric acid, 25 ml formalin (40%), 5 ml glacial acetic acid

CBB destaining solution	450 ml MeOH, 100 ml acetic acid, 450 ml $_{dd}H_2O$
CBB staining solution	1 g CBB, 500 ml MeOH, 100 ml glacial acetic acid, 400 ml $_{dd}H_2O$
Digestion Medium	1 mg/ mL collagenase/dispase, 1 mg/mL hyaluronidase, 1 mg/mL DNAse I, DMEM
DNA lysis buffer	2 ml 5 M NaCl, 1 ml 1 M Tris-HCl, pH 8.0, 5 ml 0.5 M EDTA, pH 8.0, 5 ml 10% (m/v) SDS, ddH_2O ad 100 ml
Eosin-Nigrosin stain	0.67 g eosin Y (color index 45380), 0.9 g sodium chloride, 10 g nigrosin (color index 50420), 100 ml ddH2O
Epon A	62 ml Epon 812, 100 ml 2-Dodecenylsuccinic acid anhydride
Epon B	100ml Epon 812, 89 ml Methylnadicanhydrid
Epon C	20 ml Epon A, 20 ml Epon B, 0.6 ml 2,4,6-Tris (dimethylaminomethyl)phenol
Fixation buffer for TEM	3% (v/v) glutaraldehyde in 0.1 M cacodylate buffer, pH 7.4
HOS solution	1.375 g D-fructose, 0.75 g sodium citrate dihydrate, 100 ml $_{dd}H_2O$
Lab Vision™ PT Module™ Deparaffinization and Heat-Induced Epitope Retrieval Solution (100x) (pH 6.0)	TA-125-PM, Thermo Fisher, Waltham USA
Low pH glycine buffer	100 mM Glycine pH 2.5 (adjusted with HCl)
Lysogeny broth (LB) agar	5 g tryptone/peptone, 2.5 g yeast extract, 2.5 g sodium chloride, 8 g agar, $_{dd}H_2O$ ad 500 ml
LB medium (x5)	25 g tryptone/peptone, 12.5 g yeast extract, 12.5 g NaCl, $_{dd}H_2O$ ad 500 ml
Mouse anesthesia	8.5 ml 0.9% NaCl, 1 ml 10% Ketamine, 0.5 ml 2% Xylazine
Neutralization buffer (HotShot)	40 mM Tris-HCl
PageRuler™ prestained protein Ladder	26616, Thermo Fisher, Waltham, USA
PBST	1 PBS Tablet, 1000 ml H2O, 1 ml Tween 20
Ponceau S staining solution	0.5 g Ponceau S, 5 ml acetic acid, H2O ad 500 ml

Plasmid DNA isolation buffer P1	50 mM glucose, 25 mM Tris-HCl pH 8.0, 10 mM EDTA
Plasmid DNA isolation buffer P2	0.2 M NaOH, 1% (m/v) SDS
Plasmid DNA isolation buffer P3	60 ml 5 M potassium acetate, 11.5 ml acetic acid, 28.5 ml $_{dd}H_2O$
Radioimmunoprecipitation assay (RIPA) buffer (10x)	#9806, Cell signaling Technology, Cambridge, UK
Roti®-Load 1, reducing, 4x conc.	Carl Roth, Karlsruhe, Germany
SDS running buffer x10	VWR, Radnor, USA
Sperm blocking solution	5% (v/v) ChemiBLOCKER, 0.5% (v/v) Triton x-100 in 0.1 M phosphate buffer, pH 7.4
Sperm lysis buffer	1 M Tris-HCl pH 8.0, 3 M NaCl, 0.5 M EDTA, 20 % (m/v) SDS
WB Stripping buffer	5 ml 20% (v/v) SDS, 3.125 ml Tris-HCl pH 8.8, 390 µl β-mercaptoethanol, ddH_2O ad 50 ml
Tris-acetate-EDTA (TAE) buffer (x50)	292 g Tris(hydroxymethyl)aminomethane, 18.6 g EDTA, 57.1 ml glacial acetic acid, $_{dd}H_2O$ ad 1 l
Tris-EDTA (TE) buffer, pH 8.0, low EDTA	AppliChem, Darmstadt, Germany
TNE buffer	0.15 M NaCl, 10 mM Tris-HCl, 1 mM disodium EDTA, pH 7.4
Transfer buffer (x10)	24.2 g Tris(hydroxymethyl)aminomethane, 144.1 g
Transfer buffer (x1)	100 ml Transfer buffer (x10), 200 ml MeOH, 700 ml ddH_2O
Tris^{plus}	0.1241 g Tris-HCl, 1 complete mini tablet, $_{dd}H_2O$ ad 10 ml glycine, 5 ml SDS 20%, $_{dd}H_2O$ ad 1 l
Washing buffer IHC	B1-30A, Medac, Hamburg, Germany

2.3 Kits

Table 3: Kits used in this study

Description	Manufacturer
Dynabeads ™ M-280 Sheep Anti-Rabbit IgG	Thermo Fisher, Waltham, USA
GeneRuler™ 1 kb DNA ladder	Thermo Fisher, Waltham, USA
GeneRuler™ 100 bp plus DNA ladder	Thermo Fisher, Waltham, USA
Maxima SYBR Green Master Mix	Thermo Fisher, Waltham, USA
Maxima First Strand cDNA synthesis Kit	Thermo Fisher, Waltham, USA
MEGAshortscript™ T7 Transcription Kit	Thermo Fisher, Waltham, USA
MEGAclear™ Transcription Clean-up Kit	Thermo Fisher, Waltham, USA
NucleoBond® Xtra Maxi kit	Macherey-Nagel, Düren, Germany
NucleoSpin® Gel and PCR Clean-up	Macherey-Nagel, Düren, Germany
Pierce™ BCA protein assay kit	Thermo Fisher, Waltham, USA
Pierce™ Bovine Serum Albumin Standard	Thermo Fisher, Waltham, USA
SuperSignal West Pico Chemiluminescent Substrate	Thermo Fisher Scientific, Waltham, USA
TOPO™ TA Cloning™ Kit, with pCR™2.1	Thermo Fisher, Waltham, USA

2.4 Equipment

Table 4: Equipment used in this study

Description	Company	Model
Agarose Gel imaging system	Intas Science Imaging Instruments GmbH, Göttingen, Germany	GEL iX20
Antigen retrieval module	Thermo Fisher, Waltham, USA	Lab Vision™ PT module™
Autostainer	Medac, Hamburg, Germany Eppendorf, Hamburg, Germany	480 S
Balance	Sartorius, Göttingen, Germany Sartorius, Göttingen, Germany Ohaus Corporation, USA Sartorius, Göttingen, Germany	BP211S CP3202P JE 120 PT 120
Blot imaging system	Bio-rad, Hercules, USA	ChemiDoc™ MP
Blot transfer system	Bio-rad, Hercules, USA	USA Trans-Blot® Turbo™
Centrifuges	Eppendorf, Hamburg Germany Eppendorf, Hamburg Germany Merck eurolab, Darmstadt, Germany	5415 D 5417 R Galaxy mini
Confocal Microscope	Zeiss, Oberkochen, Germany	LSM170
Confocal super resolution Microscope	Olympus, Tokyo, Japan	Olympus IX73 with UPlanSApo 100x objective
Counting chamber	Marienfeld, Lauda-Königshofen, Germany	Neubauer-improved
DNA SpeedVac	Savant, Farmingdale, USA	DNA110
Electrophoresis power supply	Peqlab, Erlangen, Germany	Consort EV243
Gel electrophoresis chamber	Peqlab, Erlangen, Germany Peqlab, Erlangen, Germany	40-1214 B1
Highspeed camera	Dimax, Kehlheim, Germany	CMOS
Incubator	Selutec, Hechingen, Germany	TECO20
Inverted microscope	Leica, Wetzlar, Germany Olympus, Tokio, Japan	DM IRB IX71
LC pump system	Waters, Milford, USA	nanoAcquity
Magnetic stirrer	Heidolph, Schwabach, Germany	MR3001
Mass spectrometer	Thermo Fisher, Waltham, USA	LTQ Orbitrap Elite
Microplate Absorbance reader	Bio-rad, Hercules, USA	iMark™
Microplate shaker	VWR, Radnor, USA	980121EU

Microscope incubator	Life Imaging Services, Basel, Switzerland	
Microtome Microm	Microm GmbH, Walldorf, Germany	HM 325
Orbital shaker	New Brunswick Scientific, New Jersey, USA	Innova 4000
Polyacrylamide gel electrophoresis (PAGE) chamber	Bio-rad, Hercules, USA	Mini-PROTEAN® Tetra Cell
PAGE Handcast System	Bio-rad, Hercules, USA	Mini-PROTEAN® Tetra Handcast System
PCR thermal cycler	Jena Analytik, Jena, Germany	FlexCycler
pH meter	Schott instruments, Mainz, Germany	
Pipettes (2.5 µl, 10 µl, 20 µl, 100 µl, 200 µl, 1000 µl)	Eppendorf, Hamburg, Germany	research
Pipette controller	BRAND, Wertheim, Germany	Accu-jet® pro
Real-time PCR system	Thermo Fisher, Waltham, USA	ViiA7
Repetitive pipette	BRAND, Wertheim, Germany	HandyStep®
Sample mixer	Thermo Fisher, Waltham, USA	HulaMixer™
Sonicator	Diagenode, Seraing, Belgium	Bioruptor®
Spectrophotometer	Peqlab, Erlangen, Germany	NanoDrop™ 1000
Thermomixer	Eppendorf, Hamburg, Germany	Thermomixer compact
Tissue embedding station	Sakura Finetek, Heppenheim, Germany	Tissue-Tek thermal console Tissue-Tek Dispensing console Tissue-Tek Cryo console
Tissue sample processor	Sakura Finetek, Heppenheim, Germany	Tissue-Tek VIP
Transmission electron microscope	FEI, Eindhoven, Netherland	Verios 460L, with STEM3 detector
Ultramicrotome	Leica, Wetzlar, Germany	Ultracut R
Vortex	Scientific Industries, New York, USA	Vortex-Genie® 2

2.5 Consumables

Table 5: Materials used in this study

Product	Company
1.5 ml / 2 ml reaction tubes	Sarstedt, Nümbrecht, Germany
1.5 ml low binding tubes	Sarstedt, Nümbrecht, Germany
15 ml / 50 ml centrifuge tubes	Greiner Bio-One, Frickenhausen, Germany
5 ml Falcon® Round-bottom FACS Tube	Corning, New York, USA
5 ml Falcon® Round-Bottom FACS Tube with Cell-Strainer Cap	Corning, New York, USA
5 ml reaction tubes	Eppendorf, Hamburg, Germany
Axygen® PCR® strip tubes	Corning Inc., New York, USA
BLAUBRAND®intraMARK micropipettes	Brand, Wertheim, Germany
Costar® Stripettes (5 ml, 10 ml, 25 ml)	Corning Inc., New York, USA
Cover slips 18 x 18 mm	Medite, Burgdorf, Germany
Cover slips 24 x 60 mm	Medite, Burgdorf, Germany
Embedding cassettes for biopsies	Carl Roth, Karlsruhe, Germany
Filtertips (10 µl, 100 µl, 200 µl, 1000 µl)	Nerbe plus, Winsen, Germany
T3 analytical column (1.8 µm particle)	Waters, Milford, USA
HSS Micropipettes PIEZO 8-15-NS	Waters, Milford, USA
Microscope Slides	Marienfeld, Lauda-Königshofen, Germany
Multiply®-µStrip pro 8-strip	Sarstedt, Nümbrecht, Germany
Pipette tips (10 µl, 100 µl, 1000 µl)	Greiner Bio-One, Frickenhausen, Germany
Roti® PVDF 0.45 µm pore size	Carl Roth, Karlsruhe, Germany

Sterican® cannulas	B. Braun, Melsungen, Germany
Whatman paper	Macherey-Nagel, Düren, Germany

2.6 Primers

Oligonucleotides were obtained from Sigma-Aldrich, Traufkirchen, Germany in a dry and desalted format. Primers were dissolved in $_{dd}H_2O$ (10 min, RT) to a concentration of 100 µM and stored at -20°C.

2.6.1 Genotyping Primers

Table 6: Genotyping Primers used in this study

Primer ID	Sequence (5'→3')	Mouse line	Reference
Pfn3-F	ATGAGTGACTGGAAGGGCTACATCAGTGC	B6-Pfn3Δ254 B6-Pfn3Δ41 B6-Pfn3Δ29	This study
Pfn3-R	CTAAGAGCACTGCTCACGCAGCCCACCAA		This study
Pfn4-1G1F	CTTCCCCTCTGAGTACTGGTGAACCCT	B6-Pfn4Δ5417 B6-Pfn4Δ5417	This study
Pfn4-1G1R	GCTTTCACCCTTACACTAAATCCTGGTGA		This study
Pfn4-2G2R	TTTGGATCCCCCAGGAAGTTCTTCCCT		This study

2.6.2 sgRNAs

Table 7: Single guide RNAs used in this study

Primer ID	Sequence top stand (5'→3')	Sequence bottom stand (5'→3')	Reference
Pfn3-sg1	CACCGGTGCAGTGCTGCGGGATCAG	AAACCTGATCCCGCAGCACTGCACC	This study
Pfn3-sg2	CACCGGACGGGCGTGCAATCTGTGT	AAACACACAGATTGCACGCCCGTCC	This study
Pfn4-sg1	CACCGGACACACACTGATAATAAGC	AAACGCTTATTATCAGTGTGTGTCC	This study
Pfn4-sg2	CACCGGTGGTGGCAACTTACACTGC	AAACGCAGTGTAAGTTGCCACCACC	This study

2.6.3 qRT Primers

Table 8: qRT Primers used in this study

Primer ID	Sequence (5'→3')	Reference
qrt-Pfn1-F	CGTAGGCTACAAGGACTCGC	This Study
qrt-Pfn1-R	GGTCTTTGCCTACCAGGACA	This Study
qrt-Pfn2-F	GCTACTGCGACGCCAAATAC	This Study
qrt-Pfn2-R	ACCTTCCCGGTCTTTTCCTA	This Study
qrt-Pfn3-F	TGGAAGGGCTACATCAGTGC	This Study
qrt-Pfn3-R	CTGCCCATGAGCACCAGGAG	This study
qrt-Pfn4-F	AATACAACCCTTCCCTTCGC	Master thesis Sharang Phadke

qrt-Pfn4-R	CTCCAGGAAAAGACCCTGTG	Master thesis Sharang Phadke
Beta-actin-F	TGTTACCAACTGGGACGACA	This study
Beta-actin-R	GGGGTGTTGAAGGTCTCAAA	This study

2.6.4 Sequencing primers

Table 9: Sequencing primers used in this study

Primer ID	Sequence (5'→3')
M13 fwd	TGTAAAACGACGGCCAGT
M13 rev	CAGGAAACAGCTATGACC
px330 seq2	TTGCATATACGATACAAGGCTG

2.7 Medium

Table 10: Medium used in this study

Medium	Recipe/company
TYH Medium	138 mM NaCl, 4.8 mM KCl, 2 mM $CaCl_2$, 1.2 mM KH_2PO_4, 1 Mm $MgSO_4$, 5.6 mM glucose, 10 mM HEPES, 0.5 mM sodium pyruvate, 10 mM L-lactate, pH 7.4, 310-320 mOsm
M2	Sigma-Aldrich, St. Louis, USA
M16	Sigma-Aldrich, St. Louis, USA
KSOM	GYNEMED, Lensahn, Germany

2.8 Enzymes

Table 11: Enzymes used in this study

Enzyme	Company
DNase I from bovine pancreas	Sigma-Aldrich, St. Louis, USA
DNase I, RNase free	Thermo Fisher, Waltham, USA
DreamTaq DNA Polymerase	Thermo Fisher, Waltham, USA
Platinum™ Taq DNA Polymerase	Thermo Fisher, Waltham, USA
Proteinase K	Merck, Darmstadt, Germany
Restriction enzyme BbsI	Thermo Fisher, Waltham, USA
RNase A, DNase free	AppliChem, Darmstadt, Germany
T4 DNA ligase	Thermo Fisher, Waltham, USA
Trypsin 3x cryst	CellSystems, Troisdorf, Germany

2.9 Animals

Table 12: Animals used in this study

Strain	Details	Reference
C57BL/J6	Inbred mouse strain, black coat color	Charles River, Erkrath Germany
B6-Pfn3 254 line 7503	endonuclease-mediated mutation of *Pfn3*	This Study
B6-Pfn3 41 line 7515	endonuclease-mediated mutation of *Pfn3*	This Study

B6-Pfn3 29 line 7511	endonuclease-mediated mutation of Pfn3	This Study
B6-Pfn4 5417 line3	endonuclease-mediated mutation of *Pfn4*	This Study
B6-Pfn4 5417 line6	endonuclease-mediated mutation of *Pfn4*	This Study

2.10 Antibodies

Table 13: Antibodies used in this study

2.10.1 Primary antibodies

Antibodies	Company	Catalog Number	IHC/IF dilution	WB dilution
PFN3	Kind Gift of Prof. Dr. W.Witke		1:200	1:500-1000
CFL1			X	1:1000-2000
CFL2			X	1:1000-2000
ADF			X	1:1000-2000
ARF3	Proteintech	10800-1-AP	1:200	1:1000
ARL3	Proteintech	10961-1-AP	1:200	X
ARPM1	Proteintech	27580-1-AP	1:200	1:500-1000
ATG2A	Thermo Fisher Scientific, Waltham, USA	PA5-77794	X	1:1000-2000
Cleaved Caspase-3	Cell signaling	9664	1:100	X
Cleaved Caspase-9	Cell signaling	9509	1:100	X
Active Caspase-3	R & D systems	AF835	1:100	X
COPA	Thermo Fisher Scientific, Waltham, USA	BS-12464R	1:200	X
FKBP1	Proteintech	10273-1-AP	X	1:1000
GOPC	Proteintech	12163-1-AP	1:200	X

HOOK1	Proteintech	10871-1-AP	1:200	X
LC3B	Abcam	ab58610	1:100	1:500-1000
PICK1	Thermo Fisher Scientific, Waltham, USA	PA5-76084	1:200	X
SPECC1L	Thermo Fisher Scientific, Waltham, USA	PA5-71632	X	1:1000
SQSTM1	Cell signaling	5114	X	1:500-1000
SP56	Molecular Probes, Invitrogen	MA1-10866	1:200	X
ACROSIN	Thermo Fisher Scientific, Waltham, USA	BS-5151R	1:200	X
TRIM27	Proteintech	12205-1-AP	X	1:500-1000
AMPK	Cell signaling	5831	X	1:500-2000
mTOR	Cell signaling	2972	X	1:5000-2000
p-mTOR	Cell signaling	2971	1:50	1:1000-2000
Beta-actin(AC-15)	Santa Cruz	sc-69879	X	1:10000
α-TUBULIN (DM1A)	Cell signaling	3873	1:500	X
GM-130	BD Biosciences, Franklin Lakes, New Jersey, USA	610823	1:250	X
TGN-46(JF1-024)	Thermo Fischer Scientific, Waltham, USA	MA5-32532	1:100	X

2.10.2 Secondary antibodies

Antibodies	**Company**	**Catalog number**	**IHC/IF dilution**	**WB dilution**
goat anti-rabbit HRP	Dako, Agilent Technologies,	P0448		1:2000

	Santa Clara, USA			
rabbit anti-mouse HRP	Dako, Agilent Technologies, Santa Clara, USA	P0260		1:1000
Rabbit IgG(H+L) alexa fluor 488	Thermo Fischer Scientific, Waltham, USA	A-11070	1:200	
Mouse IgG(H+L) alexa fluor 488	Thermo Fischer Scientific, Waltham, USA	A-21202	1:2000	

2.11 Software

Table 14: Software used in this study

Program	Purpose	Source
Adobe illustrator CS4	vector graphics editor	Adobe, San José, USA
CRISPR Design tool	design of sgRNAs	www.crispr.mit.edu
Ensembl	genome database	www.ensembl.org
Gene ontology	enrichment analysis on gene/protein sets	www.geneontology.org
ImageJ	image processing and analysis software	www.imagej.nih.gov/ij

Mendeley reference manager	Tool for arranging references and citations	www.mendeley.com/refernce-management/reference-manager
NCBI PubMed	bibliographic database	www.ncbi.nlm.nih.gov/pubmed/
Nuclear morphology software	Tool for analysis of sperm head shaping	http://bitbucket.org/bmskinner /nuclear_morphology/wiki/Home/
Office for windows	word processing software	Microsoft, Redmond, USA
Proteome discoverer , 2.3.0.523	Identification and quantification of proteins from MS measurements	Thermo Fisher, Waltham, USA
String 11.0	Search tool for retrieval of interacting genes/proteins	www.string-db.org

3. METHODS

3.1 Animal Experiments

3.1.1 Ethics

Mice were housed in aspen-bedded filter-top cages with the 12 hours (h) of light and 12 h of dark cycle in a controlled environment at 21-23°C with 50-70% humidity. Animals were fed ad libitum (AL) with γ-irradiated breeding diet and water. All animal experiments were conducted according to German law of animal protection and in agreement with the approval of the local institutional animal care committees (Landesamt für Natur, Umwelt und Verbraucherschutz, North Rhine-Westphalia, approval ID: AZ84-02.04.2013.A429). For tissue and organ procrurement, mice were anesthesized with isofluran-piramal and sacrificed by cervical dislocation (CD).

3.1.2 Generation of Transgenic Mice

3.1.2.1 CRISPR/Cas9 mediated generation of gene edited mice

Superovulation was done by intraperitoneal injections of PMS (pregnant mare's serum, 5IU) and hCG (human chorionic gonadotropin, 5IU) in C57BL/6J female mice and two females mated with one C57BL/6J male. Zygotes from the oviducts at day 0.5 were harvested and microinjected using an inverted microscope (Leica, Wetzlar, Germany) provided with micromanipulators (Narishige, Japan) and piezo unit (Eppendorf, Hamburg, Germany). Fluorinert (FC-770, Sigma-Aldrich, Taufkirchen, Germany) was filled in injection pipettes (PIEZO 8-15-NS, Origio, Charlottesville, USA) for proper piezo pulse transmission. Co-injection of Cas9 mRNA (100 ng/µl) (Sigma-Aldrich) and in vitro transcribed single-guide RNAs (sgRNA) (50 ng/µl each) were achieved into the cytoplasm of zygotes. The zygotes survived after microinjection were kept for 3 days to KSOM medium 37°C into 5% CO_2 incubator. Resulting blastocysts were transferred into the uteri of pseudo-pregnant foster recipients. The alleles were registered with mouse genome informatics and received the IDs: $Pfn3^{em1Hsc}$ MGI:6384215, $Pfn3^{em2Hsc}$ MGI:6384216, and $Pfn3^{em3Hsc}$ MGI:6384217.

3.1.3 Fertility analysis

For fertility analysis, total 5-7 WT and KO male mice aged 10 to 12-weeks were individually housed with sexually mature WT C57BL/6J females in a controlled breeding experiment. Females were observed for the presence of vaginal plugs and pregnancies. The average litter size from pregnant females were calculated.

3.1.4 Morphological analysis

Pfn3 and *Pfn4* knockouts were used for gross morphological analyses including body weights, testes weight, epididymis weight and appearance of testes as compared to heterozygous and wild type littermates.

3.1.5 In-vitro fertilization (IVF)

B6D2F1 females Oocytes were super-ovulated by Intraperitoneal injection of 5 i.U. Pregnant Mare Serum (PMS) and human Chorionic Gonadotropin (hCG). Oocytes were extracted from the oviducts after 15 hours of the last hormone injection and freed from cumulus cells by treatment with hyaluronidase. Oocytes and sperm were cocultured in M2 medium (Sigma) for 2-4 hours. Oocytes survived after injection were cultivated in KSOM medium as micro-drops (Gynemed, Lensahn, Germany) under the mineral oil (Gynemed) at 37°C and 5% CO_2.

3.1.6 Isolation of Germ cell population from testes

Testes were collected in ice-cold PBS and tunica albuginea was removed carefully. Testicular tissue was minced in 200 µl of digestion medium until all seminiferous tubules seemed to be digested. Then 800 µl of remaining digestive medium was added and incubated for 25 min at 37 °C with slow continuous rotation. Additional mechanical disruption was performed by pipetting the solution for 5 times using recovery tips. Suspension was filtered in 35mm pore size filter to achieve single cell suspension. Cell suspension was pipetted slowly to avoid clogging and cell damage. Cells were collected by centrifuge for 10 min at 37 °C on 400g, supernatant was discarded, and pellet was resuspended in 1 mL of PBS.

3.2 Histochemical Methods

3.2.1 Tissue fixation

Testes and epididymis tissues were fixed in Bouin's solution at 4°C for o/n. Samples were washed with 70% EtOH for 1 h to remove excess picric acid. Organs were processed in paraffin wax. 3-5 µm thick sections were obtained on glass slides and dried at 37°C for o/n.

3.2.2 Hematoxylin and Eosin (H&E) staining

Tissue sections were deparaffinized in xylene for 10 min two times each and hydrated by decreasing the ethanol concentrations in 100% EtOH for 5 min followed by 3 min each in 96% EtOH, 80% EtOH, 70% EtOH. Slides were washed in tap water and basophilic structures were stained with Hemalum solution acid according to Mayer for 3 min. Sections were washed with warm water until cell nuclei showed a blue-violet color on tissues. Acidophilic structures were counterstained in red with Eosin Y for 1 min. Slides were rinsed with tap water and dehydrated by an increasing EtOH gradation 70%, 80%, 96% EtOH, for 3min each, followed by 100% EtOH for 5 min. After incubation in xylene for 10 min, stained tissue sections were mounted with coverslips and Entellan.®

3.3 Biochemical Methods

3.3.1 BCA Assay

Protein lysates obtained from testicular tissues were quantified using the Pierce™ BCA Protein Assay Kit according to the 96-well microplate procedure according to the manufacturer's protocol. Quantification is based on the biuret reaction, the reduction of Cu2+ to Cu+ by proteins in alkaline solution. BCA chelates with generated Cu+ ions, resulting in the formation of a purple reaction product with an absorption maximum at 562 nm. Absorption increases linear with protein concentration and was recorded using iMark™ Microplate Absorbance reader.

3.3.2 Pierce Assay

Sperm protein isolation needs the use of significant amounts of reducing agents, which is not compatible with protein BCA assay. Therefore, sperm protein samples (see 3.4.2) were quantified using Pierce 660 nm Protein Assay Reagent containing Ionic Detergent Compatibility Reagent according to the 96-well microplate procedure of the manufacturer's protocol. Quantification is based on a reaction of a dye-metal complex with basic amino acid residues of proteins under acidic conditions. This results in the deprotonation of the dye and a color change from reddish-brown to green, which was measured using iMark™ Microplate Absorbance reader at 660 nm. Protein concentrations were determined in reference to pre-diluted protein assay standards of BSA (0-2000 µg/ml).

3.3.3 SDS-PAGE

Typically, 20-40 µg of proteins obtained from total cell lysates (diluted in 1 x Roti-load) and boiled at 95°C for 5 min prior to loading (see section 2.1 and 2.2). Next, resolved on 6%, 10% and 15% SDS-PAGE (sodium dodecyl sulfate polyacrylamide gel electrophoresis) gel together with PageRuler Prestained Protein Ladder and separated by electrophoresis. Gels were run in 1x SDS running buffer. Gels were made according to Table 15, using the Mini-PROTEAN® Tetra Handcast System. Proteins were running in the stacking gel at 70 V and separated in the resolving gel at 90-100 V.

Table 15 : Components for a small SDS Polyacrylamide gel

Components	**Resolving gel 6%**	**Resolving gel 10%**	**Resolving gel 15%**	**Stacking gel 5%**
ddH2O	2.6	1.9	1.1	1.4
Rotiphorese30	1.0	1.7	2.5	0.33
1.5 M Tris-HCl, pH 8.8	1.3	1.3	1.3	x
1.0 M Tris-HCl, pH 6.8	x	x	x	0.25

10% SDS	0.05	0.05	0.05	0.02
10% APS	0.05	0.05	0.05	0.02
TEMED	0.004	0.002	0.002	0.002

3.3.4 Western Blot

Following SDS PAGE, using the electro blot transfer system 'Trans-Blot Turbo', the proteins were transferred to a PVDF. Prior to transfer, PVDF membranes were activated with MeOH for 1min at RT and Whatman papers were kept in 1x transfer buffer. Gel and PVDF membrane were placed in a sandwich with 4 Whatman papers each into the transfer cassette. Ponceau S staining was done shortly to test whether the applied amounts of protein were equal, and transfer was successful.

3.3.5 Immunodetection

Prior to incubation with the primary antibody, the membrane was blocked with PBS containing 0,1% v/v Tween and 5% nonfat milk (PBSTM) at 4°C o/n or at room temperature for 1-2 h under constant rotation. Then, the membrane was incubated with the primary antibody in PBSTM at 4°C overnight or at room temperature for 1-3 h under constant rotation. After washing with PBS containing 0,1% v/v Tween (PBS-T) to get rid of excess primary antibodies, the membrane was incubated with the secondary antibody in PBSTM at 4°C overnight or at room temperature for 1h with rotating incubator. Then, the membrane was washed with PBS-T to get rid of the excess secondary antibodies. For protein detection the membrane was incubated with either 'Super Signal West Pico Chemiluminescent' Horseradish peroxidase (HRP)-Substrate for 5min or with 'Westar Supernova' HRP-Substrate for 2 min. Stripping was done on the membrane by keeping in stripping buffer for 20-30min at 65°C in water bath. The resulting signal was detected with the blot imaging system 'ChemiDoc MP'.

3.3.6 Immunolabelling and Microscopy

3.3.6.1 Immunohistochemical staining

Tissue sections on glass slides were pre-treated in the Lab Vision™ PT module™ for both deparaffinization and antigen retrieval. Slides were boiled at 99°C in PT Module™ Buffer (pH 6.0) for 20 min. After cooling down at RT for 20 min, sections were rinsed with ddH2O and incubated with peroxide blocking solution for 10 min at RT to quench endogenous peroxidase activity, which can cause non-specific background staining. Sections were incubated with the primary antibody for 30 min at RT. Used antibodies and dilutions are specified in section 2.10. Signals were detected semi-automatically with Autostainer 480S using the BrightVision+ polymer detection system. Therefore, slides were successively incubated with enhancer solution for 10 min, followed by 20 min incubation in poly-HRP-anti-mouse/rabbit IgG secondary antibody and 8 min incubation in 3, 3' diaminobenzidine tetrahydrochloride (DAB) substrate solution. Sections were washed in washing buffer after every step. Finally, sections were counterstained with Hemalum solution acid according to Mayer for 3 min, dehydrated and then mounted with a coverslip and Pertex®.

3.3.6.2 Immunofluorescence staining

In order to check the acrosome biogenesis at different phases, PNA-FITC Alexa fluor-488 conjugate (Molecular Probes, Invitrogen), anti-mouse GM130 (610823, BD Biosciences, USA) for *cis*-Golgi network and anti-rabbit TGN46 (JF1-024, Thermo Fischer Scientific) for *trans*-Golgi network were used on testes sections according to manufacturer's protocol. 5µm testes tissue sections were taken. Deparaffinization of Bouin's fixed paraffin embedded testes tissue was performed by immersing them in Xylol for 2 times, followed by dehydration steps in 100 %, 95 % and 70 % alcohol. After washing with PBS twice, tissue sample was permeabilized in 0.1 % Triton X-100 for 5 minutes at 37 °C, then blocked in 1 % BSA for 1 hour at room temperature. Tissue sections were incubated with diluted PNA-FITC in PBS at room temperature for 30 minutes, next slides were washed in PBS for 2 times. Tissue sections were incubated with GM130 and TGN46 antibodies diluted at 2 µg/mL in 0.1 % BSA at 4 °C for overnight. Followed by PBS washing and respective secondary antibodies incubation for 1 hour at room temperature. Tissue sections were mounted with ROTI® Mount FluorCare DAPI (Carl Roth, Karlsruhe, Germany). Images were taken within 24 hours using an LSM 710 (Zeiss, Oberkochen, Germany).

3.3.6.3 Periodic Acid Schiff Staining (PAS)

Bouin's fixed 5-µm thick testes sections were deparaffinized and rehydrated followed by incubation for 10min with periodic acid (0.5% in H_2O). Slides were washed with H_2O and incubated for 20min with Schiff reagent. Finally, slides were rinsed for 7min with H_2O, followed by counterstained with hematoxylin, dehydrated and mounted with a coverslip. Images were taken using panoramic 3DHistech™slide scanner.

3.3.6.4 Immunocytochemistry

For sperm Immunofluorescence, after swim out, sperms were washed 2-3 times in PBS followed by fixation in 4 % paraformaldehyde for 20 minutes at room temperature. After washing with PBS, spermatozoa were incubated with PNA-FITC and MitoRed (5nM, 53271; Sigma Aldrich) diluted in PBS at room temperature for 30 minutes. For manchette staining, germ cell population isolated from testes as described in the section 3.1.6 and staining with anti-alpha-tubulin antibody (clone DM1A Alexa flour 488 conjugate; 16-232 Sigma Aldrich) was performed according to Li W et al., (2015). Next, spermatozoa were plated onto Superfrost plus microscope slides (Thermo Fisher Scientific), mounted with ROTI®Mount FluorCare DAPI (Carl Roth, Karlsruhe, Germany). Images were taken within 24 hours using an LSM 710 (Zeiss, Oberkochen, Germany).

3.3.6.5 Immunoprecipitation (IP)

Protein-IP was performed on whole adult testis lysate. Testis tissue was homogenized in RIPA buffer followed by sonication at high speed for five cycles of 30s ON/ 30s OFF with Bioruptor® sonication device and protein extraction was done as described above. Co-IP was performed using Dynabeads® M-280 Sheep anti-Rabbit IgG as described by the manufacturer. The captured and eluted proteins were separated by SDS PAGE and transferred to nitrocellulose membranes in preparation for immunoblot analysis.

3.3.6.6 Transmission electron microscopy

Tissue samples and isolated sperm cells were fixed with 3% (v/v) glutaraldehyde at 4°C for o/n, followed by post-fixation in 2% (m/v) osmium tetroxide at 4°C for 2 h. Fixatives were resolved in 0.1 M Cacodylate buffer and specimen were washed with buffer after each fixation step for 15 min at RT two times each. Next, samples were dehydrated by an increasing EtOH

gradation; 30% for 5 min; 50%, 70%, 90% for 10 min each; two times in 96% for 10 min; 100% for 10 min followed by two times for 15 min. During dehydration, samples were contrasted with 0.5% (m/v) uranyl acetate in 70% (v/v) EtOH for 1-1.5 h at 4°C. Samples were washed with propylenoxide for 10 min at RT (3x) and stored in a mixture of propylenoxide and Epon C (1:1) at 4°C for o/n. Specimen were embedded in Epon C, which was polymerized at 70°C for 24 h. Ultrathin sections were obtained using an Ultramicrotome and picked-up on grids. Following contrasting in 3.5% uranyl acetate for 25 min and lead citrate for 7 min, imaging of ultra-thin sections were taken using the Verios 460L (FEI, Eindhoven, The Netherlands) as the microscope with a STEM III-detector. For Immunogold labelling, prior to fixation in Glutaraldehyde, sections were incubated with PFN3-Antibody (1:50) for 1 hour. Followed by washing, gold conjugated anti-Rabbit IgG 10nm secondary antibody (1:50) incubated for 1 hour. Finally, the sections were post-stained with uranyl acetate and examined with transmission electron microscope CM10 equipped with analysis imaging software.

3.3.6.7 Scanning Electron Microscopy

Sperm cells were fixed in primary fixative: 1 % glutaraldehyde and 0.4 % formaldehyde in 0.1 M sodium cacodylate buffer (pH 7.2) for 30 minutes at 4 °C. After washing the samples 3 times in 0.1 M sodium cacodylate buffer for 5 minutes, post fixed with 1 % OsO_4 in 0.1 M sodium cacodylate buffer for 30 minutes followed by 3 washing steps. Images were taken using a Verios 460L (FEI, Eindhoven, The Netherlands)[61] equipped with a STEM 3 detector.

3.3.6.8 STED imaging

Epididymal sperm after swim out were diluted into PBS (1:10) 400µl of diluted sperm were loaded on Poly-L-Lysine (CAS 25988-63-0, Sigma Aldrich) coated coverslips in a 6-Well-Plate and let sperm attach at 37°C for 30 minutes. After removing the PBS, sperm cells were fixed in 4% PFA followed by quenching with 50mM NH_4Cl for 15 minutes. Sperm cells were permeabilized by 0.02 % Triton-X-100 for 3 minutes followed by washing with PBS. Incubated for 1 hour at RT with Phalloidin-Atto647 (1/1000 in 3% BSA, ab176759, Abcam) and mounted with Prolong Gold Antifade (#P36930, Life Technologies). STED micrographs were acquired using a 4-channel easy3D super-resolution STED optics module (Abberior Instruments, Goettingen, Germany) coupled with an Olympus IX73 confocal microscope (Olympus, Tokyo, Japan) and equipped with an UPlanSApo 100x (1.4 NA) objective (Olympus, Tokyo, Japan), available in the LIMES Imaging Facility.

3.3.7 Mass Spec Analysis

3.3.7.1 Tissue homogenization

20 mg of testes tissue were suspended in 200 µL LYSE buffer of the iST-NHS sample preparation kit (Preomics GmbH, Martinsried, Germany) that was supplemented with 1x HALT1/2 protease inhibitors (ThermoFisher Scientific, Darmstadt, Germany). 50 mg glass beads with 0.5 mm diameter (VWR International GmbH, Darmstadt, Germany) were added to each sample. Tissues were disrupted in a Bioruptor ultrasound device (Diagenode SA, Seraing, Belgium) at 4°C. Samples were reduced incubated at 95°C for 10 min shaking at 1000 rpm. Insoluble matter was separated by centrifugation (10 min, 14,000xg, 10°C). The supernatant was transferred to a new reaction tube. An aliquot was diluted 10-fold in water for measurement of protein content with a BCA assay (Pierce Thermo Scientific) according to manufacturer's instructions.

3.3.7.2 Proteolysis, peptide labeling, and fractionation

Protein solution with 50 µg was added to 50 µL of DIGEST buffer (iST-NHS kit) for digestion of proteins (3h, 37°C). 0.4 mg of TMT10plex isobaric Mass Tag Labeling reagent were added to each sample and incubated at room temperature for 1 h. 10 µL hydroxylamine were used to quench the reaction. The preparation procedure was continued according to the iST-NHS kit instructions. Pooled peptides were dried in a vacuum concentrator, dissolved in IPG buffer pH=3-10 (GE Healthcare, Solingen, Germany) and fractionated with an OffGel device (Agilent GmbH, Waldbronn, Germany) according to manufacturer's instructions. Dried peptide fractions were desalted using ZipTip C18 tips (Sigma-Aldrich Chemie GmbH, Munich, Germany). Eluates were dried and re-dissolved in 10 µL 0.1% formic acid (FA).

3.3.7.3 LC-MS measurements

Peptide separation was performed on a Dionex Ultimate 3000 RSLC nano HPLC system (Dionex GmbH, Idstein, Germany). The autosampler was operated in µL-pickup mode. Peptides were dissolved in 10 µL 0.1% FA (solvent A). 1 µL was injected onto a C18 analytical column (self-packed 300 mm length, 75 µm inner diameter, ReproSil-Pur 120 C18-AQ, 1.9 µm, Dr. Maisch GmbH, Ammerbuch-Entringen, Germany). Peptides were separated during a linear gradient from 5% to 35% solvent B (90% acetonitrile, 0.1% FA) at 300 nL/min. The

nanoHPLC was coupled online to an Orbitrap Fusion Lumos mass spectrometer (ThermoFisher Scientific, Bremen, Germany).

Gradient length was 120 min. Peptide ions between 330 and 1600 m/z were scanned in the Orbitrap detector every 3 s with a resolution of 120,000 (maximum fill time 50 ms, AGC target 100%). Polysiloxane (445.12002 Da) was used for internal calibration (typical mass error ≤1.5 ppm). In a top-speed method peptides were subjected to collision induced dissociation for identification (CID: 0.7 Da isolation, normalized energy 35%) and fragments analyzed in the linear ion trap with target 10,000 and maximum fill time 35 ms, turbo mode. Fragmented peptide ions were excluded from repeat analysis for 25 s. Top 8 fragment ions were chosen for synchronous precursor selection and fragmented with higher energy CID (HCD: 2 Da MS2 isolation, 65% collision energy) for detection of reporter ions in the Orbitrap analyzer (resolution 50,000, maximum fill time 86 ms, target 100,000).

3.3.7.4 Data analysis

Raw data processing and database search were performed with Proteome Discoverer software 2.5.0.400 (Thermo Fisher Scientific). Peptide identification was done with an in-house Mascot server version 2.6.1 (Matrix Science Ltd, London, UK). MS data were searched against *Mus Musculus* sequences from the SwissProt database including isoforms (2019/06, 560459+40403 sequences) and contaminants database (cRAP) (Mellacheruvu et al., 2013). Precursor Ion m/z tolerance was 10 ppm, fragment ion tolerance 0.5 Da (CID). Tryptic peptides with up to two missed cleavages were searched. $C_6H_{11}NO$-modification of cysteines (delta mass of 113.08406) and TMT on N-termini and lysines were set as static modifications. Oxidation was allowed as dynamic modification of methionine. Mascot results were evaluated by the Percolator algorithm version 3.02.1 (The et al., 2016) as implemented in Proteome Discoverer. Spectra with identifications above 1% q-value were sent to a second round of database search with semi tryptic enzyme specificity (one missed cleavage allowed). Protein N-terminal acetylation, methionine oxidation, TMT, and cysteine alkylation were then set as dynamic modifications. Actual FDR values were 0.6% (peptide spectrum matches) and 1.0% (peptides and proteins). Reporter ion intensities (most confident centroid) were extracted from the MS3 level, with co-isolation <90% and SPS mass match >65%.

The mass spectrometry proteomics data have been deposited to the ProteomeXchange Consortium via the PRIDE partner repository with the dataset identifier PXD030394 and 10.6019/PXD030394.

The statistical analysis of the MS data was done using an in-house developed workflow in R environment (R version 3.6) (R Development Core Team, 2018). Prior to the statistical analysis, non-unique peptides and single-shot proteins were removed. From all available fractions, only those with a minimum number of missing values per peptide-spectrum match (PSM) and across all TMT channels were selected. Where this filter returns more than one fraction per PSM, the one with the highest average intensity across all TMT channels was selected. The PSM-level data were then transformed and variance-stabilized using the VSN package (Huber et al., 2002) and then aggregated from PSM-level to protein-level intensities using Tukey's median polish method. The Statistical inference analysis was performed using the R package Limma (Ritchie et al., 2015) in which the peptide pools were modeled as fixed effects. The resulting P-values for each statistical contrast were adjusted for multiple testing by the Benjamini-Hochberg method and the false discovery rates (FDR) were calculated. The volcano plots, heatmaps and PCA plots were generated using ggplot2, Complex Heatmap (Gu et al., 2016) and FactoMineR (Lê et al., 2008) packages, respectively.

3.4 Molecular Biology Methods

3.4.1 Cloning

3.4.1.1 Ligation

For cloning of DNA fragments or polymerase chain reaction (PCR) products (Table 10) T4 DNA ligase was used. The enzyme catalyzes the phosphodiester bonds formation between the 3'hydroxyl group of a DNA fragment with the 5'phosphate group of another fragment. Reactions were carried out according to the manufacturer's protocol. Ligation was performed at 16°C for overnight (o/n).

3.4.1.2 Transformation

Chemically competent Escherichia coli (E. coli) TOP10 and Stabl3 bacteria were thawed on ice for 30min and 5 µl of ligation product was used. Following incubation on ice for another 30 min, bacteria were heat-shocked at 42°C for 45- 60 seconds (sec) and immediately chilled on ice for 1 min. 400 µl LB medium was added into bacteria and incubate at 37°C for 1 h under

shaking at 300 rotations per minute (rpm). Next, 50-100 µl of the bacterial growth was spread on LB-agar plates added with appropriate selection antibiotics and incubated at 37°C for o/n.

3.4.1.3 Plasmid isolation

Isolation of Plasmid DNA was performed by alkaline lysis from bacterial cultures. Bacterial colonies were picked, transferred to LB medium with appropriate antibiotics and incubated at 37°C for o/n under vigorous shaking (250 rpm). Mini Preps were performed using 2ml bacterial suspension for small amounts of DNA. Therefore, bacterial pelleted was formed by centrifugation at 14,000 rpm for 1 min at RT followed by resuspension in 150 µl buffer P1. Next, to induce bacterial lysis 300 µl buffer P2 was added. The reaction was neutralized by adding 150 µl buffer P3 and precipitating cell debris was removed by centrifugation at 14,000 rpm for 5 min at RT. The supernatant containing DNA was transferred to a new reaction tube following by the addition of 1 ml EtOH. Precipitating DNA was pelleted by centrifugation at 13,000 rpm for 10 min at 4°C. Followed by twice washing with 80% EtOH, air-dried and dissolved in low TE low buffer or 5 mM Tris-HCl at 37°C for 1 h. Large amount and high quality of plasmid DNA were isolated from 200 ml bacterial suspension using the NucleoBond® Xtra Maxi kit according to the manufacturer's guide.

3.4.2 Total DNA preparation

3.4.2.1 DNA isolation from tail biopsies and ear punches

For mouse genotyping, HotShot Method was used to isolate genomic DNA from tail tip biopsies or ear punches. Tissue samples were kept in 40-75 µl Alkaline lysis buffer (ALB) and heated at 95°C for 30 min. After cooling down to 4°C on ice, same volume to ALB of neutralization reagent was added and vortexed. 2-5 µl of the lysate were used for PCR reaction.

3.4.2.2 DNA isolation from eukaryotic cells

Cells were pelleted by centrifugation at 10,000 rpm for 3 min and resuspended in 300 µl DNA lysis buffer containing 12.5 µl proteinase K (10 mg/ml). After incubation at 45°C for 1 h, 350 µl phenol-chloroform was added. The suspension was mixed for 10 min at RT and centrifuged at 10,000 rpm for 10 min at 10°C. Supernatant contained DNA was transferred to a new tube and DNA was precipitated by addition of 1/10 volume 3 M NaAc and 3 volumes 100% EtOH. DNA was pelleted by centrifugation at 12,000 rpm for 5 min at RT and washed twice with 70%

EtOH. The DNA pellet was air-dried and dissolved in low TE buffer or 5 mM Tris-HCl at 55°C for 1 h or 37°C for o/n.

3.4.2.3 DNA isolation from sperm

Extraction of sperm genomic DNA was performed as described by Weyrich (2012). Prewashed with PBS sperm samples were lysed in 500 µl sperm lysis buffer containing 2.5 µl Triton-X100, 21 µl 1 M DTT and 40 µl proteinase K (10 mg/ml) at 50°C o/n with moderate shaking. Cell debris was removed by centrifugation at 15,500 g for 10 min at RT. The supernatant was transferred to a new tube and 1 µl glycogen, 1/10 volume 3 M NaAc and 2 volumes ice cold 100% EtOH were added. DNA was precipitated at -20°C o/n and pelleted by centrifugation at 15,500 g for 10 min at RT. The pellet was washed with 75% (v/v) EtOH twice, air-dried and dissolved in ddH2O at 37°C for o/n or 56°C for 1 h.

3.4.2.4 Phenol-Chloroform extraction

Mouse tail were resuspended in 300 µl DNA lysis buffer contained 12.5 µl proteinase K (10 mg/ml) and 40 µl SDS (10% solution in water) followed by incubation at 45°C for 1 h. Afterwards, 350 µl PCI (phenol chloroform) was added and the solution was shaken for 10 min at RT followed by centrifugation for 10 min at 10,000 rpm at 10°C. The DNA containing upper phase was transferred to a new tube containing the three fold volume of 100% EtOH and 1/10 of the volume 3 M sodium acetate (pH 5.2). Precipitated DNA was pelleted by centrifugation at 12,000 rpm for 5 min at RT and washed twice with 70% EtOH. The DNA was air dried for 3-5 min at RT and then dissolved in an adequate amount of TE low buffer (50-500 µl) at 37°C for o/n or 56°C for 1 h.

3.4.3 Agarose gel electrophoresis

Electrophoresis was used to visualize the isolated DNA, PCR product or successful restricted digestions. This technique separates products according to nucleic acid size and migration based of negatively charged DNA molecules within an electric field. Agarose was dissolved and boiled in microwave in 80-100 ml 1x TAE buffer. Following addition of 10 µl 0.07% EtBr, gels were poured and solidified at RT. For the separation of PCR products, 2% (m/v) gels were used, for genomic DNA and bigger fragments <1 kb 0.8-1% (m/v) gels were used. Samples were loaded and electrophoresed at 100-120 V for 40-60 min. GeneRuler™ 100 bp plus or 1

kb DNA ladder (5 µl) was loaded as a size standard. Gels were imaged using Agarose gel imaging system GEL iX20.

3.4.4 RNA extraction

Total RNA was isolated from testis using TRIzol™ according to the manufacturer's protocol. Briefly, tissue was homogeneized in 1 ml TRIzol™ reagent using a glass dounce homogenizer, transferred to a 1.5 ml reaction tube and incubated for 5 min at RT. 200 µl chloroform was added and the suspension mixed vigorously. After incubation at RT for 2-3 mins, samples were centrifuged at 10,000 rpm for 15 min at 4°C. The aqueous phase containing RNA transferred to a new reaction tube by adding 500 µl chilled isopropanol. RNA was precipitated by incubating for 10min at 4°C and then pelleted by centrifugation at 10,000 rpm for 10 min at 4°C. Afterwards washed with 75% (v/v) EtOH twice in DEPC ddH2O or RNase free water. The pellet was air-dried and dissolved in DEPC ddH2O or RNase free water for 10 min at 55°C. Samples were stored at -80°C.

3.4.5 Protein extraction

Tissue samples were homogenized in RIPA buffer supplemented with protease inhibitors (1 ml buffer per 100 mg of tissue) using a glass dounce homogenizer. Lysates were incubated on ice for 15 min followed by sonication for 5 min using the Bioruptor. Cell debris was removed by centrifugation at 13,000 rpm for 15 min at 4°C. Protein lysates were stored at -20°C.

3.4.6 Polymerase chain reaction

For genotyping PCR, DreamTaq Polymerase or Platinum Tag polymerase (Manufacturer's protocol) was used to amplify specific DNA segments. Reaction mixture for DreamTaq was made as given in Table 15. PCR reactions were initiated by denaturation of template DNA at 95°C for 3 min. Cyclic conditions of template DNA consist of three steps: DNA denaturation at 95°C for 30 sec, primer annealing at a temperature 3-5°C below the melting temperature of used primers for 30 sec and extension at 68°C and 72°C (30 sec/500bp) for respective genes. This was followed by final extension at 68°C and 72°C for 5 min. Cycling conditions are listed in Table 16 as they are primer specific and dependent on the probable product size.

Table 16: PCR reaction mixture

Component	Volume
10x DreamTaq buffer	5µl
dNTP Mix, 10 mM	1µl
Forward primer, 10 µM	1µl
Reverse primer, 10 µM	1µl
Template DNA	5µl
DreamTaq DNA polymerase, 5 U/µl	0.5µl
ddH2O	Ad 50 µl

Table 17: Genotyping PCRs

Primers	Cycling Conditions	Product size	Mouse lines
Pfn3-F	95°C 30 sec	414bp WT	
Pfn3-R	95°C 30 sec 67°C 30 sec 68°C 30 sec — 30x	160bp KO 373bp KO 385bp KO	Pfn3Δ7503 Pfn3Δ7515 Pfn3Δ7511
	68°C 5 min		
Pfn4- 1G1F	95°C 3 min	300bp WT	
Pfn4-1G1R	95°C 30 sec 65°C 30 sec 72°C 30 sec — 35x	180bp KO	Pfn4Δline3
Pfn4-2G2R		180bp KO	Pfn4Δline6
	72°C 5 min		

3.4.7 cDNA synthesis

Typically, 500ng RNA samples were digested with DNase I to remove potential DNA contaminations. Reactions were assembled as described in Table 18 and incubated at 37°C for 30 min. Next, 1 µl EDTA (50 mM) was added and DNase I was inactivated at 75°C for 10 min. The whole reaction mixture was used for cDNA synthesis according to the manufacturer's protocol of the Maxima H Minus Reverse Transcriptase Kit. Oligo(dT) primers were used for specific amplification of poly(A)-tailed RNAs.

Table 18: DNase I digest mixture

Components	**Volume**
RNA	1 µg
10x reaction buffer with MgCl2	1 µl
DNase I (1 U/µl)	1 µl
DEPC ddH2O	Ad 10 µl

3.4.8 qRT PCR

Quantitative real time PCR (qRT PCR) was used in order to determine the relative expression of various genes by using the same quantity of cDNA from different samples with Maxima SYBR Green qPCR Master Mix. qRT-PCR was performed using the ViiA7 RealTime PCR System. Reaction mixture was made as described in Table 19, and 384 well titer plate was used to load the reaction in technical replicates (10 µl per well). For qRT-PCR primer sequence, see section 2.6.3. Plates were sealed with an adhesive film and centrifuged at 1000 rpm for 1 min. qRT PCR conditions are specified in Table 20. A CT (cycle threshold) value was calculated for each reaction. The mean CT of each triplicate was normalized to the mean CT of the control gene β-actin (mean CT target gene – mean CT β-actin = ΔΔCT). Relative expression of target genes was determined as $2^{-\Delta\Delta CT}$. A melt curve analysis was performed at the end of each qRT PCR to verify the primer specificity and amplification of a single specific product.

Table 19: qRT PCR reaction mixture

Components	Volume
cDNA	1 µl
Maxima SYBR Green/ROX master mix (x2)	5 µl
Primer forward (10 µM)	0.25 µl
Primer reverse (10 µM)	0.25 µl
DEPC H2O	3.5 µl

Table 20 : qRT PCR program cycling conditions

Stage	Conditions
Hold stage	50°C, 2min; 95°C, 10min
PCR stage	(95°C, 15 sec; 60°C, 1 min) x 40
Melt curve stage	90°C, 15 sec; 60°C, 1min; 95°C, 15 sec

3.5 Semen analysis

3.5.1 Sperm isolation

Sperm were isolated from the cauda epididymis using swim out method. Epididymis was dissected and placed into the 1.0 ml of prewarmed M2 or modified TYH medium. Sperm were released from cauda epididymis by 5-7 incisions, followed by swim out for 15-20 min at 37°C. Sperm were counted using a Neubauer improved counting chamber. Therefore, sperm were immobilized by 1:50 – 1:100 dilutions in ddH2O.

3.5.2 Hypoosmotic swelling test

In order to evaluate the sperm membrane integrity, 100 µl of isolated sperm were added to 1 ml of prewarmed HOS solution. After incubating for 30 min at 37°C, the suspension was mixed carefully with the Pasteur pipette. One drop was placed on a microscope slide and covered with a 24 x 60 mm cover slip. At least 200 spermatozoa images were taken at 30-fold magnification using phase-contrast within 1 h after preparation of the slides.

3.5.3 Eosin-Nigrosin staining

Typically, equal volume of isolated sperm was mixed with equal volume of Eosin-Nigrosin solution (50 µl sperm+ 50 µl E& N solution). After incubation for 30 sec at RT, sperm smears were placed on glass slides and air-dried. Slides were mounted with a 24 x 60 mm coverslip and Entellan®. Heads of at least 200 sperm were evaluated at 40- fold magnification under phase-contrast microscope.

3.5.4 Sperm motility analysis

Epididymal sperm were incubated in TYH medium at 37 °C for 20 minutes, after swim out sperm cells were diluted into the TYH medium supplemented with BSA. The diluted cell suspension was placed onto the pre-warmed (37°C) slide and video was recorded using the Basler Microscopy ace camera (acA 1920-155uc) at 300 frames, streaming video using Pylon viewer (v.5.0.11.10913, Basler AG, Ahrensburg, Germany). Sperm motility was evaluated by using the OpenCASA program as described by Alquézar-Baeta., et al (2019).

3.5.5 Nuclear Morphology analysis

For nuclear morphology analysis, after swim out sperm cells were fixed and washed 3 times in 2% paraformaldehyde (PFA). After fixation, sample was diluted in fixative and spread evenly on glass slide and allowed air dried. Slides were counterstained with DAPI (Carl Roth, Karlsruhe, Germany) as described by Skinner et al., (2019). Images were taken on the Leica DM5500 B / JVC KY-F75U digital camera. Images were analyzed using the ImageJ plugin “Nuclear morphology analysis v1.15.3” according to the developer’s instructions.

3.6 Sequencing

3.6.1 Sanger sequencing

Plasmid DNA was diluted to a concentration of 80-100 ng/µl with 5 mM Tris-HCl. 5 µl of DNA was mixed with 5 µl of sequencing primer (5 µM). Samples were sequenced by GATC, Cologne, Germany.

3.6.2 RNA seq analysis

RNA integrity (RIN) was determined by the sequencing facility (UKB sequencing core facility) using the RNA Nano 6000 Assay Kit with the Agilent Bioanalyzer 2100 system (Agilent Technologies, Santa Clara, CA, USA). RIN values ranged from 8.2-10 for all samples. RNA sample quality control and library preparation were performed by the sequencing facility (UKB sequencing core facility), using the QuantSeq 3´-mRNA Library Prep (Lexogen). RNAseq was performed on the Illumina HiSeq 2500 V4 platform, producing >10 million, 50bp 3'-end reads per sample.

All samples were mapped to the mouse genome (GRCm38.89). Mapping was done using HISAT2 2.1 (Kim et al., 2015). Transcript quantification and annotation was done using StringTie 1.3.3 (Pertea et al., 2015). Gene annotation information for the mouse genome was retrieved from the Ensembl FTP server (ftp://ftp.ensembl.org) (GRCm38.89). We used the python script (preDE.py) included in the StringTie package to prepare gene-level count matrices for analysis of differential gene expression.

Differential expression was tested with DESeq2 1.16.1 (Love et al., 2014). Pseudogenes were removed from the count matrices based on "biotype" annotation information extracted from Biomart (R-package biomaRt) (Durinck et al., 2005) Low counts were removed by the independent filtering process implemented in DESeq2 (Bourgon et al., 2010). The adjusted p-value (Benjamini-Hochberg method) cutoff for DE was set at < 0.05, log2 fold change of expression (LFC) cutoff was set at > 1.5.

The datasets presented in this study can be found in online repositories. The names of the repository/repositories and accession number(s) can be found at: https://www.ncbi.nlm.nih.gov/geo/, GSE171068.

3.7 Statistics

If not stated otherwise, the mean of all values ± standard deviation for a particular data set has been represented in graphical form. Error bars have been used to denote standard deviation. Two-tailed unpaired Student's T-Test was performed to ascertain the significance of the variability in data. For pairwise comparison of more than two dataset, one way ANOVA using Tukey HSD post-hoc (*$p < 0.05$, **$p<0.005$, ***$p<0.001$) was considered as statistically significant.

4. RESULT I

Two of the four known profilin gene family members *Pfn3* and *Pfn4* are expressed in the testes. Contrary to PFN1 and PFN2, PFN3 affected the kinetics of actin polymerization to a lesser extent, suggesting alternative and additional roles of PFN3. During the early steps of spermiogenesis, PFN3 is mainly observed in the acroplaxome of round spermatids and later detected in elongating spermatids at the acroplaxome–manchette complex (Behnen et al., 2009).

4.1 Ultrastructural analysis of PFN3 localization in mouse testes

We examined the distribution of PFN3 at ultrastructural level during spermiogenesis with a PFN3 polyclonal antibody and a gold-conjugated secondary antibody using Immunoelectron microscopy. In the Golgi phase, the electron dense giant acrosomal granule forms from the numerous Golgi-derived proacrosomal vesicles (Figure 10 A). Gold particles were detected representing PFN3 in the *cis*- and *trans*- part of Golgi network adjacent to the nuclear pole of the round spermatid (Figure 10 B-C, E-F arrows). The *cis*- part is responsible for organizing and sorting of proteins imported from the Endoplasmic Reticulum (ER) and transported to the *trans*- part of the Golgi network where they are modified and exported as proacrosomal vesicles (Figure 10 E). Immunogold labelling was detected in the acrosomal granule (Figure 10 C, circle) a giant structure attached to the middle of the acroplaxome (Figure 10 E, H, white stars) of developing spermatozoa. We detected gold traces in the mitochondria, which are responsible for providing energy for flagellum propelling and germ cell differentiation (Figure 10 D-E, white arrows). Some of the gold particles were detected in the inner membrane of acrosome-acroplaxome interface suggesting that PFN3 contributes to the attachment of acrosomal granule (Figure 10 E, white stars). In the Cap phase (Figure 10 G), we detected PFN3 in the acrosomal vesicles (Figure 10 H, I, asterisk), which are responsible for the formation of acrosome. In addition, we detected few gold traces in the nucleus (Figure 10 H-M), suggesting that PFN3 might play a role in sperm nuclear shaping. Immunogold labelling also showed PFN3 localization in inner and outer membrane at the leading edge of the acrosome (Figures 10 H-I, K elbow). Gold traces were also detected in highly specialized structures of elongating spermatozoa such as the manchette (Figure 10 J, M, while arrow heads), the acroplaxome marginal ring (Figure 10 O, double arrows), as well as flagellum formation (Figure 10 N, Q,

T). Cross sections of the flagellum showed gold traces in mitochondria which are gathered around the axoneme (Figure 10 U-W) to form the mitochondrial sheath in the sperm mid-piece (Figure 10 W). So, PFN3 is detected in the Golgi sub-domains, the acroplaxome-manchette complex and mitochondria suggesting a role for PFN3 in acrosome biogenesis, sperm head shaping and tail formation. The negative control is given in the supplementary data (Figure 10 Y-Z).

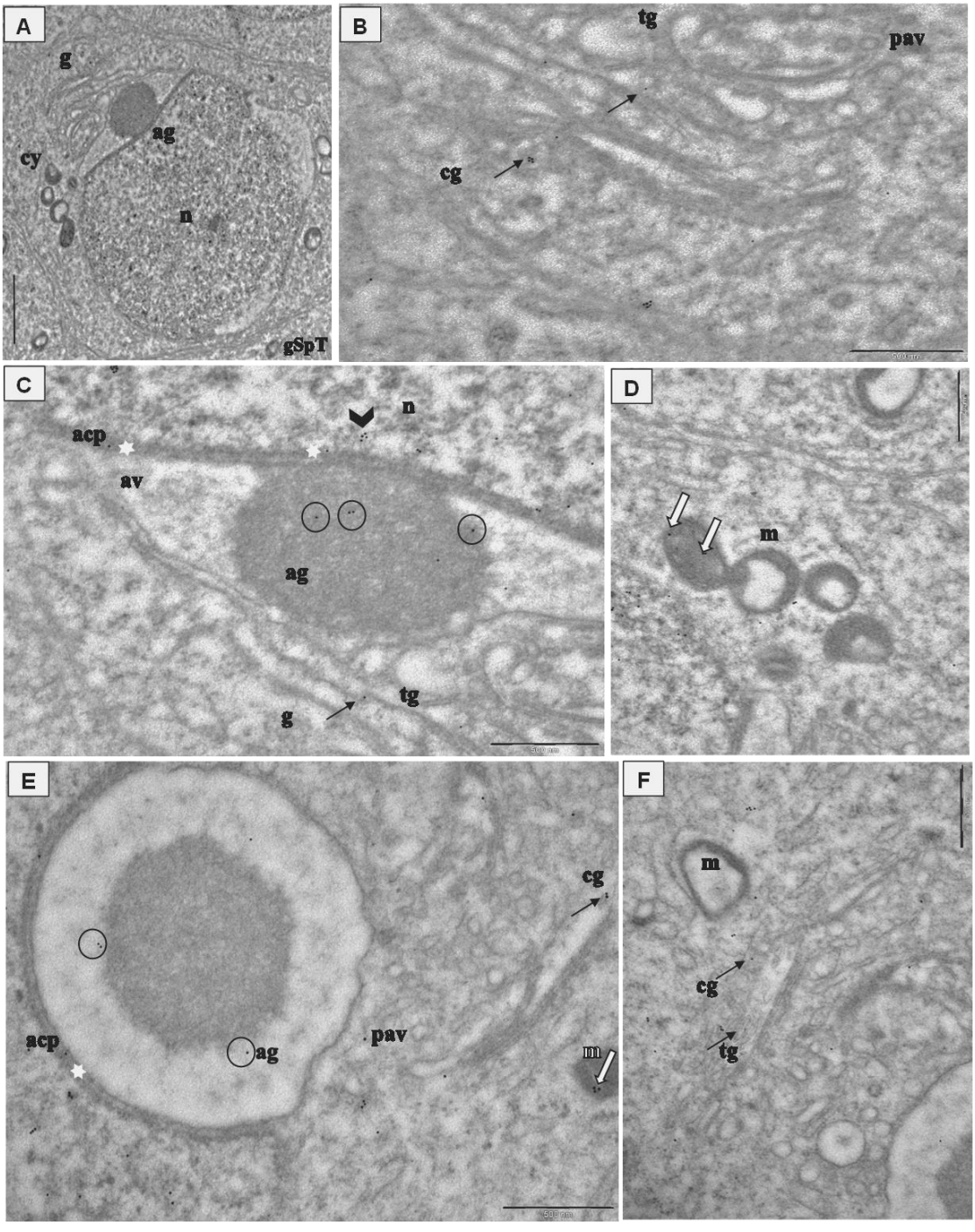

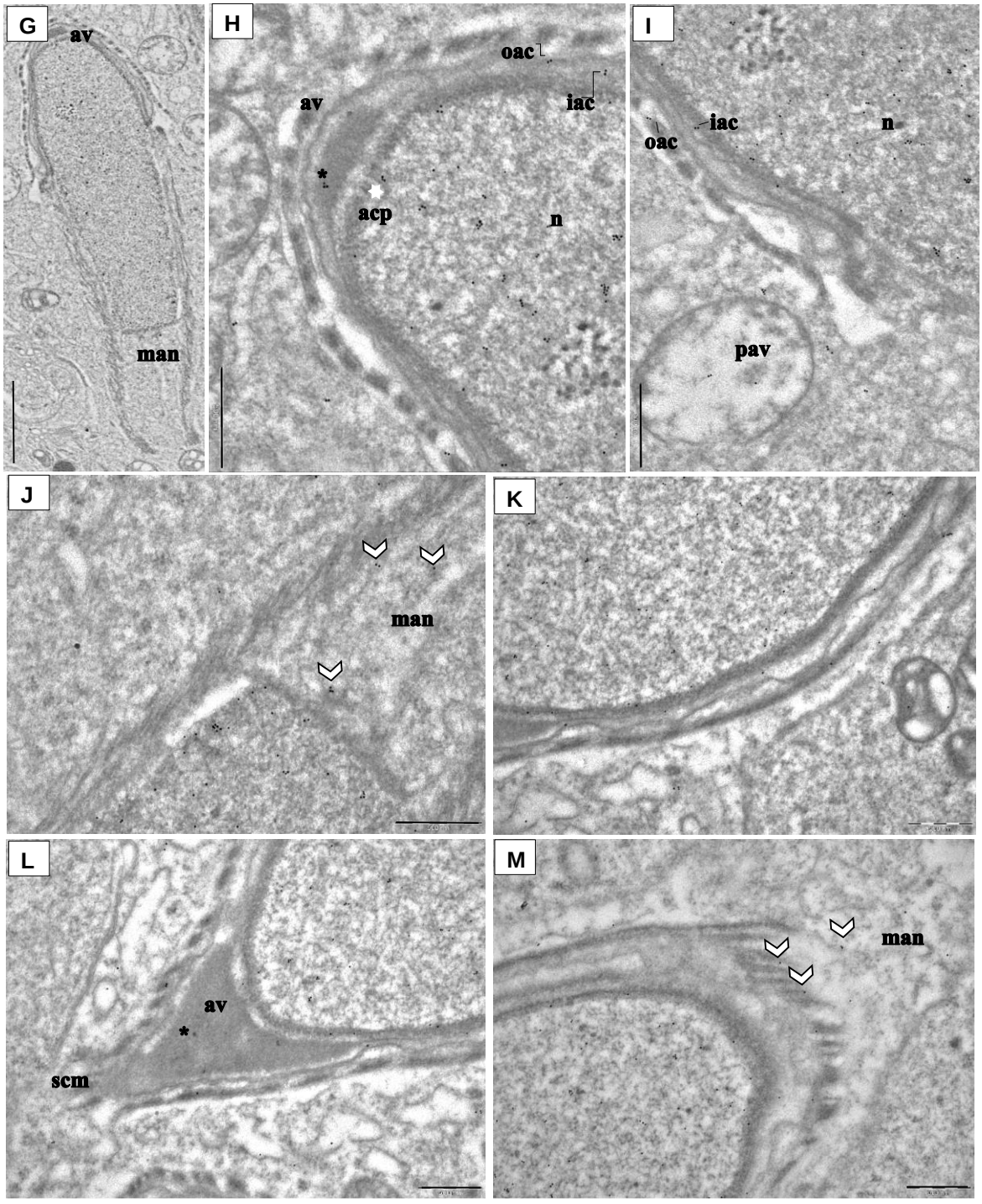
G
av
man
H
oac
iac
av
*
acp
n
I
iac
n
oac
pav
J
man
K
L
av
*
scm
M
man

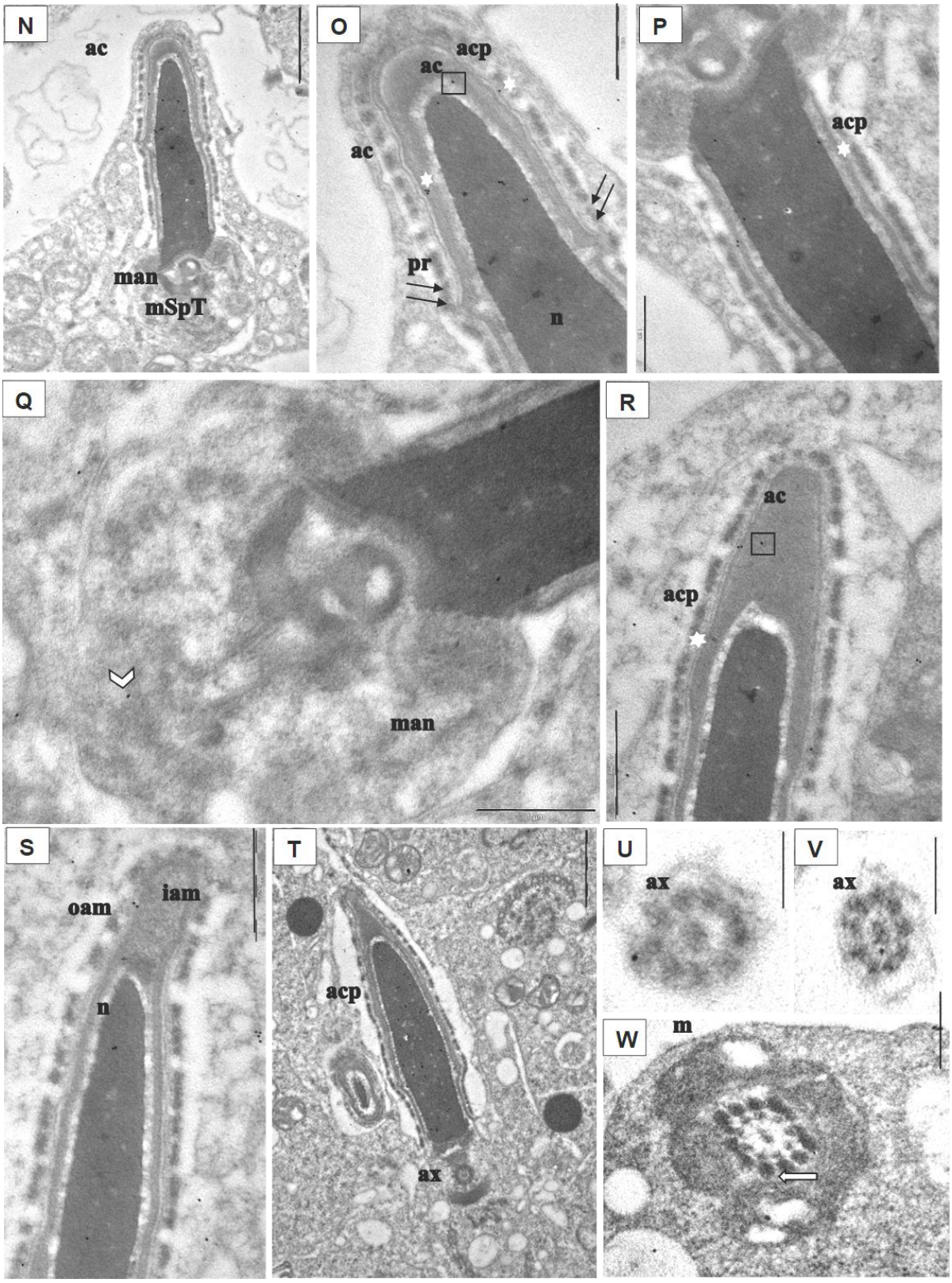
N
ac
man
mSpT
O
acp
ac
ac
pr
n
P
acp
Q
man
R
ac
acp
S
oam
iam
n
T
acp
ax
U
ax
V
ax
W
m

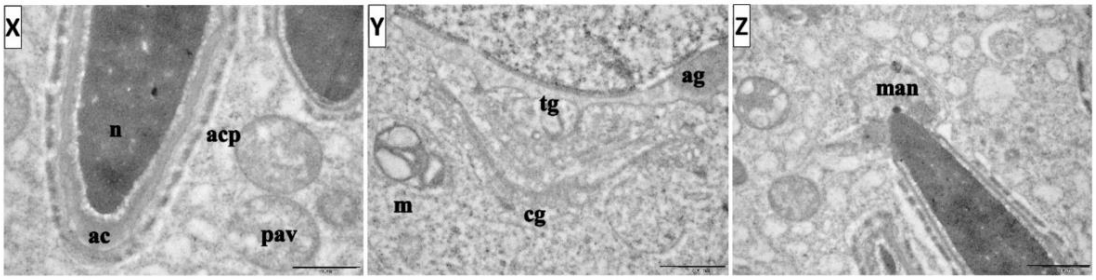

Figure 10: Immunogold labelling using PFN3 antibody on testes sections. **(A-F)** In Golgi phase, **(G-M)** In Cap phase, (**N-W)** In Maturation phase, PFN3 is localized in various cellular compartments. (**X-Z)** Negative control. **g**=Golgi, **cy**=cytoplasm, **ag**=acrosomal granule, **n**=nucleus, **gSpT**=spermatid in Golgi phase, **cg**=cis-Golgi, **tg**=trans-Golgi, **pav**=proacrosomal vesicle, **acp**=acroplaxome, **m**=mitochondria, **av**=acrosomal vesicle, **man**=manchette, **oac**=outer acrosomal membrane, **iac**=inner acrosomal membrane, **scm**=sertoli cell membrane, **ac**=acrosome, **pr**=perinuclear ring, **mSpT**=spermatid mid piece, **ax**= axoneme. Details of indications described in the result part. Scale bar = 1 μm & 500 nm.

4.2 *Pfn3* deficient male mice display sub-fertility and low sperm quantity and quality

Pfn3 is located on chromosome 13, and has one exon. We generated *Pfn3* deficient mice by injecting Cas9 mRNA and two sgRNAs into the cytoplasm of fertilized eggs targeting the exon of the gene. Six pups carrying CRISPR/Cas9-induced mutations were identified (Figure 11 A) and 3 mouse lines, *Pfn3*Δ254, *Pfn3*Δ41 and *Pfn3*Δ29 harboring deletions of 254 bp, 41 bp and 29 bp respectively, were established after sequencing by backcrossing with C57BL/6 mice. All deletions result in null alleles since they encode for frame shifts in the PFN3 reading frame leading to premature translational termination (Figure 11 B). Real time quantitative PCR (qRT-PCR), western blotting and Immunohistochemical staining (IHC) confirmed the deletion of *Pfn3* in the *Pfn3* deficient mice (Figure 11 C). Western blotting displayed a signal in testis/post-natal testis (day 28). All other tissues tested were negative for PFN3. Similarly, IHC produced a signal for PFN3 in testis but not in brain and kidney sections. These results indicate the specificity of the PFN3 antibody (Figure 11 D). IHC of WT testis section using anti-PFN3 antibody showed strong expression of PFN3 in the nuclear region of elongated spermatids (Figure 11 C). Males heterozygous for either *Pfn3*Δ254, *Pfn3*Δ41 and *Pfn3*Δ29 produced an average litter size of 7.6, 7.9 and 7.3 respectively (Figure 11 E), which is comparable to wildtype mice with a mean litter size of 8.2 (Biggers et al., 1962). Homozygous *Pfn3* male mice are sub-fertile since they produced an average litter size of 1.5, 2 and 4 for *Pfn3*Δ254,

*Pfn3*Δ41 and *Pfn3*Δ29 respectively (Figure 11 E).

Adult *Pfn3* deficient males for either *Pfn3*Δ254, *Pfn3*Δ41 and *Pfn3*Δ29 mated with females normally as vaginal plugs were clearly detectable. Relative weights of testes and epididymis of *Pfn3* deficient mice (*Pfn3*Δ254) were slightly reduced, however that reduction was not significant (Figure 11 F, G). Histological analysis using H & E (hematoxylin and eosin) staining on $Pfn3^{+/+}$, $Pfn3^{+/-}$ and $Pfn3^{-/-}$ testes sections showed normal morphology of seminiferous tubules (Figure 11 H). This suggests that deletion of *Pfn3* left the gross morphology of testes and epididymis unaffected.

However, $Pfn3^{+/-}$ and $Pfn3^{-/-}$ males showed a significant reduction in sperm count (Figure 11 I). Next, eosin and nigrosine (E&N) staining was performed to assess the vitality of spermatozoa. E&N distinguish live (whitish in color, arrowhead) from dead sperm (pink in color, arrow, Figure 11 J). A percentage of live sperm in the range of 60-80% is considered normal, borderline 40-60% and below 40% is considered abnormal. E&N staining showed that in heterozygous males the percentage of viable sperm are in the normal range, while in case of *Pfn3* deficient mice the percentage of viable sperm was at borderline (~40%) (Figure 11 K). Further, the Hypo-osmotic swelling test (HOS) was performed to check the integrity of sperm membrane, where intact (live) sperm displays a swelling of the tail (Figure 11 L). The percentage of Hypo-osmotic reactive sperm for $Pfn3^{-/-}$ mice was again at borderline (Figure 11 M). Male mice for *Pfn3*Δ41 and *Pfn3*Δ29 have the same phenotype as *Pfn3*Δ254 mice (Umer et al., 2021). In conclusion, loss of *Pfn3* impinges not only on sperm quantity but sperm quality.

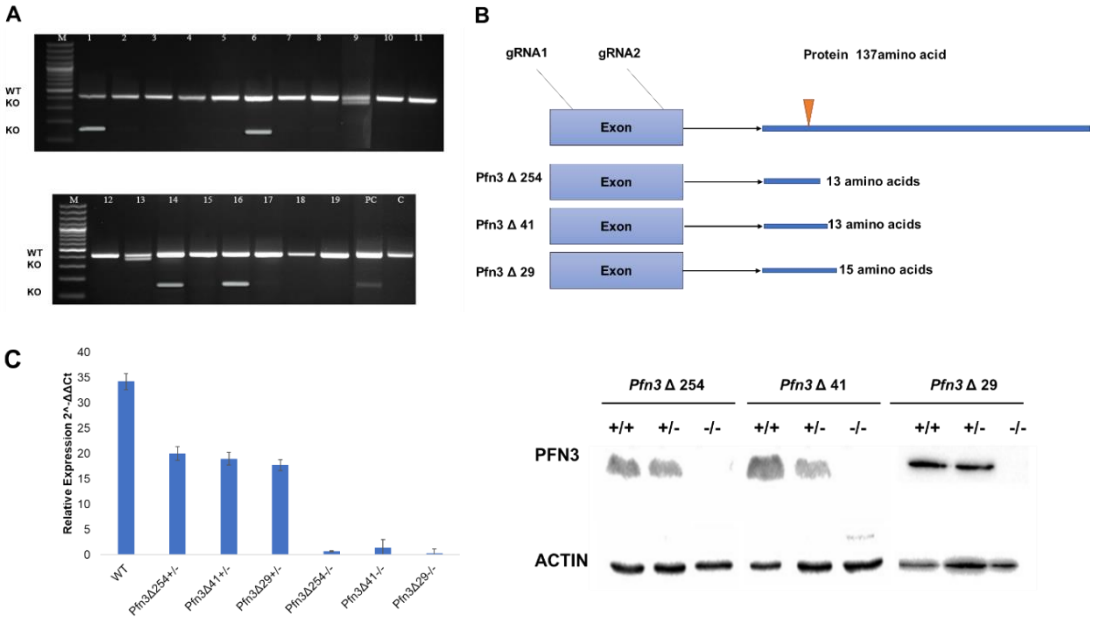

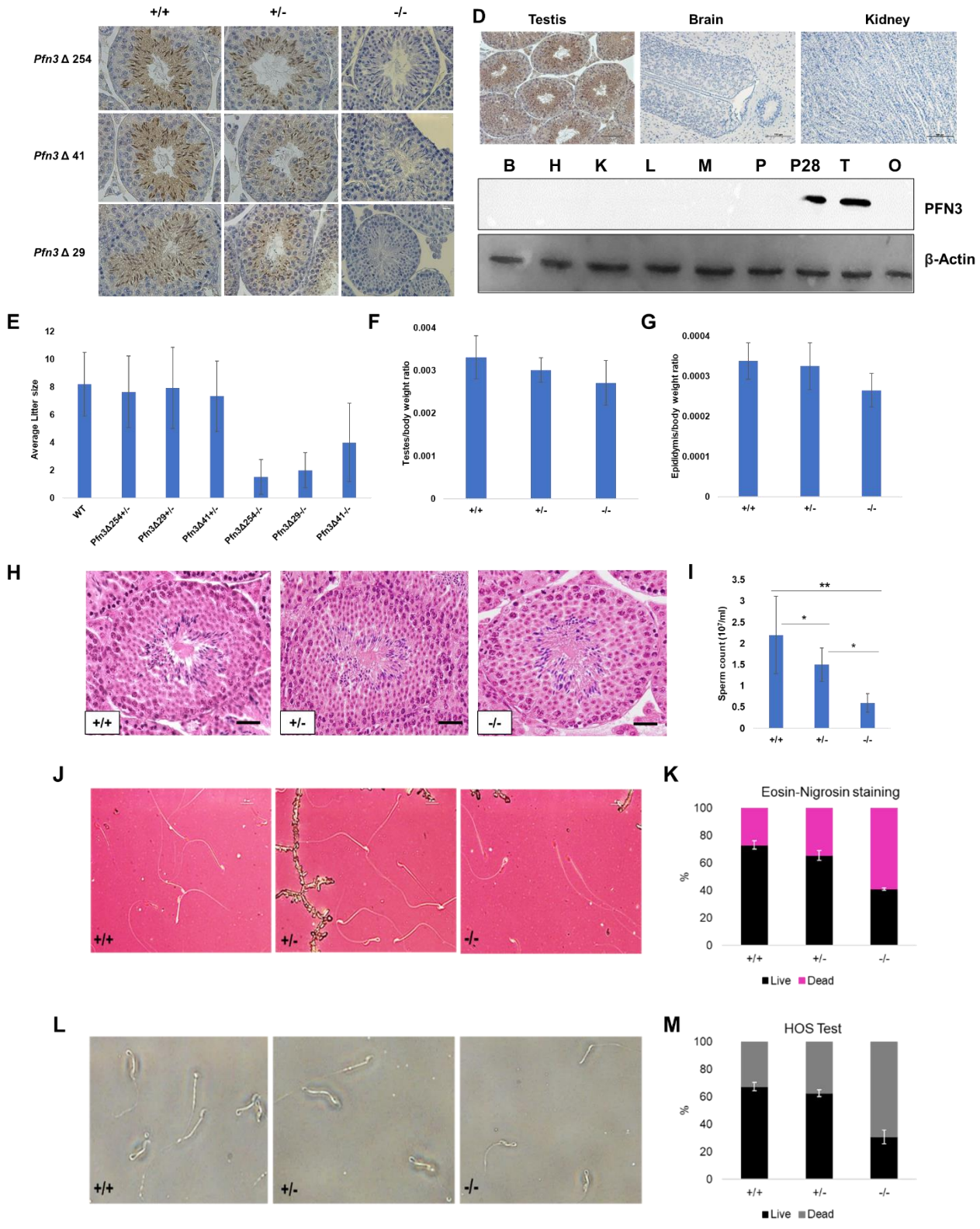

Figure 11: PFN3-Deficient mice generation and establishment. **(A)** Genotyping for *Pfn3* deficient mice (P#1, 6, 9, 13, 14 and 16 are positive for the mutation). M= 100bp Plus ladder, 414bp PCR product represents WT allele, 160bp, 373bp and 385bp PCR products represent mutant allele**. (B)** Schematic of the established *Pfn3*-deficient alleles *Pfn3*Δ254, *Pfn3*Δ41 and *Pfn3*Δ29. Orange triangle marks the cleavage site result in frame shifts in the PFN3 reading

frame leading to premature translational termination of the PFN3 protein. **(C)** Validation of *Pfn3* deficient mice. qRT-PCR was performed to check the relative expression of *Pfn3* mRNA in murine testis of wildtype, $Pfn3^{+/-}$ and $Pfn3^{-/-}$ mice for *Pfn3*Δ254, *Pfn3*Δ41 and *Pfn3*Δ29 mutation. Immunoblot against PFN3 protein following SDS gel electrophoresis of protein extracts from murine testis of $Pfn3^{+/+}$, $Pfn3^{+/-}$ and $Pfn3^{-/-}$ for each line. Beta-actin was used as control. Immunohistochemical staining of PFN3 on testicular sections of wildtype, $Pfn3^{+/-}$ and $Pfn3^{-/-}$ mice. Scale bar = 10µm. **(D)** IHC on brain, testis and kidney sections using PFN3 antibody. Scale bar = 100 µm. WB performed on various tissues isolated from mice using PFN3 antibody. B= Brain, H= heart, K=kidney, L=liver, M= muscle, P=pancreas, P28= post-natal day 28 testis, T=testis, O=ovary. **(E)** Mating statistics of wild-type, *Pfn3*Δ254, *Pfn3*Δ41, and *Pfn3*Δ29 heterozygous and homozygous (n = 5/PFN3-deficient mouse model) males. Successful mating of heterozygous and homozygous males with wild-type females was indicated by the presence of a vaginal plug at 0.5 dpc. **(F,G)** Relative weights of testes and cauda epididymis are comparable between all three genotypes of *Pfn3*Δ254 (n = 13). **(H)** H & E staining on $Pfn3^{+/+}$, $Pfn3^{+/-}$ and $Pfn3^{-/-}$ testes section. **(I)** Sperm count comparison in $Pfn3^{+/+}$, $Pfn3^{+/-}$ and $Pfn3^{-/-}$ littermates (n = 13). **(J)** Eosin and nigrosine staining of $Pfn3^{+/+}$, $Pfn3^{+/-}$ and $Pfn3^{-/-}$ sperms. Live= white sperm cells, pink=dead sperm cells**. (K)** Eosin and nigrosine staining on biological replicates (n=3) per genotype of $Pfn3^{+/+}$, $Pfn3^{+/-}$ and $Pfn3^{-/-}$ sperm. **(L)** Hypo-osmotic swelling test performed on $Pfn3^{+/+}$, $Pfn3^{+/-}$ and $Pfn3^{-/-}$ sperms. Tail curling= live sperm cells. Scale bar= 10µm. E&N staining and HOS test. **(M)** Hypo-osmotic swelling test on biological replicates (n=3) per genotype of $Pfn3^{+/+}$, $Pfn3^{+/-}$ and $Pfn3^{-/-}$ sperm. Scale bar = 10µm. At least 200 spermatozoa were evaluated per sample.

4.3 Sperm head morphology is altered in *Pfn3* deficient mice

We next used geometric morphometric analysis to analyze sperm head shape in detail. DAPI stained sperm cells showed altered head shape for $Pfn3^{-/-}$ compared to control (Figure 12 A). Analysis of 994 nuclei revealed (334 $Pfn3^{+/+}$, 289 $Pfn3^{+/-}$, 371 $Pfn3^{-/-}$), that *Pfn3* deficient sperm shows alterations in area (Figure 12 B), circularity (Figure 12 C), length of hook (Figure 12 D), bounding width (Figure 12 E) and regularity (Figure 12 F). Next, clustering was performed to categorize the sperm heads. Of note, 50% of heterozygous sperm nuclei are similar to WT, while 50% have abnormal morphology similar to *Pfn3* deficient sperm nuclei (Figure 12 G). This finding suggests a gene-dosage effect, which, however, does not seem to affect the mating success of $Pfn3^{+/-}$ males. Interestingly, 70-80% of *Pfn3* deficient sperms showed

irregular/round head morphology. Our analysis suggests that PFN3 affects the shaping of the sperm head during spermiogenesis.

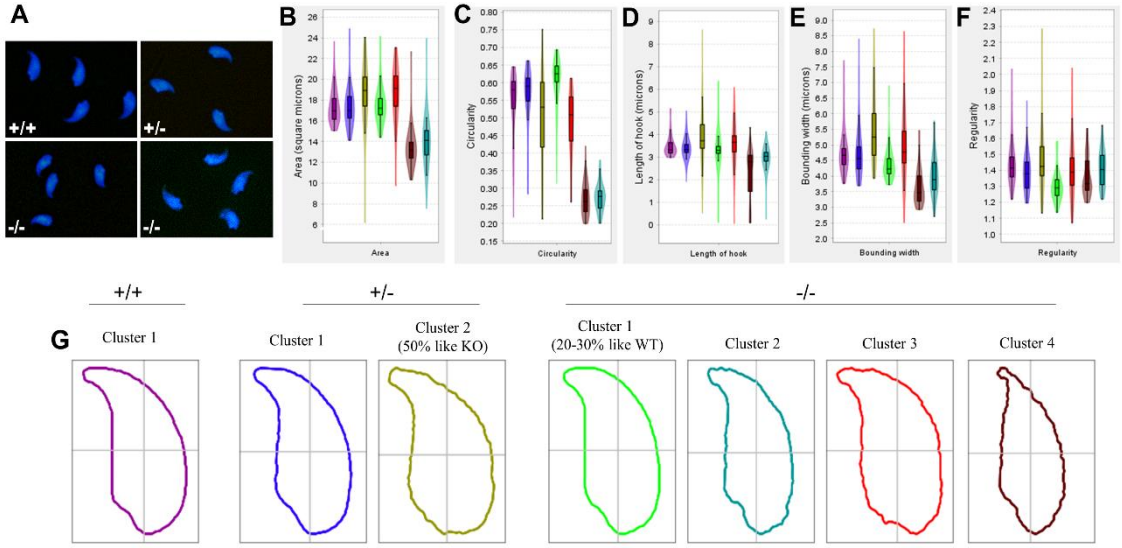

Figure 12: Amorphous nuclear morphology of sperm cells in *Pfn3* deficient mice. **(A)** Sperm cells stained with DAPI. **(B)** area, **(C)** circularity, **(D)** length of hook, **(E)** bounding width and **(F)** regularity of *Pfn3*$^{+/+}$, *Pfn3*$^{+/-}$ and *Pfn3*$^{-/-}$ sperm cells. **(G)** head shape of *Pfn3*$^{+/+}$ sperm cells, 2 clusters for *Pfn3*$^{+/-}$ sperm cells, and 4 clusters for *Pfn3*$^{-/-}$ sperm cells.

4.4 Sperm motility is reduced in *Pfn3* deficient mice

To analyze the swimming properties of *Pfn3* deficient sperm, we performed computer assisted semen analysis (CASA). Compared to WT and Het sperm samples (Table 21) *Pfn3*$^{-/-}$ sperm showed significantly reduced progressive and total motility. The other sperm motility parameters such as VCL, VSL and VAP are reduced but the difference is not significant when compared to sperm samples of controls. Of note, observed reduction in sperm motility most likely is the reason of the decreased sperm count in *Pfn3* deficient mice.

	VSL Mean (µm/s)	**VCL Mean (µm/s)**	**VAP Mean (µm/s)**	**Progressive Motility (%)**	**Motility (%)**
***Pfn3*$^{+/+}$**	62.33±1.2	218.5±11.5	122.3±4.7	47.2±1.7	59±5.9
***Pfn3*$^{+/-}$**	58.46±1.9	187±5	107±5.2	45.65±9.9	52.11±7.8
***Pfn3*$^{-/-}$**	49.57±13.8	170.857±49.14	91.39±25.03	32.388±7.4*	34.91±7.9**

Table 21: Motility parameters. Motility parameters were analyzed for *Pfn3*$^{+/+}$, *Pfn3*$^{+/}$, and *Pfn3*$^{-/-}$ sperms using OpenCASA software. (n=3/genotype). Data is presented as mean ±SD using ANOVA: Tukey's post-hoc test. VSL: straight-line velocity (µm/s); VCL: curvilinear velocity (µm/s); VAP: average path velocity (µm/s).

4.5 Impaired acrosome biogenesis in *Pfn3* deficient mice

PFN3 is detected in actin rich structures such as acrosome-acroplaxome and Golgi complex suggesting a role in acrosome biogenesis. In order to investigate the development of acrosome, we used PNA-FITC fluorescence labelling on testes sections. In tubules of wild-type (Figure 13 A) and heterozygous males (Figure 13 B), Golgi phase spermatids showed developing acrosomes forming a homogenous single cluster on the apical face of cell nuclei. In mutant spermatids, PNA staining was scattered suggesting a less uniform acrosomal compartment (Figure 13 C). This abnormal formation of the acrosome was further observed in the next step, the Cap phase. Here, the acrosome forms a cap like structure covering the anterior half on round spermatids as seen in WT (Figure 13 D) and heterozygous (Figure 13 E) sections. In *Pfn3*$^{-/-}$, the cap structures were more unevenly distributed in round spermatids (Figure 13 F). In the Acrosomal phase, as spermatids started to elongate during sperm head remodeling, these defects were more prominent, the acrosomal content failed to form an arrow like shape in elongating spermatids of *Pfn3*$^{-/-}$ mice (Figure 13 I), compared to WT (Figure 13 G) and heterozygous (Figure 13 H). These results indicate that loss of PFN3 impairs acrosomal biogenesis already at the Golgi phase.

To understand the impaired acrosome biogenesis more in detail, ultrastructure analysis using TEM was performed on developing spermatids. In the Golgi phase, proacrosomal granules originate from the *trans*-Golgi and fuse to form a single, large acrosome vesicle attaching itself in the middle of the acroplaxome on the nuclear surface as seen in WT (Figure 13 J) and heterozygous cells (Figure 13 K). However, sections of *Pfn3* deficient testes showed that the proacrosomal vesicle fail to attach in the middle of the acroplaxome and did not form a dense giant vesicle (Figure 13 L). In the Cap phase, the proacrosomal granule starts to develop and flattens over the nucleus forming the acrosomal cap, displayed in WT (Figure 16 M) and heterozygous spermatids (Figure 13 N). However, in *Pfn3* deficient testes, the acrosomal vesicle fails to form a continuous cap like structure and present as a detached granule from the acroplaxome (Figure 13 O). In the Acrosome phase, the cap continues to develop as an arrow like cover spanning the anterior two third of the nucleus as indicated in WT (Figure 13 P) and heterozygous spermatids (Figure 13 Q). Finally, at the end of Maturation phase, acrosome formation is completed (Figure 13 R, S). In *Pfn3* deficient sperm, during the Acrosomal and Maturation phase the acrosomal granule fails to develop further (Figure 13 T, U).

In order to see the acrosomal defect in mature sperm, we next analyzed epididymal sperm cells of *Pfn3* deficient males using Transmission electron microscopy (TEM) and Immunofluorescence staining (PNA-FITC). Ultrastructural analysis and acrosomal labelling revealed malformation of the acrosomal region in epididymal sperms of *Pfn3*$^{-/-}$ mice. Sperm cells present with elongating projections (highlighted by arrows), detached acrosome, abnormal acrosomal covering and impaired removal of cytoplasm (Figure 13 V). Similarly, mature sperm stained with PNA showed malformation of the acrosome in addition to abnormal sperm head morphology (Figure 16 W). Imaging of 200 spermatozoa revealed, that in *Pfn3*$^{-/-}$ male mice 51-56% of spermatozoa display malformed acrosome compared to heterozygous (18%) and WT (16%) spermatozoa (Figure 13 X, Y).

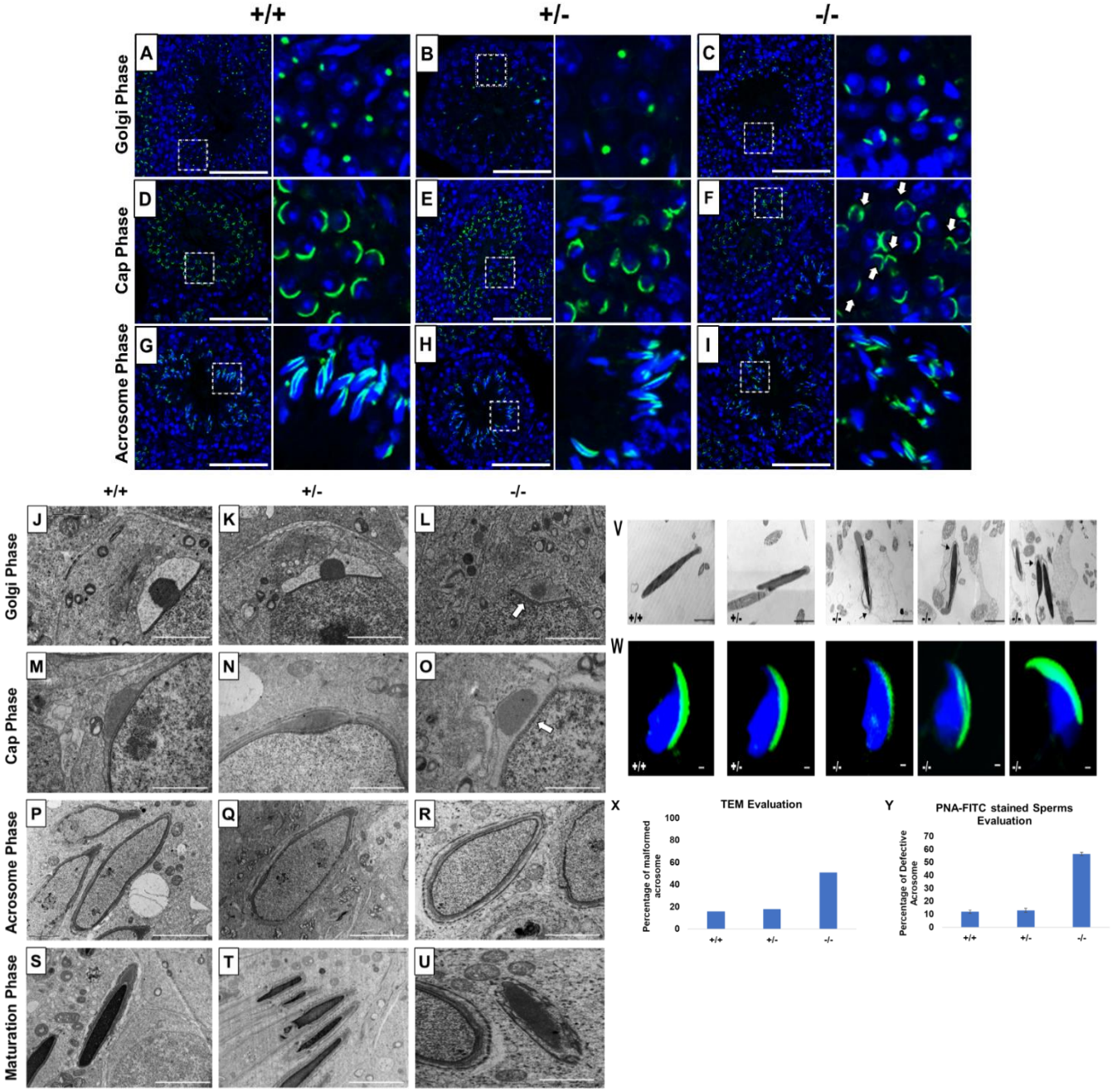

Figure 13 : Impaired acrosome biogenesis in *Pfn3* deficient mice. Adult testes sections of $Pfn3^{+/+}$(left panel), $Pfn3^{+/-}$ (Middle panel) and *Pfn3* deficient (right panel), the developing acrosome was labelled with PNA-FITC (green) and cell nuclei were stained DAPI (blue); inset panel showed the Golgi/Cap/Acrosomal phase of the tubules displayed in main panel (n=3). In the Golgi phase, proacrosomal granule (green) labelled by PNA-FITC for **(A)** $Pfn3^{+/+}$, **(B)** $Pfn3^{+/-}$ and **(C)** $Pfn3^{-/-}$ round spermatozoa. In the Cap phase, acrosomal caps (green) stained for **(D)** $Pfn3^{+/+}$, **(E)** $Pfn3^{+/-}$ and **(F)** $Pfn3^{-/-}$ round spermatozoa (white arrows showed fragmented cap structures). In the Acrosome phase, PNA-FITC labelled acrosomal area on **(G)** $Pfn3^{+/+}$, **(H)** $Pfn3^{+/-}$ and **(I)** $Pfn3^{-/-}$ elongated spermatids. Scale bar = 20 μm. TEM on developing spermatids in seminiferous tubules of $Pfn3^{+/+}$, $Pfn3^{+/-}$ and $Pfn3^{-/-}$ mice. Golgi phase spermatozoa, **(J)** $Pfn3^{+/+}$, **(K)** $Pfn3^{+/-}$, and **(L)** $Pfn3^{-/-}$ (white arrow). Cap phase spermatozoa, **(M)** $Pfn3^{+/+}$, **(N)** $Pfn3^{+/-}$, and **(O)** $Pfn3^{-/-}$ (white arrow). Acrosome phase elongating spermatids, **(P)** $Pfn3^{+/+}$, **(Q)** $Pfn3^{+/-}$, and **(R)** $Pfn3^{-/-}$. Maturation phase spermatids, **(S)** $Pfn3^{+/+}$, **(T)** $Pfn3^{+/-}$, and **(U)** $Pfn3^{-/-}$. Ultrastructure analysis using TEM revealed the acrosomal structures of $Pfn3^{+/+}$, $Pfn3^{+/-}$ and $Pfn3^{-/-}$ sperm cells. Scale bar = 2 μm. **(W)** Immunofluorescence staining using PNA-FITC (green) on epididymal sperm cells of $Pfn3^{+/+}$, $Pfn3^{+/-}$ and $Pfn3^{-/-}$ mice (n=3). Scale bar = 20 μm. **(X)** TEM evaluation shows the percentage of malformed acrosomes in $Pfn3^{+/+}$, $Pfn3^{+/-}$ and $Pfn3^{-/-}$ sperm cells. (n=2). **(Y)** Graph represents the PNA-stained defective acrosome percentage of $Pfn3^{+/+}$, $Pfn3^{+/-}$ and $Pfn3^{-/-}$ sperm cells. (n=3). 200 spermatozoa were counted per genotype.

4.6 Significant decrease of acrosome reacted sperm in *Pfn3* deficient mice

As a consequence of the malformed acrosome, we reasoned that the acrosomal reaction (AR) could be impaired. We used the A23187 to induce acrosome reaction (AR). Acrosomal status was evaluated using Coomassie staining, intact acrosomes were stained dark blue as a crescent like shape on the top of sperm head (Figure 14 A, white arrows), whereas acrosome-reacted sperm showed that the crescent like shape (acrosome) on the top of sperm head was not present (Figure 14 A, white arrow heads). The rate of A23187-induced AR was significantly reduced in *Pfn3* deficient sperm. Upon exposure to A23187, more than 60% of sperm from $Pfn3^{+/+}$ mice, and ~60% of sperm from $Pfn3^{+/-}$ mice (Figure 14 B) underwent acrosome exocytosis, whereas the AR occurred only in 37.5% of sperm from $Pfn3^{-/-}$ mice (Figure 14 B). This result indicates that the observed acrosome malformation impairs the acrosome exocytosis.

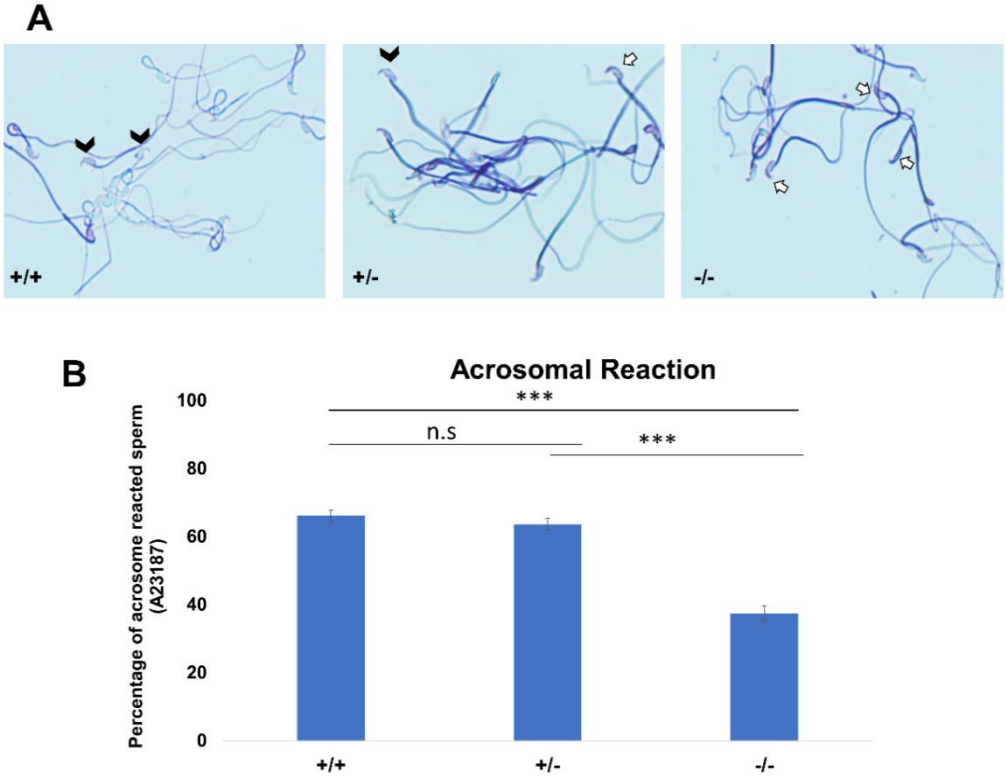

Figure 14: The acrosomal reaction (AR) using calcium ionophore. **(A)** Coomassie stained sperm cells of *Pfn3*$^{+/+}$, *Pfn3*$^{+/-}$ and *Pfn3*$^{-/-}$. Black arrow heads indicate successful acrosomal reaction took place. White arrow indicated crescent shape acrosome on sperm head indicates acrosomal reaction didn't take place. **(B)** Percentage of acrosomal reacted sperm for *Pfn3*$^{+/+}$, *Pfn3*$^{+/-}$ and *Pfn3*$^{-/-}$ (n=3 biological replicates/genotype, ***p<0.0005, student's t-test, one tail, paired).

4.7 Disrupted Golgi network in *Pfn3* deficient mice

In order to investigate the underlying mechanism of impaired acrosome biogenesis in *Pfn3* deficient mice, we performed Immunofluorescence (IF) staining by using GM130 and TGN46 antibodies, markers for *cis*- and *trans*-Golgi network respectively. GM130 plays a crucial role in vesicle tethering, fusion and maintaining *cis*-Golgi structural integrity (Tiwari et al., 2019), while TGN46 is important for formation of exocytic vesicles and secretion from the *trans*-part of the Golgi network (Huang et al., 2019). IF revealed *cis*- and *trans*-Golgi predominantly concentrated at one pole of the *Pfn3*$^{+/+}$ (Figure 15 A, D) and *Pfn3*$^{+/-}$ (Figure 15 B, E) spermatids. Whereas the *Pfn3*$^{-/-}$ spermatids showed defects and disorganization in *cis*- (Figure 15 C) and *trans*-Golgi network (Figure 15 F). These results indicate that loss of *Pfn3* leads to disruption of the Golgi sub-domains causing defects in Golgi derived proacrosomal vesicles leading to acrosome malformations.

Berruti et al. published (Berruti *et al.*, 2015) that in addition to the Golgi derived biosynthetic pathway, the endocytic pathway contributes to acrosome biogenesis. In order to check whether loss of PFN3 affects the endocytic pathway, we performed IHC staining using anti-Rab5 antibody on testis sections for all three genotypes. Rab5 is a marker for early endosomes and key factor in early endosome transport. The Rab5 mediated endo-lysosomal trafficking pathway is responsible for maturation of early endosomes to late endosomes. Interestingly, we did not observe any difference in the Rab5 staining of *Pfn3*$^{-/-}$ testis sections as compared to the *Pfn3*$^{+/-}$ and *Pfn3*$^{+/+}$ testis sections (Figure 15 G). This result suggests that in *Pfn3* deficient mice the endocytic pathway is not affected.

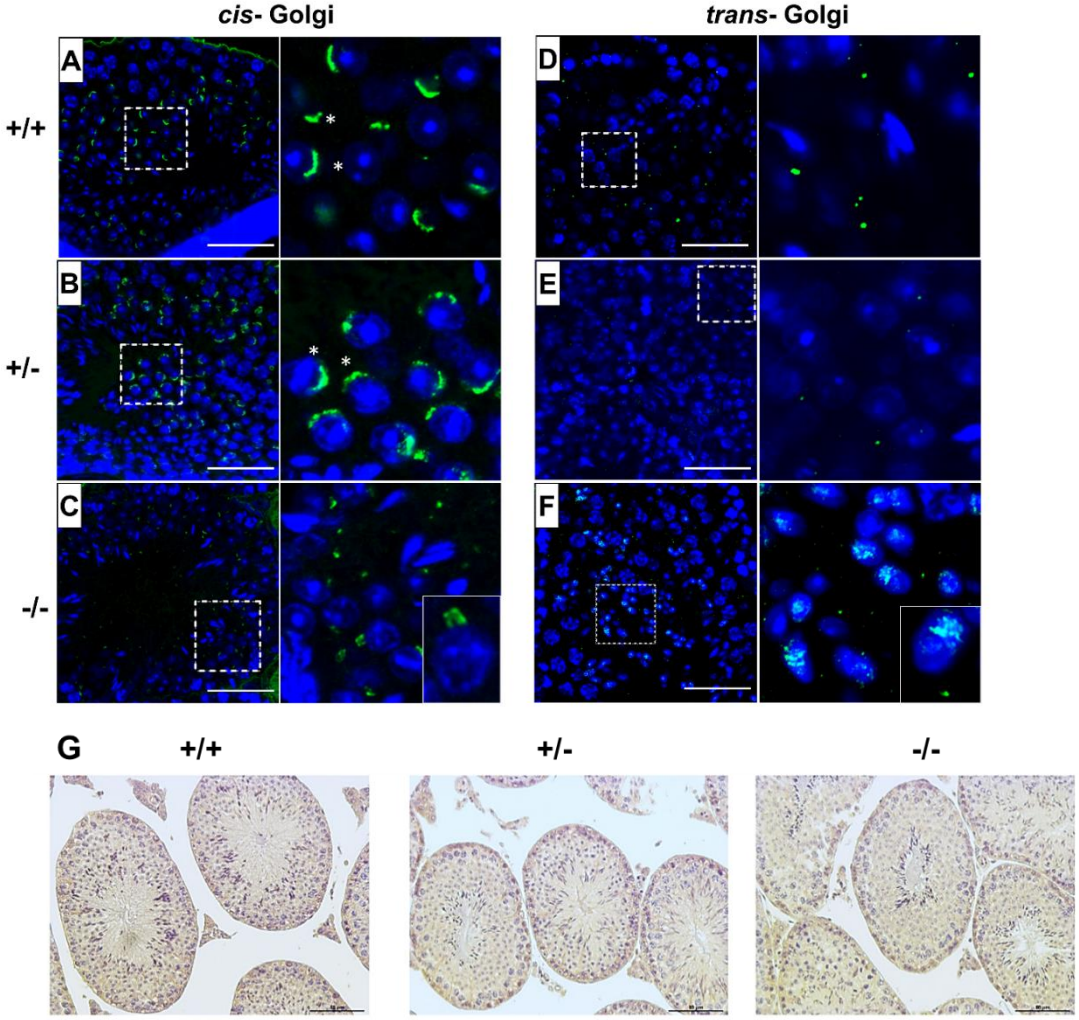

Figure 15: *Cis*-and *trans*-Golgi staining on testes sections. *Pfn3*$^{+/+}$, *Pfn3*$^{+/-}$ and *Pfn3*$^{-/-}$ testes sections stained for the *cis*- (GM130 Antibody) and *trans*- (TGN46 Antibody)-Golgi compartment (Green) and nuclei (DAPI, blue) (n=3). In **(A)** WT, **(B)** heterozygous and *Pfn3*$^{-/-}$ spermatozoa stained for *cis*-Golgi compartment (asterisks). **(D)** WT, **(E)** heterozygous, and **(F)** *Pfn3*$^{-/-}$ spermatozoa stained for *trans*-Golgi network. Scale bar = 50 µm. IHC was performed using anti-Rab5 antibody on *Pfn3*$^{+/+}$, *Pfn3*$^{+/-}$ and *Pfn3*$^{-/-}$ testes section. Scale bar = 50 µm. **(G)**

IHC was performed using anti-Rab5 antibody on *Pfn3*$^{+/+}$, *Pfn3*$^{+/-}$ and *Pfn3*$^{-/-}$ testes section. Scale bar = 50 µm.

4.8 RNA-Seq revealed alterations in expression levels of germ cell development related genes in *Pfn3*$^{-/-}$ mice

Since the function of PFN3 is only begun to be understood we set out to identify whether deletion of *Pfn3* impinges on global gene expression and performed RNA-sequencing on total RNA isolated from testes of *Pfn3*$^{+/+}$, *Pfn3*$^{+/-}$ and *Pfn3*$^{-/-}$ mice. RNA-sequencing identified 38 significantly differentially expressed (DE) genes with log2 fold change > 1.5 in *Pfn3*$^{-/-}$ as compared to control (Figure 16 A). In total, 27 genes were found to be upregulated and 11 genes to be down regulated in *Pfn3*$^{-/-}$ testes compared to wildtype (Figure 16 B). Tukey's multiple comparison ANOVA was used to check for statistics and all groups showed non-significant difference. Quantitative real-time PCR was used to validate the results for 13 of the DE genes which are related to male fertility. *Cfl1, Trim27, B3gnt9, Mul1, Hhatl* were up-regulated while *Exosc1, Srsf9, Atg2a, Copa, Slc25a36, Sap30, Dpm2* and *Qrich1* were down-regulated in *Pfn3*$^{-/-}$ mice (Figure 16 C). These results indicated that deletion of *Pfn3* disrupts the expression of genes involved in actin cytoskeletal dynamics, regulation of autophagy, mitochondrial and Golgi network structural integrity. In order to check, that the results observed are not skewed due to a defect in spermiogenesis in the PFN3 deficient mice, we tested for expression levels of marker genes indicative for Leydig cells, Sertoli cells and Spermatogonia. Box plots of marker genes for the different cell types are given in (Figure 16 D) and reveal that overall quantity and development of sperm cells are not affected in *Pfn3*$^{-/-}$ mice.

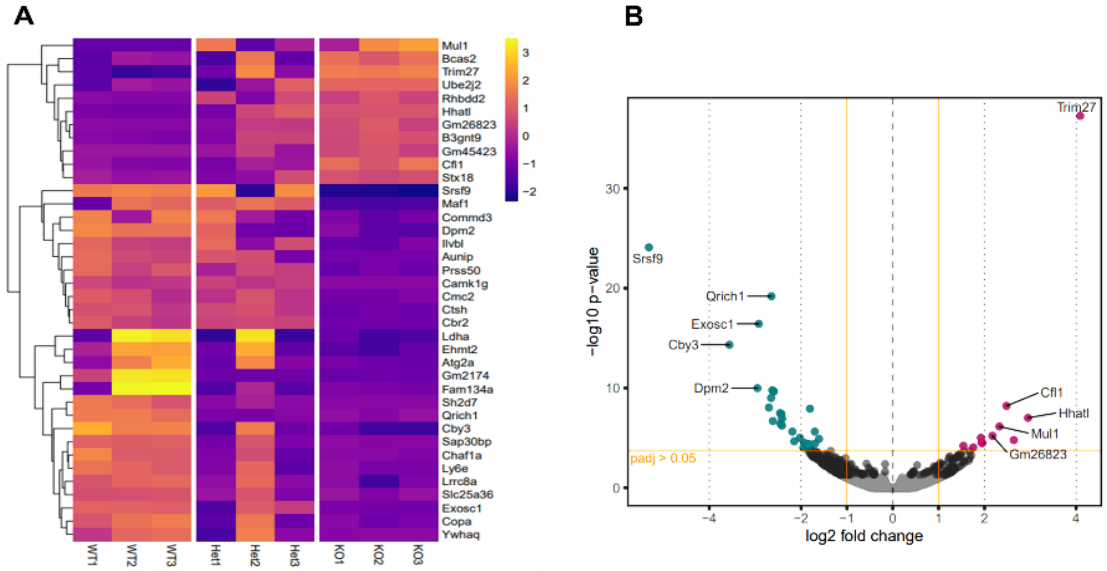

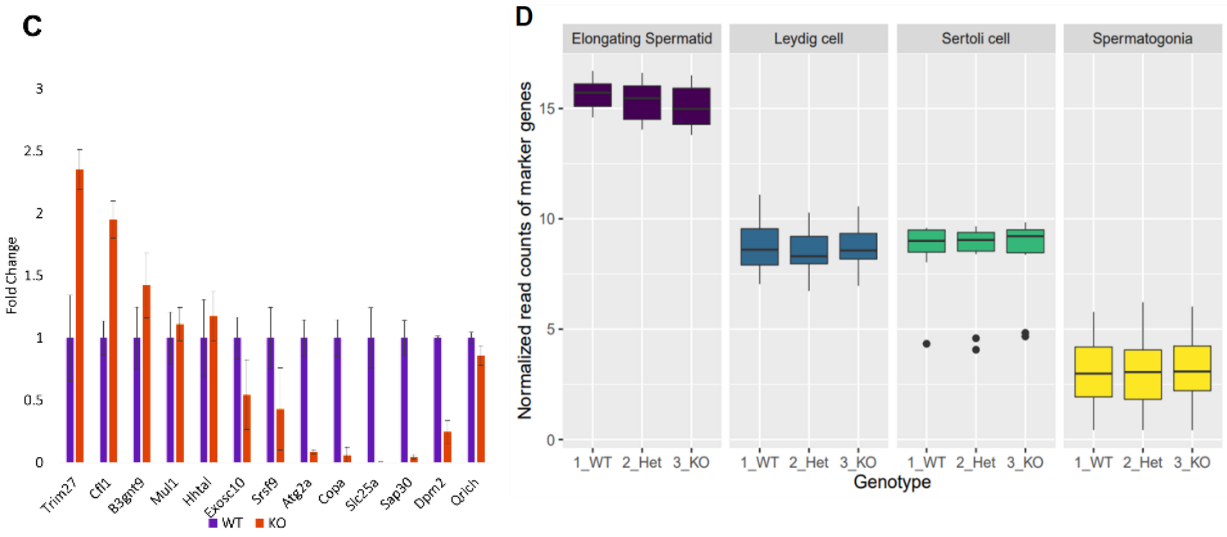

Figure 16: Changes in gene expression profile of *Pfn3* deficient mice. (**A)** Heat map visualization of top 38 differentially expressed (DE) genes obtained by RNA seq on $Pfn3^{+/+}$, $Pfn3^{+/-}$ and $Pfn3^{-/-}$ testes. **(B)** Volcano plots displaying DE genes for $Pfn3^{+/+}$ vs $Pfn3^{-/-}$ (adjusted p-value< 0.05, log2 fold change of expression (LFC) > 1.5). **(C)** DE genes obtained by RNA seq were verified by qRT-PCR on $Pfn3^{+/+}$, $Pfn3^{+/-}$ and $Pfn3^{-/-}$ testicular RNA. (n=3 biological replicates/genotype). **(D)** Box plot of normalized read counts of marker genes in different cell types for all three genotypes. In elongating spermatozoa transition nuclear proteins and protamine's were used as a marker. Markers indicative for Leydig cells, Hsd17b3, Fabp3, Star, Insl3, Cyp11a1 and Cyp17a1, Sertoli cells Amhr2, Aard, Defb36 and Cst12 were used as markers, spermatogonia, Zbtb16, Plzf, Gfra1, Nanos3 and Lin28a were used.

4.9 Autophagic flux and AMPK/mTOR signaling pathway are affected in *Pfn3* deficient mice

The RNA-Seq analysis revealed *Trim27* as the most upregulated gene in *Pfn3* deficient mice. Overexpression of *Trim27* leads to activation of AKT signaling (Zhang et al., 2018). AKT in turn is an activator of mTOR (Hahn-Windgassen et al., 2005). Autophagy is regulated by AMPK/mTOR signaling pathways, with AMPK being stimulating and mTOR being repressive (Liang et al., 2018). Next, we were interested to determine whether the signaling pathways downstream of *Trim27* responsible for regulation of autophagy are affected in *Pfn3* deficient mice. Indeed, immunoblotting showed increased protein levels for mTOR and phospho-mTOR, while the level of phospho-AMPKα was reduced (Figure 17 A). Increased level of phospho-mTOR was validated by IHC in *Pfn3* deficient mice (Figure 17 B). So, these data

suggest, that loss of *Pfn3* leads to an upregulation of *Trim27*, which results in activation of mTOR signaling (Zhang et al., 2018) (Hahn-Windgassen et al., 2005) (Liang *et al*., 2018) causing a decrease in p-AMPKα resulting in the disruption of autophagy. Further the autophagic gene *Atg2a* was expressed at lower levels in *Pfn3* deficient mice. *Atg2a* is involved in the phagophore elongation leading to the formation of the autophagosome (Bozic et al., 2020). The elongation step is completed by the conjugation of LC3B, known as microtubule, associated protein and a widely used marker for autophagosomes (Tang et al., 2017). LC3B is a core protein in the autophagic flux where it functions as an autophagic cargo by interacting with an autophagic substrate SQSTM1/p62 (Tang et al., 2017). It is well established that depletion of *Atg2a* results in blocking of autophagic flux leading to accumulation of LC3B and SQSTM1 (Bozic et al., 2020). Therefore, we analyzed LC3B and SQSTM1 protein levels. Interestingly in *Pfn3* deficient testes levels of LC3B were increased as shown by WB and IHC and WB (Figure 17 A, C respectively). We further found and accumulation of SQSTM1 in testes of *Pfn3* deficient using WB (Figure 17 A). Quantification of protein levels (Figure 17 C) revealed an increase in LC3B, p62, p-mTOR and mTOR levels, and reduction of ATG2a and AMPK. So, we hypothesized that deletion of *Pfn3* results in upregulation of *Trim27*, which leads to mTOR mediated inhibition of autophagy hallmarked by lower levels of *Atg2a*. As a consequence, autophagic flux stalls, indicated by accumulation of LC3B and SQSTM1. This might cause the disturbance of the acrosome formation in *Pfn3* deficient mice.

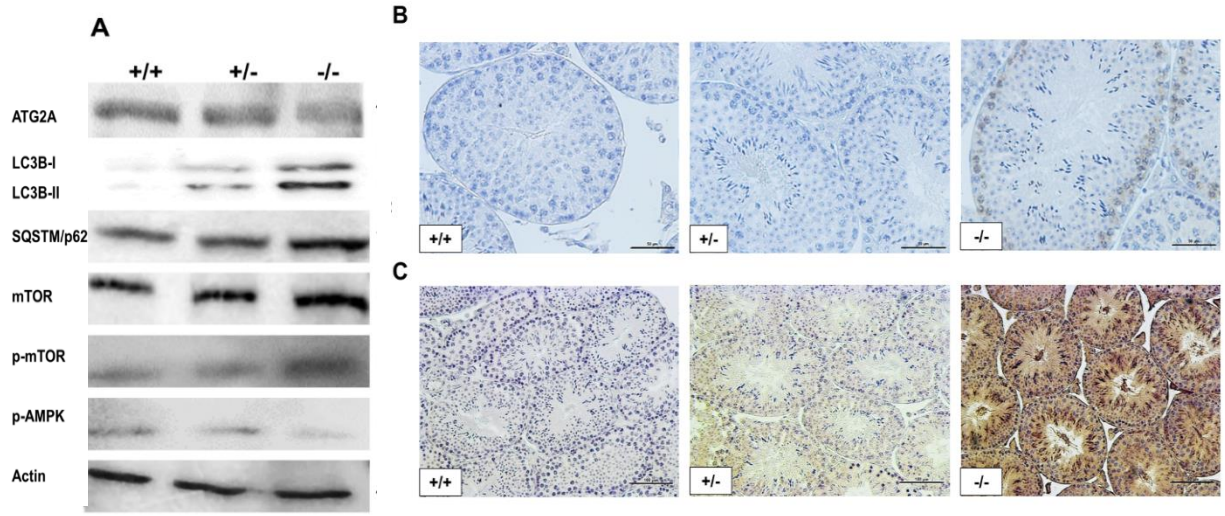

D

.

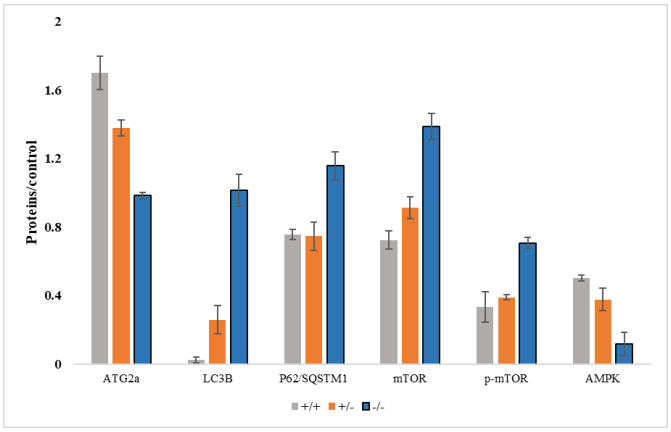

Figure 17: Disruption in autophagic flux and AMPK/MTOR signaling pathway of *Pfn3* deficient mice. **(A)** Immunoblot analysis against ATG2A, LC3B, SQSTM1, mTOR, phospho-mTOR and phospho-AMPKα on protein lysates from *Pfn3*$^{+/+}$, *Pfn3*$^{+/-}$ and *Pfn3*$^{-/-}$ testes. **(B)** Immunohistochemical staining against phospho-mTOR on *Pfn3*$^{+/+}$, *Pfn3*$^{+/-}$ and *Pfn3*$^{-/-}$ testes sections (Top row). **(C)** Immunohistochemical staining against LC3B on *Pfn3*$^{+/+}$, *Pfn3*$^{+/-}$ and *Pfn3*$^{-/-}$ testes sections (Bottom row). Staining of testicular tissue sections from *Pfn3*$^{+/+}$ (left column), *Pfn3*$^{+/-}$ (middle column) and *Pfn3*$^{-/-}$ (right column) animals is shown. Scale bar = 100 µm. **(D)** Quantification of protein levels in all three genotypes. ATG2a and AMPK relatively quantified showing decreased protein levels in *Pfn3* deficient mice compared to controls. Similarly, LC3B, P62/SQSTM1, mTOR and p-mTOR protein levels are increased in *Pfn3* deficient mice indicating inhibition in autophagy.

4.10 PFN3 interacts with TRIM27

Next, we used co-immunoprecipitation (Co-IP) to test whether PFN3 and TRIM27 interact. From whole testis lysate a PFN3-specific antibody pulled down TRIM27 (Figure 18 A, lane 3) the IP with a TRIM27 antibody was able to capture and elute PFN3 (not shown). The specificity of the assay was confirmed by using protein extraction buffer as a negative control (Figure 18 A, lane 2); whole testis lysate was used as an input control (Figure 18 A, lane 1). To validate this interaction, reciprocal antibodies on immunoblot (Figure 18 B) showed PFN3 (~14KDa) and TRIM27 (~58KDa) proteins from input control (lane1), Co-IP (lane 2), flow through (lane 3) and negative control.

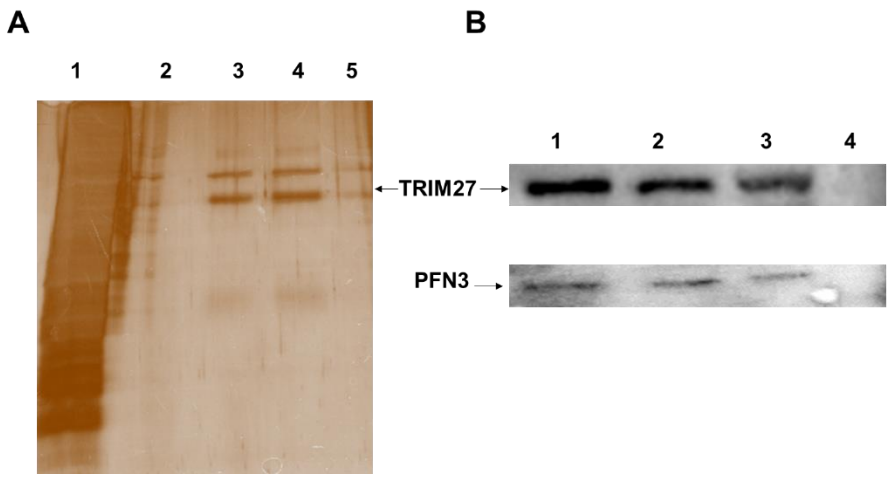

Figure 18: Co-immunoprecipitation using anti-PFN3 and anti-TRIM27 antibody on testis lysates. **(A)** Silver stained SDS-PAGE; lane 1: input control (protein lysate), lane 2: negative control (only antibody), lane 3: IP using PFN3 antibody, lane 4: IP using PFN3 antibody, lane 5: flow through. **(B)** Western blot showed PFN3 and TRIM27 proteins. Lane 1: Input control . Lane 2: Immunoblot of reciprocal IP for TRIM27 (band observed at ~58kDa) and PFN3 protein levels (band observed at ~14kDa) using anti-PFN3 and anti-TRIM27 antibody respectively. Lane 3: Flow through. Lane 4: Negative control.

4.11 *Pfn3* deficient mice exhibit increased protein levels of ADF/CFL variants compared to WT

Further, the expression of cofilin1 (*Cfl1*) was upregulated in *Pfn3* deficient testes. We decided to check protein levels using WB for the cofilin traditional proteins (CFL1, CFL2 and ADF) known as actin binding proteins. The level of ADF protein was increased in *Pfn3*$^{-/-}$ testes while CFL1 and CFL2 (Figure 19 A) protein levels were already increased in heterozygous testes.

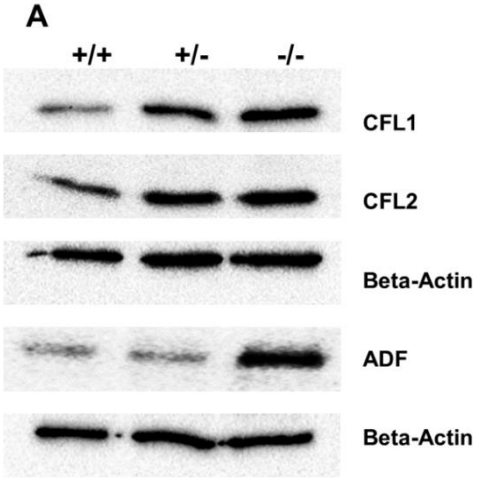

Figure 19: Immunoblotting against ADF, CFL1 and CFL2 on protein lysates from *Pfn3*$^{+/+}$, *Pfn3*$^{+/-}$ and *Pfn3*$^{-/-}$ testes.

4.12 PFN3 binding protein is lost in nuclear fraction of sperm

PFN3 is detected in a complex with ARPM1 specifically in the sperm nucleus, however, not in the cytoplasm (Hara et al., 2008). In sperm cytoplasm of *Pfn3*$^{-/-}$ mice still moderate signal of ARPM1 can be detected (Figure 20 A). We performed WB using anti-ARPM1antibody on proteins isolated from cytoplasmic and nuclear fractions of both testes and sperm. Western blot showed that ARPM1 could not be detected in the nuclear fraction of *Pfn3* deficient testes and sperm, while cytoplasmic ARPM1 protein levels in testes are slightly reduced in *Pfn3* deficient mice (Figure 20 A).

These findings were further confirmed by Immunohistochemistry, the nucleus of spermatozoa in testes of *Pfn3* deficient mice were devoid of ARPM1 (Figure 20 B). This finding suggests that loss of PFN3 destabilizes the PFN3-ARPM1 complex, leading to loss of ARPM1 in the nuclei of *Pfn3* deficient sperm.

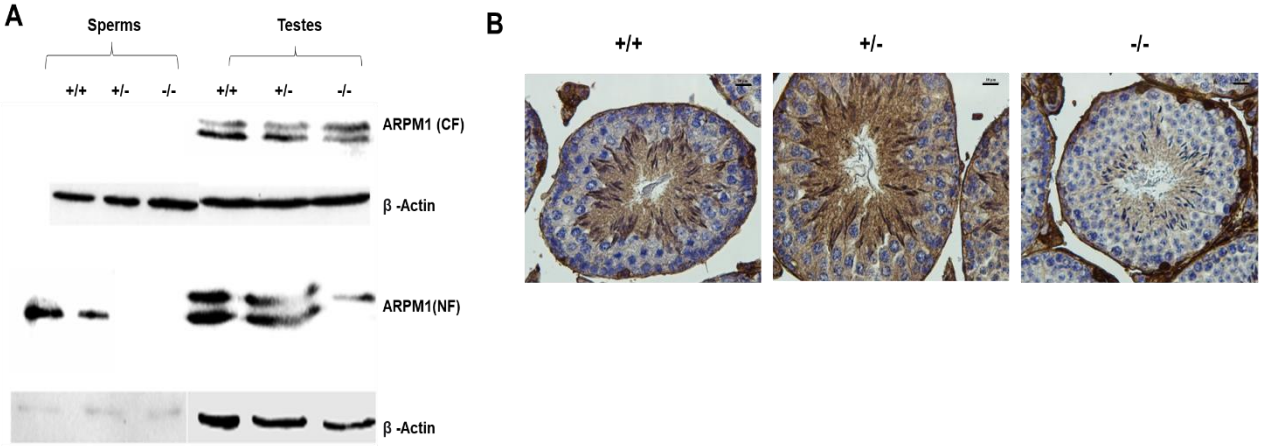

Figure 20: Western blot analysis and IHC (immunohistochemical analysis) was performed using anti-ARPM1 antibody. **(A)** Western blot analysis of cytoplasmic and nuclear fraction from mice of *Pfn3*$^{+/+}$, *Pfn3*$^{+/-}$ and *Pfn3*$^{-/-}$ sperm and testes. **(B)** Immunohistochemical analysis using anti-ARPM1 antibody on *Pfn3*$^{+/+}$, *Pfn3*$^{+/-}$ and *Pfn3*$^{-/-}$ testes sections. Scale bar = 10 µm.

4.13 F-Actin organization is not altered in *Pfn3* deficient sperm

Pfn3 binds to actin monomers and plays a role in actin polymerization. Actin is mainly located in the mid piece of sperm flagellum suggesting a role in sperm motility, elasticity, and membrane integrity. F-Actin is present as a helical structure (Gervasi et al., 2018) which is in parallel with the organization of the mitochondrial sheath in mouse sperm (Amaral et al., 2013). We wanted to see whether the *Pfn3* deletion affects the actin cytoskeleton organization in the sperm. Phalloidine Atto-647 fluorescence staining revealed that actin assembly was not altered in the mid piece of $Pfn3^{-/-}$ sperm (Figure 21). This result suggests that loss of PFN3 doesn't affect the actin assembly in $Pfn3^{-/-}$ sperm.

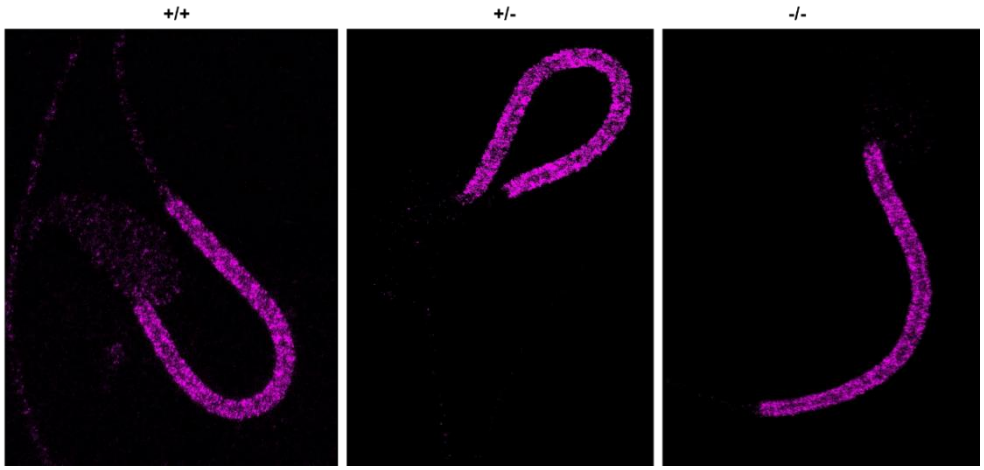

Figure 21: Stimulated emission depletion (STED) microscopy was performed on mature sperm flagellum of $Pfn3^{+/+}$, $Pfn3^{+/-}$ and $Pfn3^{-/-}$ mice to detect the actin polymerization by using Phalloidine Atto-647 fluorescence. Scale bar = 2μm.

4.14 Abnormal manchette development in *Pfn3* deficient mice

We found PFN3 localized in the manchette complex of the developing spermatid. In order to investigate whether abnormal head morphology of *Pfn3* deficient sperm was due to the alteration in manchette structure or formation, we performed an Immunofluorescence staining using alpha tubulin for step-by-step comparison on the germ cell population isolated from testes. Tubulin staining revealed that in WT and heterozygous spermatids (Figure 22 A, B) manchette was forming the proper skirt like structure while the manchette was not properly covering and constricted overly at the posterior region in *Pfn3* deficient round spermatids (Figure 22 C). This abnormal manchette development is more obvious in the later steps of development (step 9-13) in *Pfn3* deficient spermatids. We conclude that deletion of PFN3 leads

to disruption of manchette formation which in turn contributes to the abnormal shape of the sperm head and flagellar defects in *Pfn3* deficient sperm.

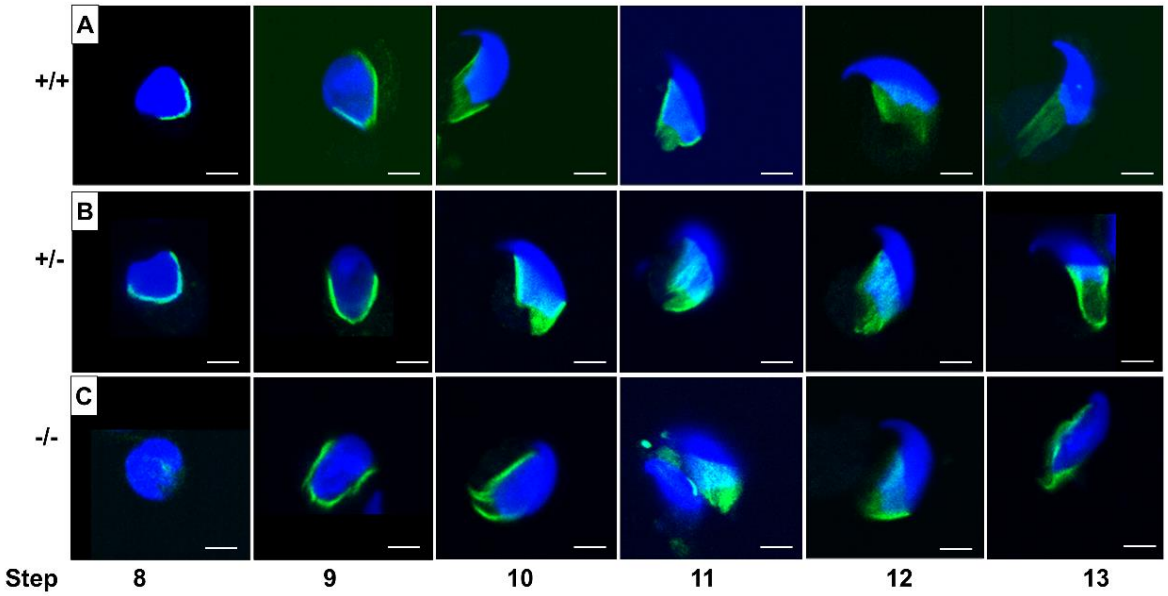

Figure 22: Manchette structure stained by using α-tubulin antibody (green) on germ cell population isolated from **(A)** *Pfn3*$^{+/+}$, **(B)** *Pfn3*$^{+/-}$ and **(C)** *Pfn3*$^{-/-}$ testes (n=3/genotype). Nuclei were stained with DAPI (blue). Scale bar = 20 μm.

4.15 *Pfn3* deficient sperm display flagellar deformities

Since we detected low sperm motility in *Pfn3* deficient mice, we analyzed sperm flagella structure. We used MitoRed Immunostaining to assess the mitochondrial sheath in the mid piece of sperm flagella. While MitoRed uniformly stained the mitochondrial sheath in spermatozoa of WT (Figure 23 A) and heterozygous (Figure 23 B), *Pfn3* deficient sperm flagella showed a variety of aberrations spanning from abnormally thick mid piece (Figure 23 C), slightly tapered bent thick neck (Figure 23 D) and cytoplasmic droplets with amorphous sperm heads (Figure 23 E). This suggests that loss of PFN3 resulted in flagellar deformities due to mitochondrial disorganization. In addition, defective manchette results in disrupted intra-manchette transport, which might also lead to the flagellar abnormalities.

Next, we performed transmission electron microscope (TEM) on mature sperm isolated from cauda epididymis to analyze whether the mid piece of sperm have normal axonemal and mitochondrial structure. TEM of *Pfn3* deficient sperm showed several ultrastructural defects, like plasma membrane not covering uniformly the mitochondrial sheet (Figure 23 H),

disorganized or vacuolated mitochondria (Figure 23 I, asterisk), axonemal fibrous sheet enclosed two or more mitochondria and axonemal flagellar complex (Figure 23 J) compared to WT (Figure 23 F) and heterozygous sperm ultrastructure (Figure 23 G). Scanning electron microscope (SEM) showed similar sperm abnormalities in *Pfn3* deficient mice, thick sperm mid pieces with distal cytoplasmic droplets (Figure 23 M, N) compared to WT (Figure 23 K) and heterozygous sperm (Figure 23 L). This result correlates with the previous (MitoRed and TEM ultrastructural sperm analysis) findings. These findings showed that sperm from *Pfn3* deficient mice display an abnormal morphology of mitochondrial and axonemal fibrous sheet. Statistical analysis revealed that the percentage of deformed sperm flagella in *Pfn3* deficient mice (~55%) compared to WT and heterozygous sperm was significantly higher (Figure 23 O). We speculate that these defects contribute to the reduced sperm motility. Altogether our results indicate that loss of PFN3 located in mitochondria resulted in sperm flagellar defects and further support a cytoplasm removal defect.

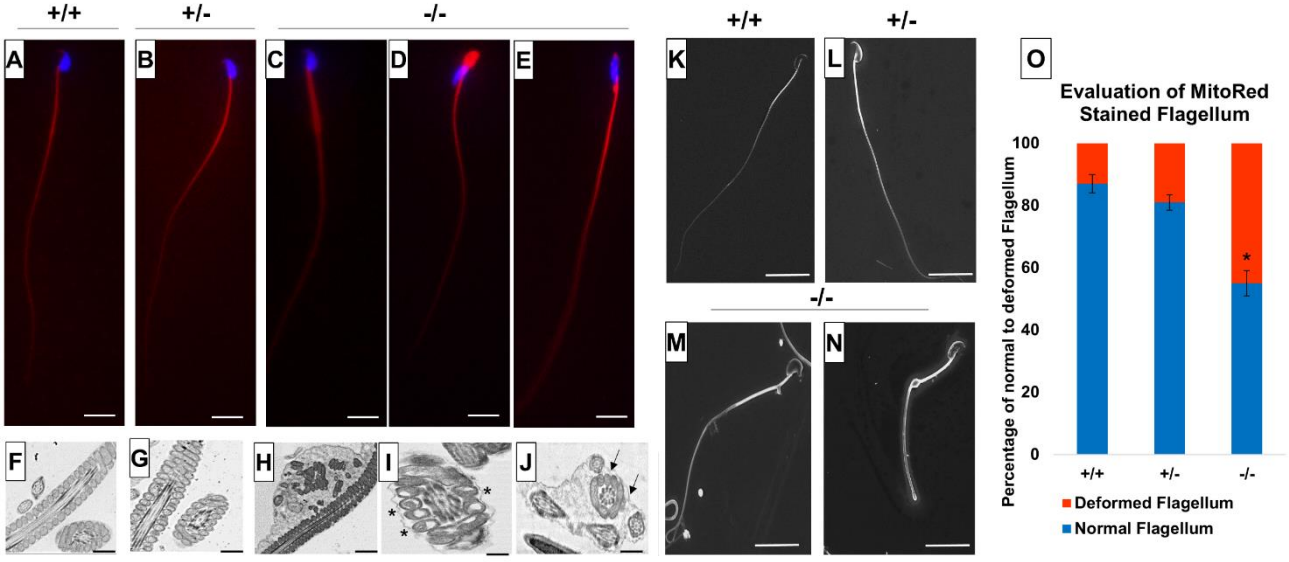

Figure 23: Flagellum analysis on mature sperm cells from *Pfn3*$^{+/+}$, *Pfn3*$^{+/-}$ and *Pfn3*$^{-/-}$ mice. MitoRed staining (Red) of sperm flagellum on **(A)** *Pfn3*$^{+/+}$, **(B)** *Pfn3*$^{+/-}$, and **(C), (D), (E)** *Pfn3*$^{-/-}$ sperm cells isolated from cauda epididymis. Scale bar=10 µm. Ultrastructural analysis using TEM on **(F)** *Pfn3*$^{+/+}$, **(G)** *Pfn3*$^{+/-}$, and **(H), (I), (J)** *Pfn3*$^{-/-}$ sperm cells isolated from cauda epididymis. Vacuolated mitochondria shown by asterisk and fibrous sheet contained more than one axoneme-mitochondrial complex shown by arrows. Scale bar = 5 µm. Surface analysis using SEM on **(K)** *Pfn3*$^{+/+}$, **(L)** *Pfn3*$^{+/-}$, and **(M), (N)** *Pfn3*$^{-/-}$ mature sperm cells isolated from cauda epididymis. Scale bar = 50 µm. **(O)** Statistical analysis of MitoRed stained flagellum of

Pfn3$^{+/+}$, *Pfn3*$^{+/-}$, and *Pfn3*$^{-/-}$ sperm cells. Data is presented as mean ±SD using ANOVA: Tukey's post-hoc ($p < 0.05$*).

5. DISCUSSION I

Pfn3 has multiple physiological roles in sperm formation and function. In this study we have shown that deletion of *Pfn3* results in male subfertility hallmarked by reduced sperm count/vitality with sperm displaying type II- globozoospermia. *Pfn3* deficient mice display an impaired acrosome biogenesis followed by malformed acrosomal covering on mature spermatozoa including cytoplasm removal defects, abnormal manchette development contributing to amorphous head shape of sperm and flagellar deformities resulting in reduced sperm motility. In addition, loss of *Pfn3* disturbs the morphology of Golgi sub-domains resulting in abnormal formation of Golgi derived vesicles. Further, we found by co-IP that PFN3 interacts with TRIM27 play a role in autophagy for acrosome development. Mechanistically we found a deregulation of autophagy master regulators (*Trim27,* AMPK, mTOR, *Atg2a,* LC3B and SQSTM1) which seem to relate the disruption of acrosome formation in *Pfn3* deficient germ cells.

The first and foremost effect of deleting *Pfn3* was impaired acrosome development due to defective vesicle transport from Golgi. Golgi complexes were disorganized and not oriented correctly leading to an impaired post Golgi trafficking. Acrosome labelling in *Pfn3* deficient testes revealed, that acrosome biogenesis was affected in the Golgi phase of development. The underlying defect was the failure of proacrosomal granule formation and fusion. Loss of *Pfn3* affected the transport of vesicles released from Golgi complexes in *Pfn3* deficient mice. It is known that profilin1 is found in the Golgi compartment (Dong et al., 2000) and profilin2 is associated with proteins which play a role in membrane trafficking (Gareus et al., 2006).

The formation of the acrosome uses elements of the autophagy machinery which are involved in the fusion/transportation of Golgi derived proacrosomal vesicles (Wang et al., 2014). We demonstrate that deletion of *Pfn3* leads to upregulation of *Trim27*, which leads to activation of mTOR. This, in turn leads to repression of AMPK. Together, higher mTOR and lower AMPK leads to an attenuation of autophagy hallmarked by lower levels of *Atg2a.* As a consequence, autophagic flux stalls, indicated by accumulation of LC3B and SQSTM1. This causes the developmental arrest of the acrosome formation in *Pfn3* deficient mice. Disruption of autophagic flux leading to failure of proacrosomal granule formation is also reported in mice deficient for *Sirt1* (Liu et al., 2017) and *Atg7* (Wang et al., 2014). Interestingly, in *Atg7* mutants,

LC3B levels are increased, but AMPK and mTOR levels remain unaffected (Wang et al., 2014). However, in *Sirt1* mutants autophagic flux is partially disrupted by the accumulation of acetylated LC3B in the nucleus (Liu et al., 2017). This suggests, that ATG7 and SIRT1 act further downstream in the autophagic cascade compared to *Pfn3.*

We demonstrate that loss of *Pfn3,* leads to an upregulation of *Trim27*. So, we speculate, that *Pfn3* directly or indirectly interacts with or is tethered to *Trim27* to modulate its activity during spermiogenesis. In fact, the interaction was demonstrated using co-immunoprecipitation. So, we hypothesize that lack of *Pfn3* unleashes *Trim27* leading to i) enhanced expression of *Trim27* which initiates a cascade resulting in ii) impaired acrosome development.

In addition, acrosome labelling, and evaluation of transmission electron microscopy showed malformed/fragmented acrosomes in 50-60% of mature epididymal *Pfn3* deficient sperm. Besides defective acrosome morphology of mature spermatozoa, 70% of *Pfn3* deficient sperms showed amorphous head shape lacking the typical hook area and circularity. We demonstrated that the development of the manchette is disturbed in *Pfn3* deficient sperm. Defective manchette development leading to abnormal shaping of sperm head is also reported in *Katnb1, Sun4, Lrguk1, Kif3A, Hook1*, and *Kash* mutants. Intriguingly these genes interact with the microtubule network and the proteins are localized in the microtubular manchette (Mendoza-Lujambio et al., 2002)(Lehti et al., 2013)(O'Donnell et al., 2012)(Gunes et al., 2020). The manchette is connected to the nucleus by fuzzy material/linkers, which indicates that manchette and nucleus possess a structural relationship through which they exert forces on each other for the shaping of sperm head (Russell et al., 1991). This suggest that loss of microtubular proteins in the manchette disturbs the structural relationship between manchette and nucleus resulting in abnormal sperm head development. The fact, that PFN3 is localized to the microtubules of the manchette, and loss of PFN3 results in manchette deformities suggests that PFN3 contributes to the organization and remodeling of the manchette for sperm head shaping. Impaired manchette might also contributed to the flagellar defects due to affected IMT.

The fact, that the sperm count is significantly reduced is most likely due to the observed motility defect and the use of swim-out method for sperm count.

Further, *Pfn3* deficient sperm showed significant reduction in progressive motility as well as cytoplasmic removal defects. Vacuolated mitochondria result in the deformities in the flagellum leading to the reduced motility. Sperm motility is the outcome of flagellar movement

of sperm tail, gained by ATP driven energy produced by mitochondrion located in sperm mid piece (Tourmente et al., 2015). Sperm flagellum deformities lead to poor sperm motility and abnormal flagellum structure as seen in other knockout mouse models such as TSSK4, QRICH2 and CABYR (Shen et al., 2019)(Lehti and Sironen, 2017). This suggest that deformities of the flagellum led to the reduced motility in *Pfn3*$^{-/-}$ mice, however caused by a yet unexplained mechanism.

To our surprise we observed unaltered F-actin organization in *Pfn3* deficient sperm. This suggests that the role of *Pfn3* in actin polymerization is rather minor.

Hara *et al.,* showed that in the nuclei of spermatids ARPM1 binds to PFN3, while, cytoplasmic ARPM1 does not. The ARPM1-PFN3 complex contributes to spermatid head shaping (Hara et al., 2008). We found that lack of PFN3 led to the loss of ARPM1 in spermatid nuclei. We hypothesized that PFN3 is required for the stabilization or localization of ARPM1 in nuclei of the spermatids. So, the abnormal sperm nuclear morphology observed in *Pfn3* deficient mice might be a consequence of lack of testes specific PFN3-ARPM1 complex. In addition, ARPM1 protein was detected in the cytoplasm of testes since ARPM1-PFN3 complex is only restricted to sperm nucleus which further confirms Hara *et al.,* findings (Hara et al., 2008).

Further, *Srsf9, Slc25a36, Prss50 and Copa* are downregulated in our *Pfn3* deficient mice. Bansal *et al.,* reported that patients with reduced sperm motility known as asthenozoospermia display lower levels of *Srsf9* (Bansal et al., 2015). Additionally, *Slc25a36* is a member of solute carrier super family, and known to regulate mitochondrial function. It is reported by Xin *et al.,* that *Slc25a36* deficiency led to impaired mitochondria and decreased mitochondrial membrane potential (Xin et al., 2019). PRSS50 and COPA are involved in male fertility and Golgi trafficking respectively (Sleutels et al., 2012)(Custer et al., 2019). Downregulation of PRSS50, resulted in reduced male fertility (Sleutels *et al.,* 2012). Moreover, knockdown of COPA impairs Golgi-ER trafficking (Tang et al., 2015). We reported severely reduced male fertility and sperm motility, malformed mitochondria and disturbed Golgi derived vesicles in *Pfn3* deficient mice. In addition, we observed that *Mul1* is upregulated in *Pfn3* deficient testes. *Mul1* is essential for maintaining the mitochondrial morphology (Li et al., 2015). We found vacuolated mitochondria in sperm flagellum of *Pfn3* deficient mice. These findings suggest that loss of *Pfn3* results in differentially expressed genes leading to reduced sperm motility and flagellar deformities.

Taken together, our findings demonstrate that *Pfn3* affects multiple processes during spermiogenesis. We summarize our findings related to the role of PFN3 in vesicle transport from Golgi to nucleus for acrosome biogenesis in Figure 24. Lack of PFN3 causes a disruption of Golgi sub-domains leading to impaired acrosome biogenesis. On a molecular level, loss of PFN3 leads to upregulation of *Trim27*, resulting in deregulation of mTOR and AMPK signaling leading to a disruption of autophagic flux. Further, we show that loss of *Pfn3* causes abnormal manchette development and loss of ARPM1 in sperm nucleus. We detected vacuolated mitochondria in the flagellum. This might lead to reduced sperm motility in *Pfn3* deficient mice. In conclusion, our study highlights the requirement of *Pfn3* during spermiogenesis specifically in acrosome biogenesis and adds this gene to the growing catalog of genes potentially involved in human male infertility.

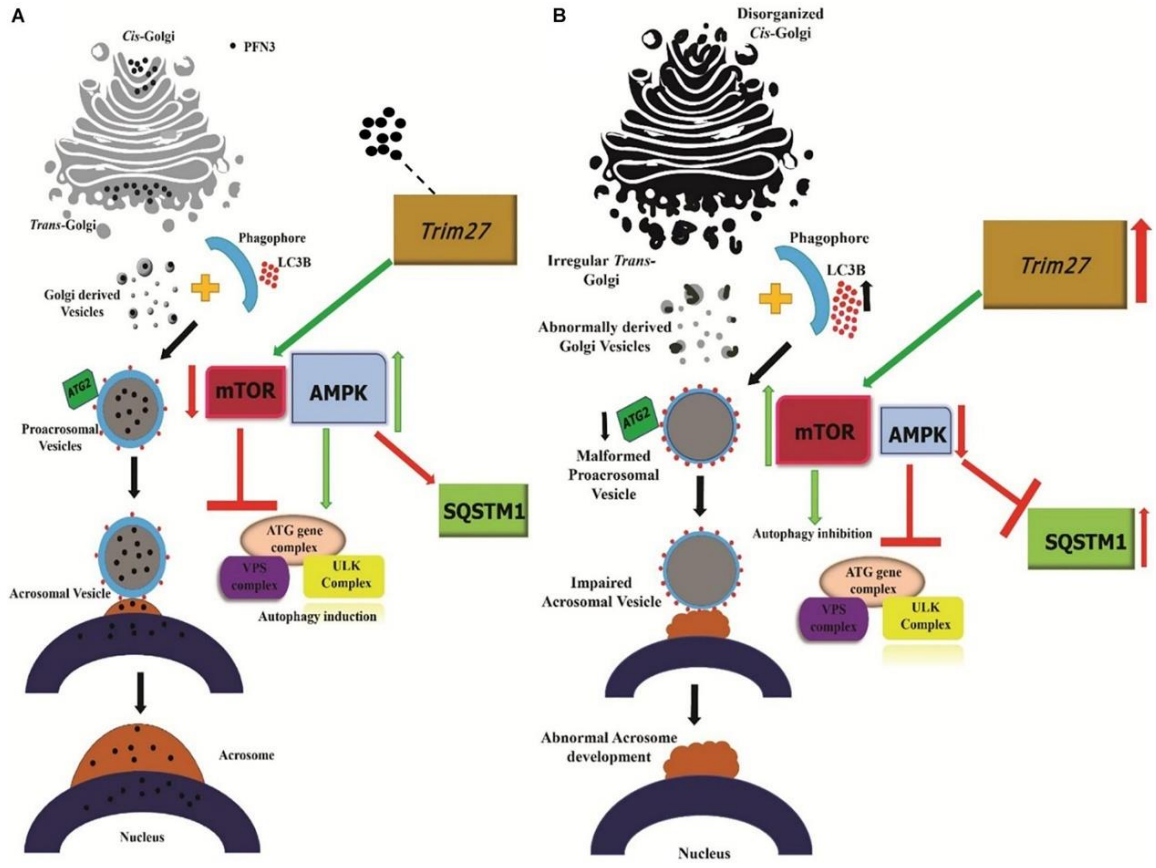

Figure 24: Working hypothesis on the PFN3 role in acrosome biogenesis. **(A)** Schematic illustration of the *Pfn3* presence in Golgi network responsible for proacrosomal formation associated with the autophagy mechanism. **(B)** Schematic illustration depicting the disrupted autophagy mechanism and acrosome formation in the absence of *Pfn3*. Black dots = PFN3.

Part of this chapter have been published in :

Umer, N., Arévalo, L., Phadke, S., Lohanadan, K., Kirfel, G., Sons, D., Sofia, D., *et al.* (2021a), "**Loss of Profilin3 Impairs Spermiogenesis by Affecting Acrosome Biogenesis, Autophagy, Manchette Development and Mitochondrial Organization**", *Frontiers in Cell and Developmental Biology*, Vol. 9, available at: https://doi.org/10.3389/fcell.2021.749559.

6. RESULT II

Profilin 4 (*Pfn4*, PFN4) is highly expressed in testes and localized to the acrosome-acroplaxome-manchette complex (Behnen et al., 2009). *Pfn4* shows only 30% homology to other profilin family members, it does not encode for the actin binding and poly-L-proline binding sites as found in *Pfn1, 2* and *3* (Behnen et al., 2009).

6.1 Generation and phenotypic characterization of PFN4-deficient mouse lines

To delete the *Pfn4* alleles CRISPR/Cas9 was used, and two sgRNAs (annealing to Exon2 and Exon4 of the *Pfn4* locus) (Figure 25 A) and Cas9 mRNA were injected into the cytoplasm of fertilized oocytes. Successful gene editing was detected by PCR and confirmed by sequencing (Figure 25 B, C). Two PFN4 deficient mouse lines harboring identical deletions of 5417bp were established and backcrossed to C57BL/6 mice and named *Pfn4*Δa and *Pfn4*Δb. The deletion resulted in a frame shift in the PFN4 reading frame, leading to premature translational termination giving rise to a hypothetical truncated protein of 25 amino acids.

For *Pfn4*Δa and *Pfn4*Δb, real time quantitative PCR (qRT-PCR) showed that expression of *Pfn4* mRNA is reduced by half in $Pfn4^{+/-}$ compared to WT mice. No *Pfn4* transcript was detected in *Pfn4*Δa (Figure 25 D) and *Pfn4*Δb (Figure 25 E). Mice confirming that the *Pfn4*Δ allele is in fact a functional null allele.

After generating and validating the PFN4-deficient lines, we performed fertility analysis on male mice of both lines (*Pfn4*Δa, and *Pfn4*Δb). Adult $Pfn4^{+/-}$ and $Pfn4^{-/-}$ males mated normally with females as vaginal plugs were clearly seen. $Pfn4^{+/-}$ mice retain normal fertility, with average litter size comparable to WT littermates. This suggests that the reduced level of *Pfn4* mRNA observed in heterozygous males does not affect regular fertility. In contrast, $Pfn4^{-/-}$ mice are infertile as none of the males (n=9) produced any pregnancy or offspring (Figure 25 F). Of note, female $Pfn4^{-/-}$ mice did not show any alterations in fertility (Figure 25 G).

For both PFN4-deficient lines (*Pfn4*Δa, *Pfn4*Δb), body weight (Figure 25 H), absolute and relative weight of testes and epididymis in $Pfn4^{-/-}$ males were comparable with $Pfn4^{+/-}$ and WT littermates (Figure 25 I-L).

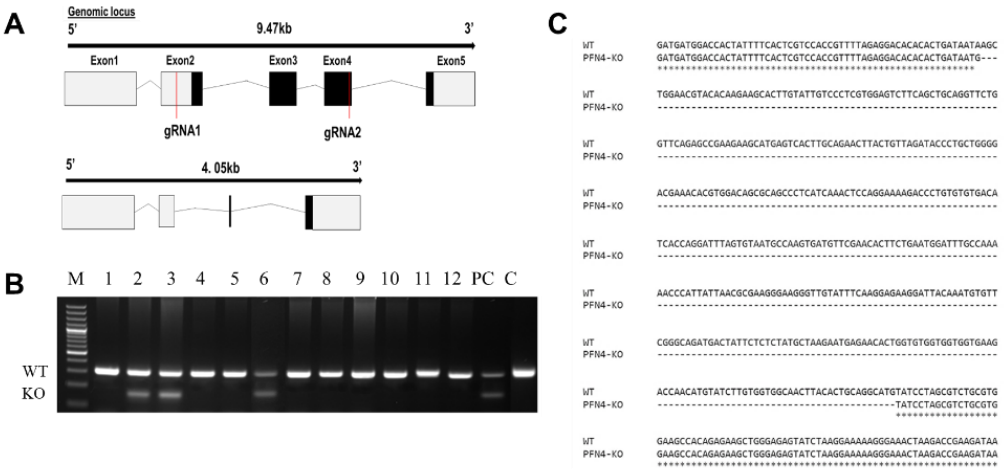
A
Genomic locus
5'
9.47kb
3'
Exon1
Exon2
Exon3
Exon4
Exon5
gRNA1
gRNA2
5'
4. 05kb
3'
B
M 1 2 3 4 5 6 7 8 9 10 11 12 PC C
WT
KO
C
WT GATGATGGACCACTATTTTCACTCGTCCACCGTTTTAGAGGACACACACTGATAATAAGC
PFN4-KO GATGATGGACCACTATTTTCACTCGTCCACCGTTTTAGAGGACACACACTGATAATG---
WT TGGAACGTACACAAGAAGCACTTGTATTGTCCCTCGTGGAGTCTTCAGCTGCAGGTTCTG
PFN4-KO
WT GTTCAGAGCCGAAGAAGCATGAGTCACTTGCAGAACTTACTGTTAGATACCCTGCTGGGG
PFN4-KO
WT ACGAAACACGTGGACAGCGCAGCCCTCATCAAACTCCAGGAAAAGACCCTGTGTGTGACA
PFN4-KO
WT TCACCAGGATTTAGTGTAATGCCAAGTGATGTTCGAACACTTCTGAATGGATTTGCCAAA
PFN4-KO
WT AACCCATTATTAACGCGAAGGGAAGGGTTGTATTTCAAGGAGAAGGATTACAAATGTGTT
PFN4-KO
WT CGGGCAGATGACTATTCTCTCTATGCTAAGAATGAGAACACTGGTGTGGTGGTGGTGAAG
PFN4-KO
WT ACCAACATGTATCTTGTGGTGGCAACTTACACTGCAGGCATGTATCCTAGCGTCTGCGTG
PFN4-KO TATCCTAGCGTCTGCGTG
WT GAAGCCACAGAGAAGCTGGGAGAGTATCTAAGGAAAAAGGGAAACTAAGACCGAAGATAA
PFN4-KO GAAGCCACAGAGAAGCTGGGAGAGTATCTAAGGAAAAAGGGAAACTAAGACCGAAGATAA

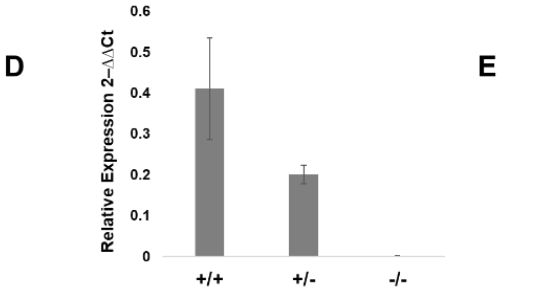
D
Relative Expression 2−ΔΔCt
0.6
0.5
0.4
0.3
0.2
0.1
0
+/+
+/-
-/-

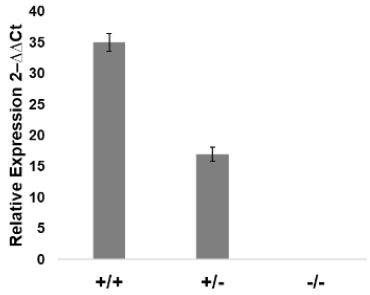
E
Relative Expression 2−ΔΔCt
40
35
30
25
20
15
10
5
0
+/+
+/-
-/-

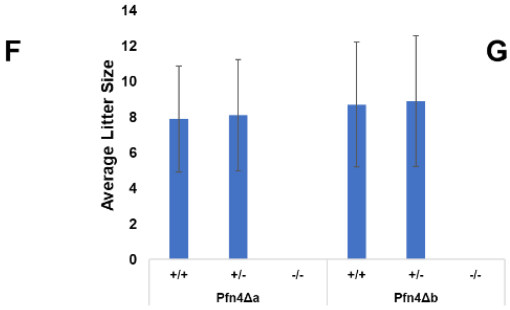
F
Average Litter Size
14
12
10
8
6
4
2
0
+/+ +/- -/- +/+ +/- -/-
Pfn4Δa
Pfn4Δb

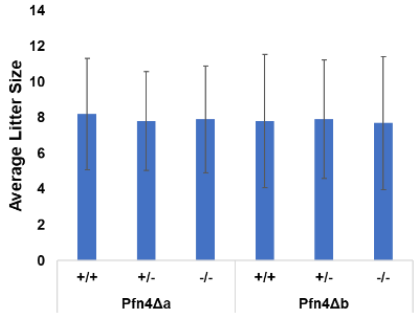
G
Average Litter Size
14
12
10
8
6
4
2
0
+/+ +/- -/- +/+ +/- -/-
Pfn4Δa
Pfn4Δb

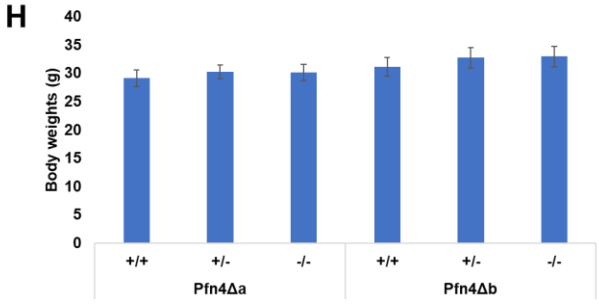
H
Body weights (g)
40
35
30
25
20
15
10
5
0
+/+ +/- -/- +/+ +/- -/-
Pfn4Δa
Pfn4Δb

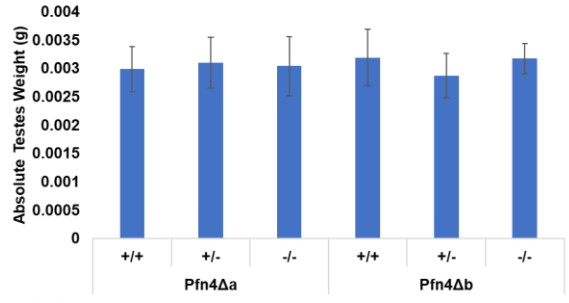
I
Absolute Testes Weight (g)
0.004
0.0035
0.003
0.0025
0.002
0.0015
0.001
0.0005
0
+/+ +/- -/- +/+ +/- -/-
Pfn4Δa
Pfn4Δb

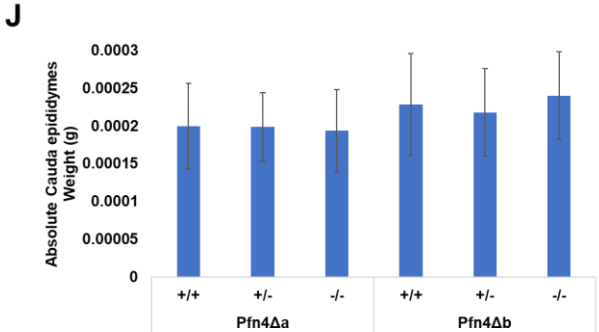
J
Absolute Cauda epididymes Weight (g)
0.0003
0.00025
0.0002
0.00015
0.0001
0.00005
0
+/+ +/- -/- +/+ +/- -/-
Pfn4Δa
Pfn4Δb

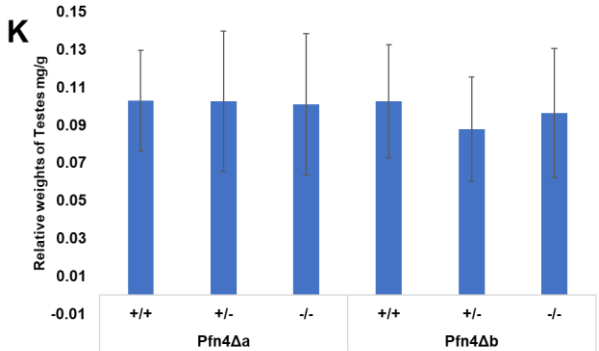
K
Relative weights of Testes mg/g
0.15
0.13
0.11
0.09
0.07
0.05
0.03
0.01
-0.01
+/+ +/- -/- +/+ +/- -/-
Pfn4Δa
Pfn4Δb

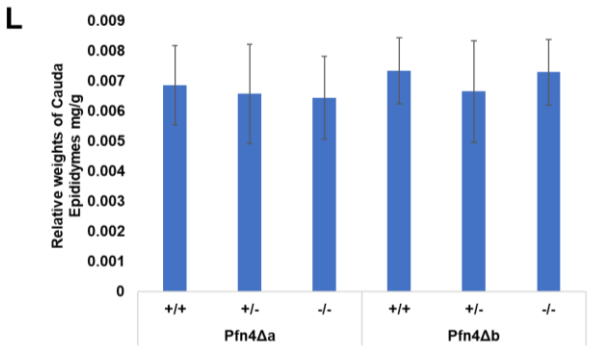

Figure 25: Generation and characterization of PFN4-deficient mice. **(A)** Genotyping for PFN4-deficient founder mice (P#2, 3, and 6 are positive for the deletion). M= 100bp Plus ladder, 302 bp PCR product represents WT allele, and 180bp PCR products represent mutant allele. **(B)** Sequencing results using clustalW of Pfn4Δ5417 mouse line. Sequences of WT and PFN4-deficient line. * indicates same base pairs and Dash line (-) represents deletion. **(C)** Schematic of the *Pfn4* locus and established PFN4-deficient mouse line. **(D, E)** Validation of PFN4-deficient mice (*Pfn4*ΔAa, *Pfn4*Δb). qRT-PCR showed the expression of *Pfn4* mRNA in murine testis of WT, $Pfn4^{+/-}$ and $Pfn4^{-/-}$ mice for *Pfn4*Δ5417a and *Pfn4*Δ5417b mutation. **(F)** Average litter size of WT, $Pfn4^{+/-}$ and $Pfn4^{-/-}$ male for *Pfn4*Δ5417a and *Pfn4*Δ5417b mutation. **(G)** Average litter size of WT, $Pfn4^{+/-}$ and $Pfn4^{-/-}$ female for *Pfn4*Δa and *Pfn4*Δb lines. **(H)** Body weights in gram, **(I, J)** Absolute weight of testes and cauda epididymis, **(K, L)** Relative weight of testes and cauda epididymis of WT, $Pfn4^{+/-}$ and $Pfn4^{-/-}$ for *Pfn4*Δa and *Pfn4*Δb lines (n=9).

Next, Periodic acid Schiff (PAS) staining and hematoxylin and eosin (H&E) staining was performed on testes and cauda epididymis sections respectively. Histological examination showed that the overall morphology of the seminiferous tubules and cauda epididymis is not affected, and spermatogenesis seems normal in *Pfn4*$^{+/-}$ and *Pfn4*$^{-/-}$ mice compared to WT for *Pfn4*Δa (Figure 26 A, B). However, we observed mis-shaped and seemingly smaller nuclei in elongating spermatozoa (black arrows, Figure 26 C). These results showed that loss of *Pfn4* did not affect the gross morphology of testes and epididymis, but the smaller head shape of elongated spermatozoa was observed.

In addition, sperm count is significantly reduced in *Pfn4*$^{+/-}$ and *Pfn4*$^{-/-}$ males for each line (Figure 26 D). In order to assess the viability of spermatozoa, eosin and nigrosin (E&N) staining was performed on mature sperm cells isolated from cauda epididymis. E&N differentiate live (white heads) from dead sperm (pink heads) (Figure 26 E). In mice a percentage of 60-80% live sperm is considered normal, 40-60% borderline and less than 40% abnormal. E&N staining showed that *Pfn4*$^{+/-}$ male mice display normal percentage of viable sperm while in *Pfn4*$^{-/-}$ mice an abnormally low percentage of viable sperm (~25%) is observed (Figure 26 F). To confirm this, a hypo-osmotic swelling test was performed on caudal sperm, where intact (live) sperm show tail curling (Figure 26 G). The percentage of hypo-osmotic reactive sperm in *Pfn4*$^{-/-}$ mice was abnormally low (~24%) (Figure 26 H). *Pfn4*Δb mice showed a similar phenotype to *Pfn4*Δa. In conclusion, loss of *Pfn4* affects sperm count and viability. As noted, before, we observed that sperm from *Pfn4*$^{-/-}$ displays an amorphous and smaller head shape (black arrows) (Figure 26 E).

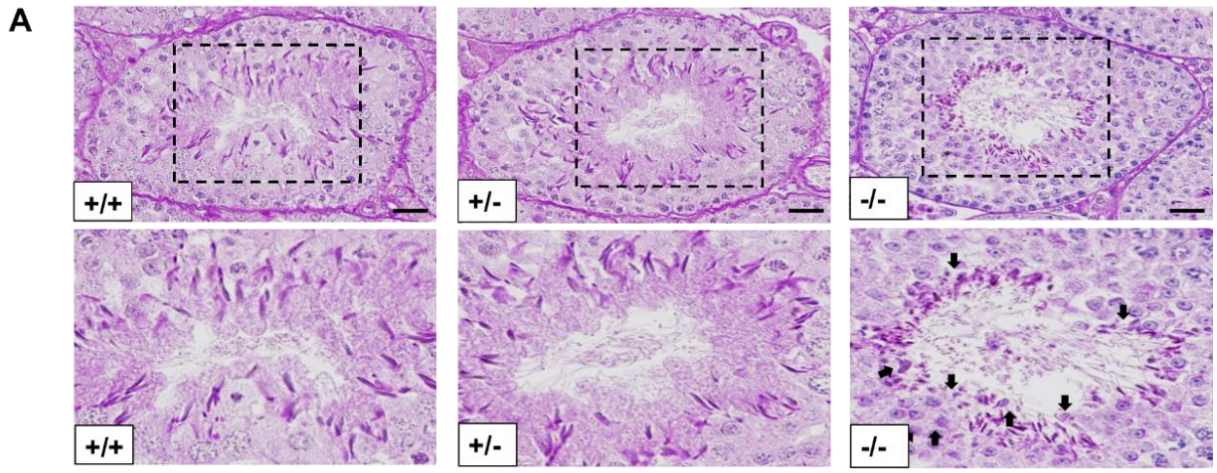

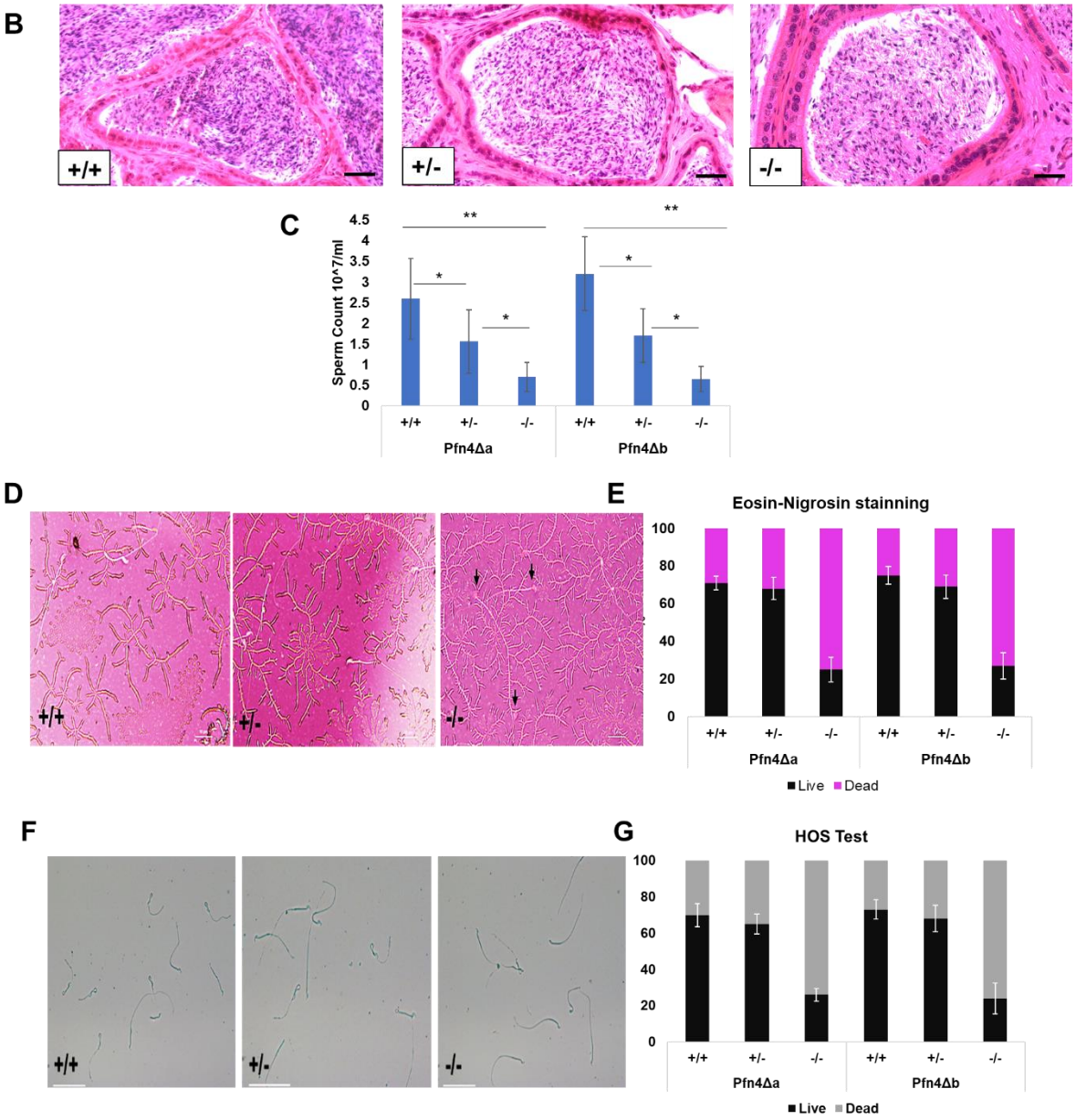

Figure 26: Histological analysis on PFN4-deficient mice. **(A)** PAS staining on WT, *Pfn4*$^{+/-}$ and *Pfn4*$^{-/-}$ testes sections. Scale bar = 10µm. **(B)** H&E staining on WT, *Pfn4*$^{+/-}$ and *Pfn4*$^{-/-}$ cauda epididymis sections. Scale bar = 10µm. **(C)** Sperm count of WT, *Pfn4*$^{+/-}$ and *Pfn4*$^{-/-}$ male for *Pfn4*Δa and *Pfn4*Δb line. **(D)** Eosin and nigrosine staining of mature WT, *Pfn4*$^{+/-}$ and *Pfn4*$^{-/-}$ sperms isolated from cauda epididymis. Live= white sperm cells, pink=dead sperm cells. Scale bar = 10 µm. **(E)** Eosin and nigrosine staining on biological replicates (n=3) per genotype of WT, *Pfn4*$^{+/-}$ and *Pfn4*$^{-/-}$ sperms for *Pfn4*Δa and *Pfn4*Δb line. **(F)** Hypo-osmotic swelling test performed of mature WT, *Pfn4*$^{+/-}$ and *Pfn4*$^{-/-}$ sperms isolated from cauda epididymis. Tail curling= live sperm cells. Scale bar= 10µm. **(G)** Hypo-osmotic swelling test on biological replicates (n=3) per genotype of WT, *Pfn4*$^{+/-}$ and *Pfn4*$^{-/-}$ sperm for *Pfn4*Δa and *Pfn4*Δb line. Scale bar = 10µm. At least 200 spermatozoa were evaluated per sample.

6.2 Loss of PFN4 results in aberrant sperm nuclear morphology

In order to determine the shape of the sperm head, we next isolated mature sperm from cauda epididymis, and performed nuclear morphology analysis (Figure 27 A). Interestingly, 77% of *Pfn4*$^{-/-}$ sperm head showed irregular/round and smaller head size (Cluster 2) compared to WT and *Pfn4*$^{+/-}$ sperm. However, only 16% (Cluster 1) of *Pfn4*$^{-/-}$ sperm head are comparable to WT and *Pfn4*$^{+/-}$ (Figure 27 B). Nuclear area, perimeter, regularity, bounding width and circularity were significantly affected in *Pfn4*$^{-/-}$ sperm compared to WT and *Pfn4*$^{+/-}$ sperm (Figure 27 C). This result indicates that PFN4 plays a role in sperm head shaping.

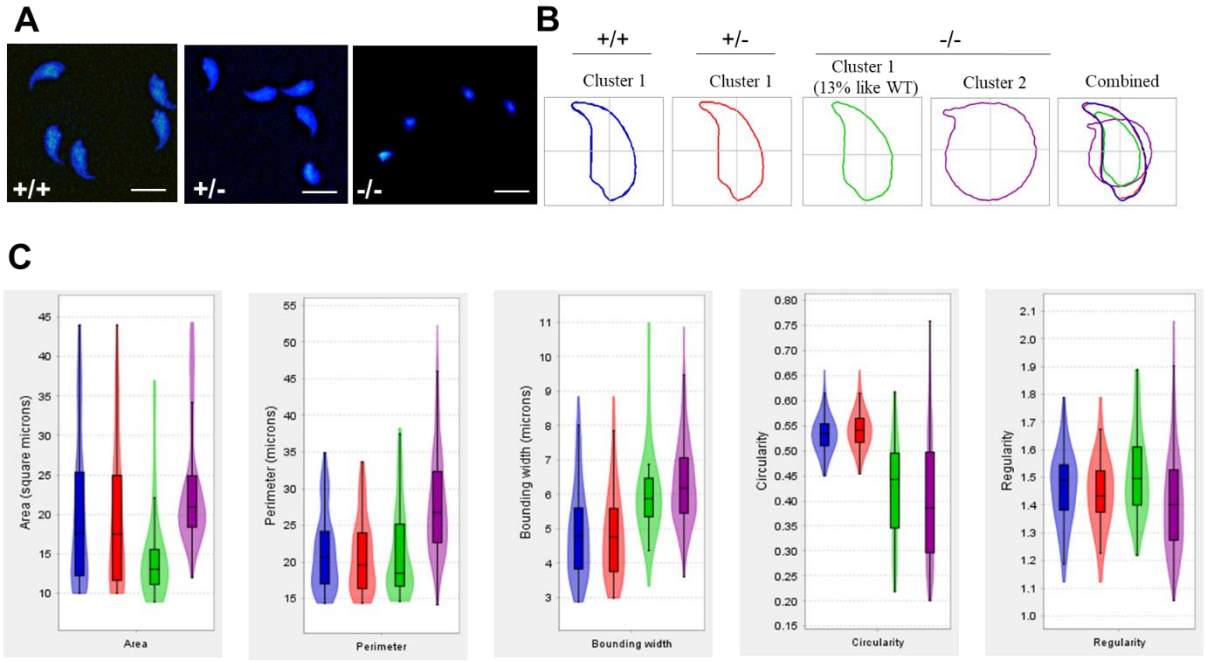

Figure 27: Nuclear morphology analysis on WT, *Pfn4*$^{+/-}$ and *Pfn4*$^{-/-}$ sperm cells. In total, 901 nuclei were analyzed: 309 for WT (cluster 1), 276 for *Pfn4*$^{+/-}$ (Cluster 1) and 541 for *Pfn4*$^{-/-}$ (86 sperm nuclei in Cluster 1 and 455 nuclei in Cluster 2). **(A)** Sperm cells stained with DAPI. **(B)** Head morphology of WT, *Pfn4*$^{+/-}$ and *Pfn4*$^{-/-}$ sperm cells. **(C)** area, perimeter, regularity, bounding width and circularity of WT, *Pfn4*$^{+/-}$ and *Pfn4*$^{-/-}$ sperm cells.

6.3 Defective manchette development in *Pfn4*$^{-/-}$ mice

The manchette is a temporary microtubular structure, which surrounds the sperm nucleus during spermatid elongation, and is discussed to play a role in shaping of the sperm head (Kierszenbaum and Tres, 2004). Since PFN4 is localized to the manchette (Behnen et al., 2009) we addressed the question, whether the loss of PFN4 affects manchette formation. Alpha tubulin staining demonstrated, that *Pfn4*$^{+/-}$ and WT spermatids showed proper manchette

development and structural organization as a tight junction of manchette microtubular array of the caudal region of spermatids (Figure 28 A, B). In contrast, in *Pfn4*$^{-/-}$ mice, manchette development was not evident from step 8 to step 13, as the posterior region of developing spermatids lack the typical parallel microtubular array structure of the manchette. As a consequence, the shape of sperm head appears smaller and deformed (Figure 27 B). This result further confirms the smaller and vastly deformed sperm head as seen in (Figure 29 B). Manchette defects were further confirmed at ultrastructure level using TEM (Figure 28 D). IHC using alpha tubulin antibody further confirms the manchette defects in in *Pfn4*$^{-/-}$ mice (Figure 28 E). This suggests that deletion of PFN4 disrupts manchette formation. Due to the involvement of the manchette in shaping the sperm head, we hypothesize, that this defect contributes to the abnormal shape of *Pfn4*$^{-/-}$ sperm heads.

In addition, we performed IHC (Immunohistochemical staining) using HOOK1 (Hook Microtubule Tethering Protein 1) and ARL3 (ADP-ribosylation factor like 3) antibodies on testes sections for all three genotype to see whether the localization of these proteins is affected in *Pfn4*$^{-/-}$ testes. HOOK1 protein belongs to the family of HOOK cytoplasmic proteins and plays a role in correct positioning and elongation of microtubular manchette (Schwarz et al., 2017). ARL3 is a novel protein localized in manchette and essential for its development (Qi et al., 2013). Our IHC staining revealed that ARL3 (Figure 28 F) and HOOK1 (Figure 28 G) showed disturbed manchette microtubular structure of *Pfn4*$^{-/-}$ spermatids, while in WT and *Pfn4*$^{+/-}$ testes sections, microtubular manchette is properly aligned as a from step 8-13. These results further confirmed the manchette abnormality in *Pfn4*$^{-/-}$ mice.

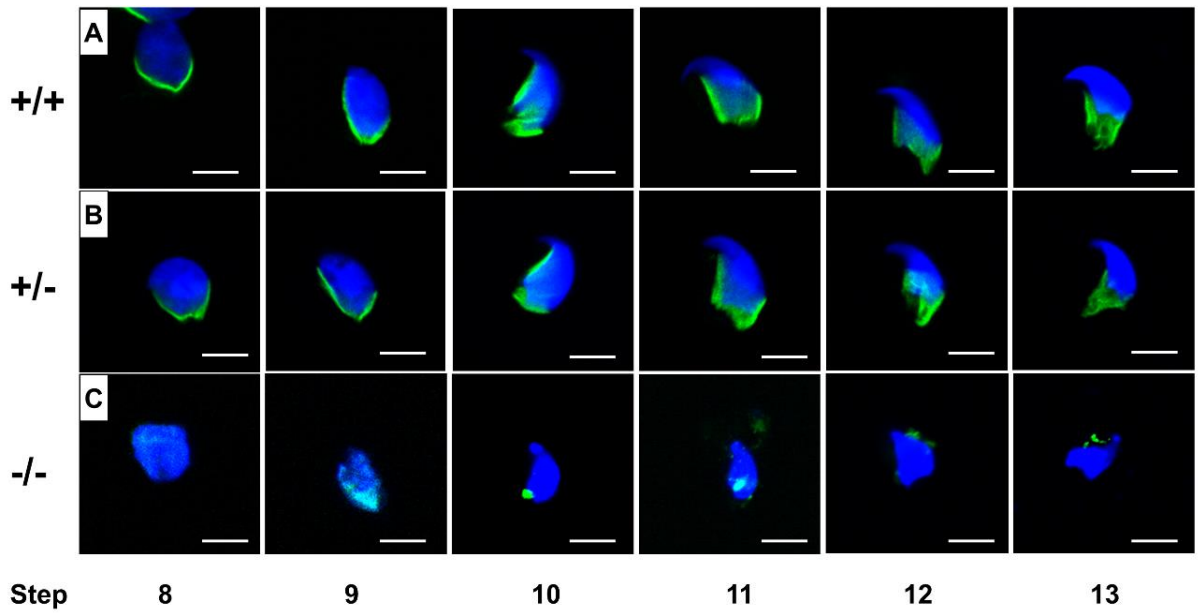

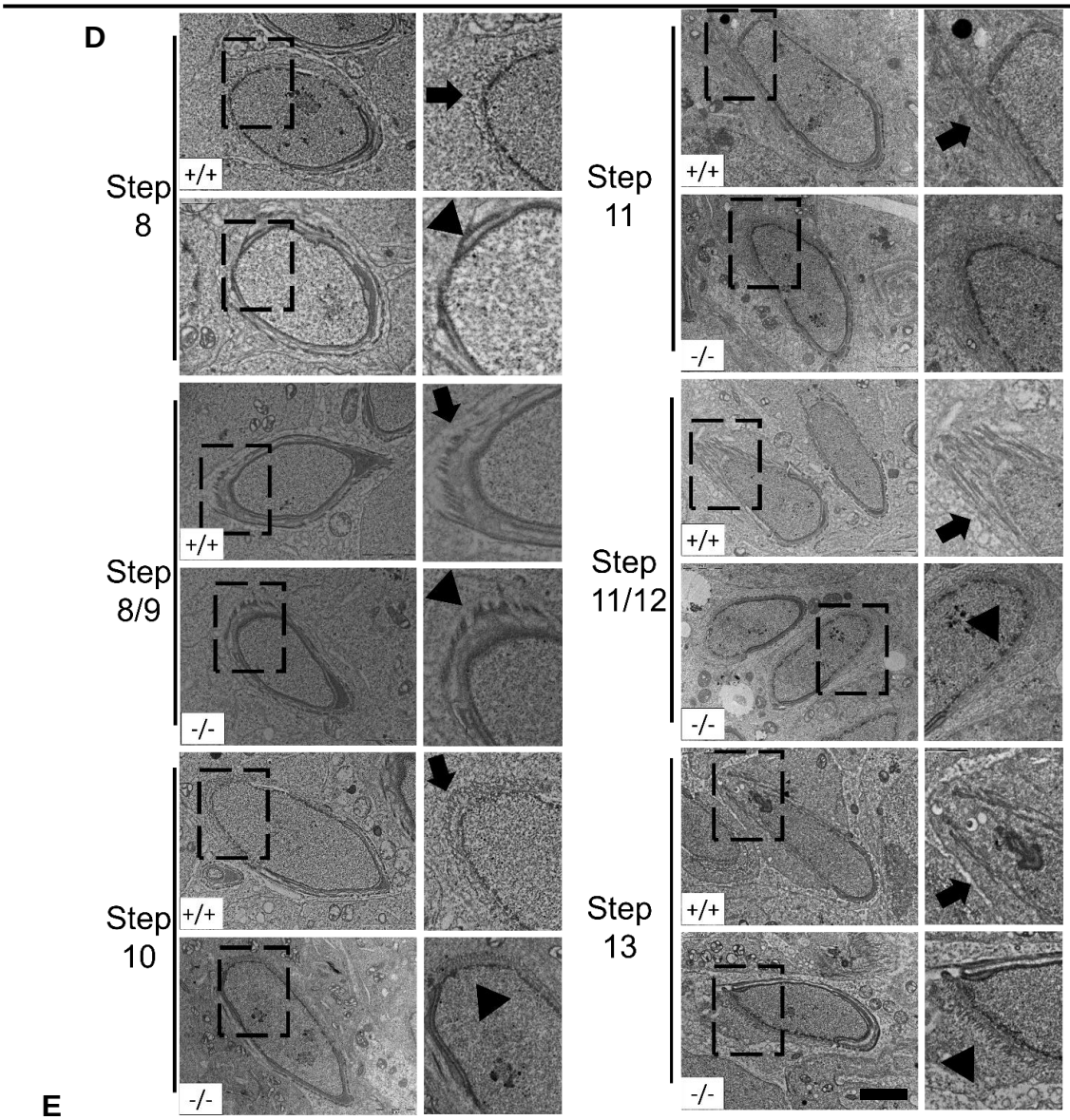
D
Step 8
Step 8/9
Step 10
Step 11
Step 11/12
Step 13
+/+
-/-

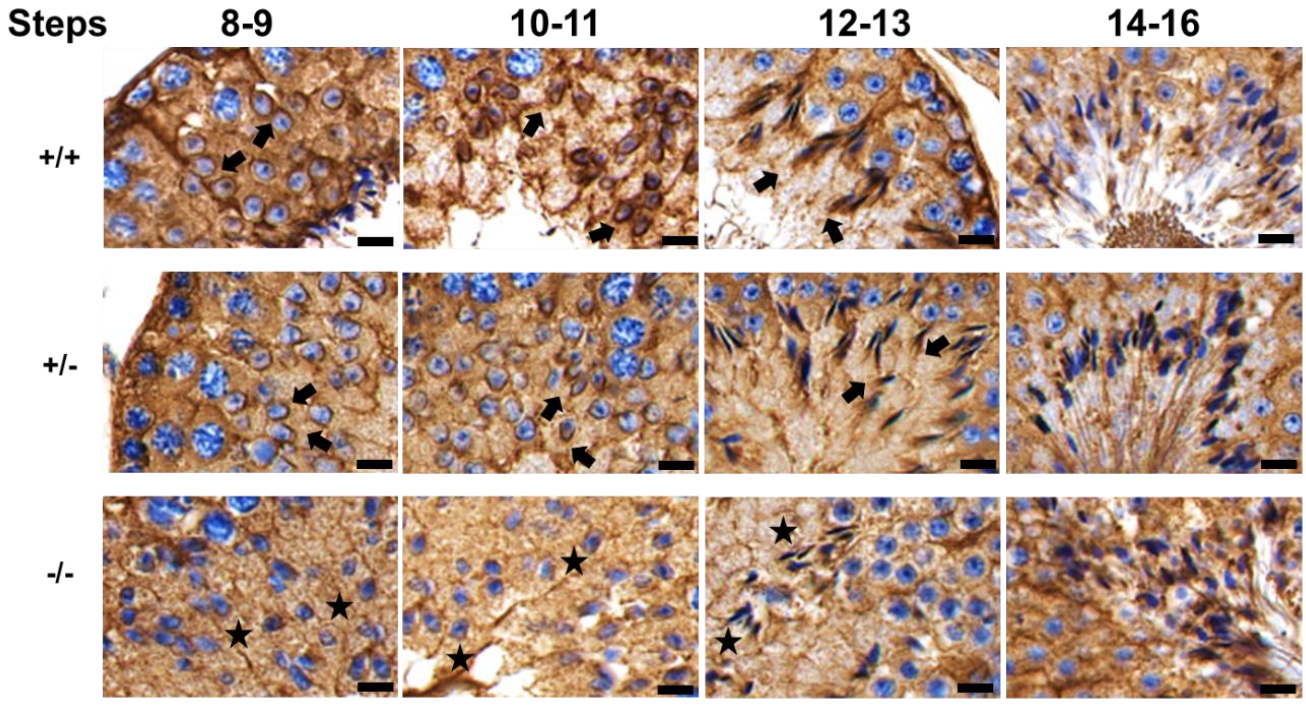
E
Steps
8-9
10-11
12-13
14-16
+/+
+/-
-/-

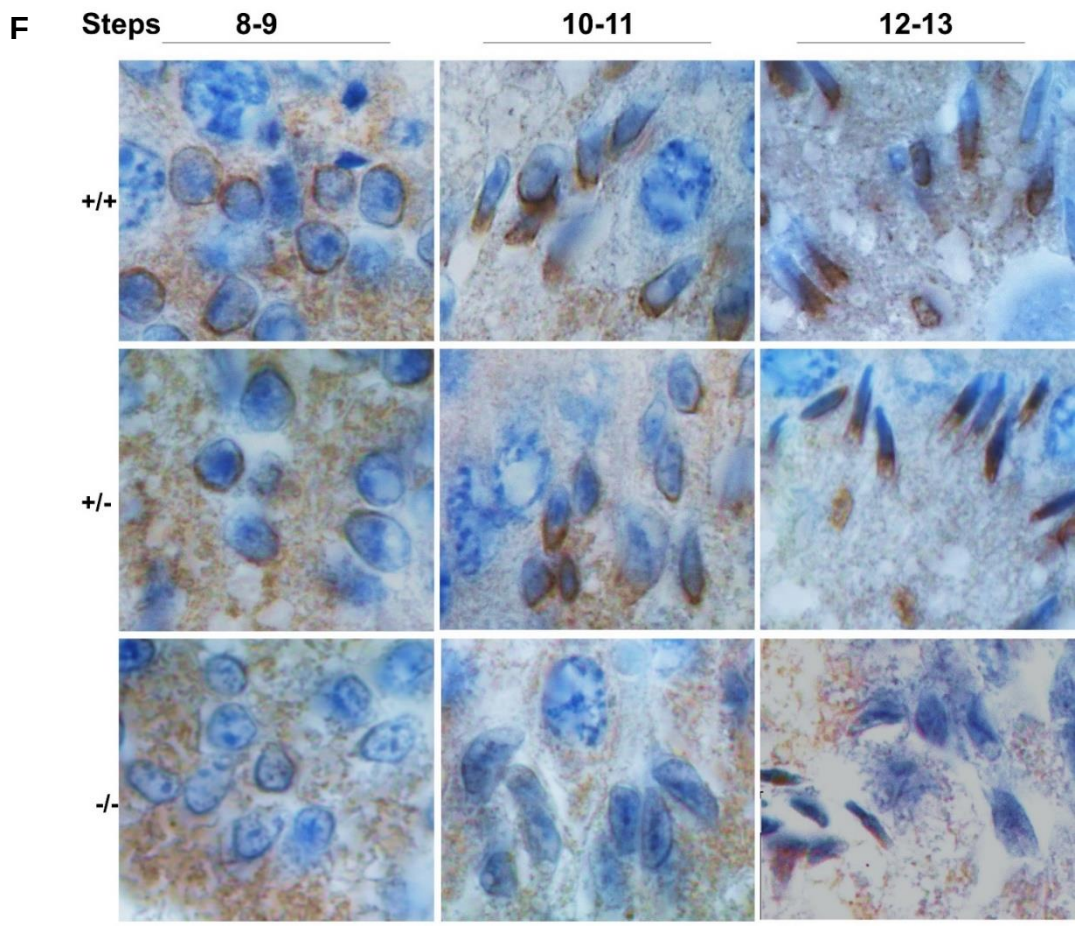
F
Steps
8-9
10-11
12-13
+/+
+/-
-/-

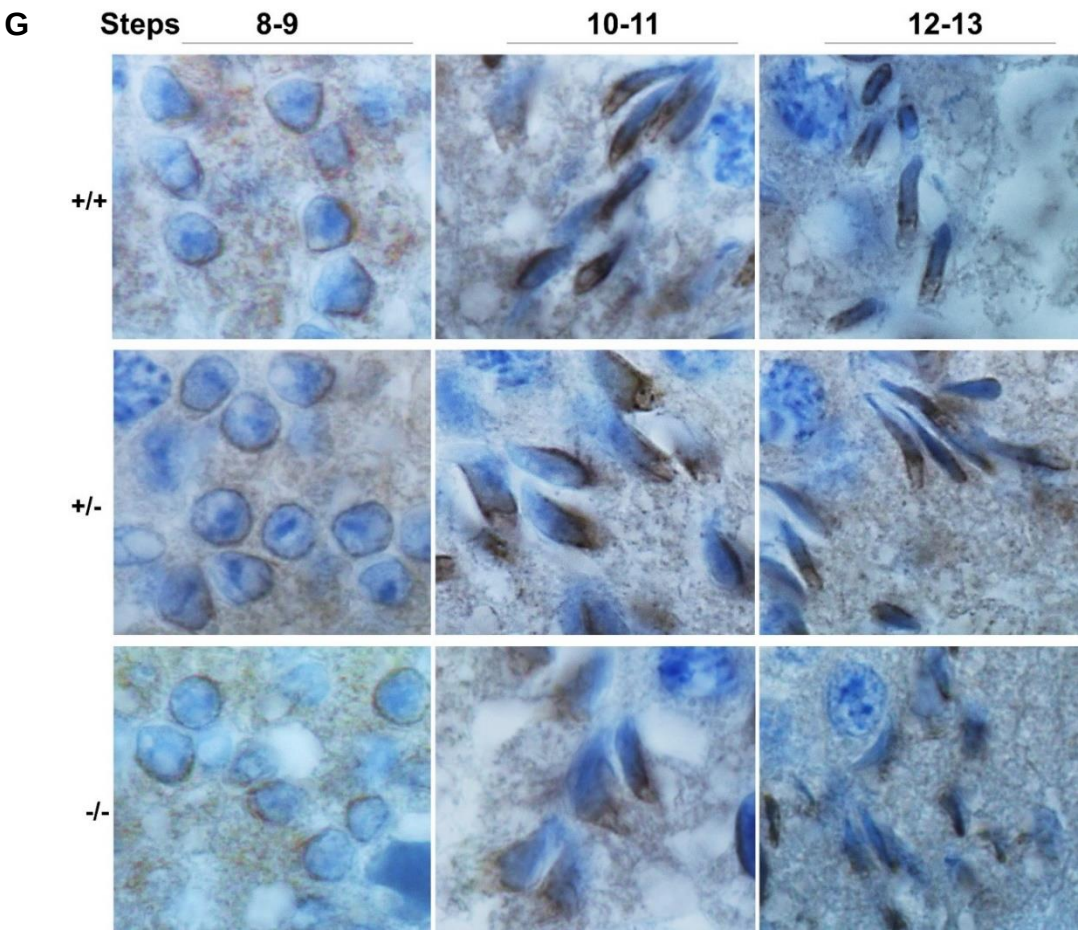
G
Steps
8-9
10-11
12-13
+/+
+/-
-/-

Figure 28: Immunofluorescence staining for manchette using α-tubulin antibody (green) on germ cell population isolated from **(A)** WT, **(B)** *Pfn4*$^{+/-}$ and **(C)** *Pfn4*$^{-/-}$ testes (n= 3/genotype). Nuclei were stained with DAPI (blue). Scale bar = 20µm. **(D)** Ultrastructure of manchette formation in developing spermatids from step8-13 using TEM in WT and *Pfn4*$^{-/-}$ mice. Black arrows indicating manchette formation in WT and arrow heads indicating malformed manchette. Scale bar= 2µm. **(E)** alpha tubulin staining on WT, *Pfn4*$^{+/-}$ and *Pfn4*$^{-/-}$ testes sections. Scale bar= 20µm. **(F)** IHC using anti-ARL3 antibody on WT, *Pfn4*$^{+/-}$ and *Pfn4*$^{-/-}$ testes sections. **(G)** IHC using anti-HOOK1 antibody on WT, *Pfn4*$^{+/-}$ and *Pfn4*$^{-/-}$ testes sections. Scale bar= 20µm.

6.4 Flagellar defects in *Pfn4*$^{-/-}$ sperm

Since loss of *Pfn4* disturbs the development of the manchette. We next examined the flagellar structure in order to see whether malformed manchette results in flagellar deformities in the absence of PFN4. It has been reported previously by Mochida and Mendoza, that sperm tail proteins during flagellar development are delivered through the manchette as well, aside from the intraflagellar transport (IFT) (Mochida, Tres and Kierszenbaum, 1991), (Mendoza-Lujambio et al., 2002) Therefore, to determine whether there are defects in organization of flagellar structures, MitoRed, SEM and TEM was performed on sperm cells isolated from cauda epididymis. In order to check the mitochondria structural organization, MitoRed dye was used to stain the sperm mitochondria in mid piece of flagella and DAPI was used to stain sperm head. The mitochondrial sheath stained precisely in WT (Figure 29 A) and *Pfn4*$^{+/-}$ sperm flagella (Figure 29 A). However, *Pfn4*$^{-/-}$ sperm flagella revealed numerous deformities including i) cytoplasmic droplets in connecting piece, ii) bent mid piece with abnormal sperm head morphology, and abnormally thick mid piece (Figure 29 A). This suggests, that the disturbed manchette seen in *Pfn4*$^{-/-}$ males, causes the mitochondria abnormalities in sperm flagellum.

MitoRed showed abnormal staining of sperm flagella so, in order to see the mitochondria ultrastructural defects in flagella of *Pfn4*$^{-/-}$ sperm, TEM was performed on cauda epididymis sperm. TEM on *Pfn4*$^{-/-}$ sperm revealed disorganized flagellar components. These defects are i) cytoplasmic droplets in mid piece, ii) mitochondria structural defects, and iii) defective fibrous sheath, compared to WT and *Pfn4*$^{+/-}$ sperm ultrastructure (Figure 29 B). Scanning electron microscope (SEM) revealed morphological anomalies of *Pfn4*$^{-/-}$ sperm including, i) coiled flagella, ii) shortened thick mid piece, iii) cytoplasmic droplets in mid piece and iv) bent

connecting piece (Figure 29 C), however *Pfn4*$^{+/+}$ and *Pfn4*$^{+/-}$ sperm showed nicely fined flagella (Figure 29 C).

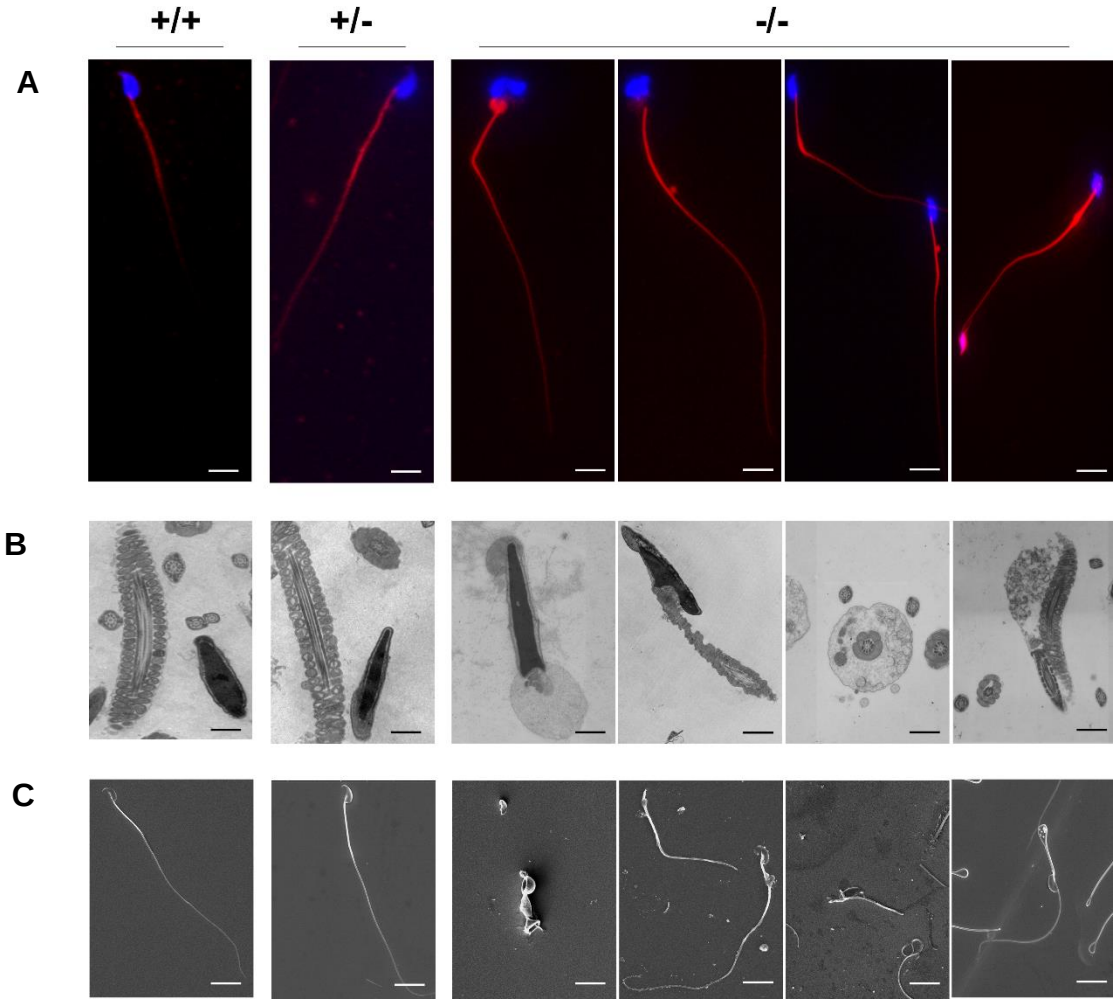

Figure 29: Flagellar staining and ultrastructural analysis using MitoRed, TEM, and SEM on WT, *Pfn4*$^{+/-}$ and *Pfn4*$^{-/-}$ sperm. (A) MitoRed staining, (B) TEM, and (C) SEM on WT, *Pfn4*$^{+/-}$ and *Pfn4*$^{-/-}$ sperm isolated from cauda epididymis. Scale bar = 10µm.

6.5 Reduced sperm motility in *Pfn4*$^{-/-}$ mice

Flagellar deformities might affect the sperm motility parameters, so, we performed computer assisted semen analysis (CASA), to analyze the swimming properties of *Pfn4*$^{-/-}$ sperm. Compared to *Pfn4*$^{+/+}$ and *Pfn4*$^{+/-}$, sperm motility parameters (curvilinear velocity (VCL), straight-line velocity (VSL), average path velocity (VAP) progressive and total motility) are significantly reduced in *Pfn4*$^{-/-}$ sperm (Table 1). These results indicated that abnormalities in sperm flagella led to the reduced overall sperm motility in *Pfn4*$^{-/-}$ mice.

	VSL Mean (µm/s)	VCL Mean (µm/s)	VAP Mean (µm/s)	Progressive Motility (%)	Motility (%)
***Pfn4*$^{+/+}$**	180.45±1.5	309.2±4.8	144.7±5.9	64.61±1.3	61.3±2.1
***Pfn4*$^{+/-}$**	176.54±1.7	265.8±6.6	129.2±4.2	62.56±2.13	57.28±1.98
***Pfn4*$^{-/-}$**	19.530±1.1	99.2892±4.9	59.9289±6.2	3.281833±3.65**	28.633±2.9*

Table 22: Motility parameters. Motility parameters were analyzed for *Pfn4*$^{+/+}$, *Pfn4*$^{+/-}$, and *Pfn4*$^{-/-}$ sperms using OpenCASA software. (n=3/genotype). Data is presented as mean ±SD using ANOVA: Tukey's post-hoc test. VSL: straight-line velocity (µm/s); VCL: curvilinear velocity (µm/s); VAP: average path velocity (µm/s).

6.6 PFN4 is essential for acrosome biogenesis

In addition to the manchette, PFN4 is also localized to the acroplaxome (Behnen et al., 2009) suggesting a role in biogenesis/function of the acrosome. In order to examine acrosome development, PNA-FITC fluorescence labelling was performed on testes sections to visualize the different steps of acrosome development. In seminiferous tubules of WT (Figure 30 A) and *Pfn4*$^{+/-}$ (Figure 30 B) male mice the developing acrosome forms a single homogenous cluster present on the anterior face of nuclei in Golgi phase spermatids, while in *Pfn4*$^{-/-}$ spermatozoa PNA-FITC staining showed a non-uniform shape of the acrosomal vesicle (Figure 30 C). This abnormal acrosome development was further seen in the next step, known as the Cap phase. Here, a cap-like covering can be seen on the apical surface of the WT and *Pfn4*$^{+/-}$ spermatozoa (Figure 30 D, E). In *Pfn4*$^{-/-}$ sperm cells the cap like structures were partially impaired (white arrows) (Figure 30 F). In the acrosomal phase, where elongation and head remodeling of spermatids starts, this abnormal acrosome development was most prominent. In *Pfn4*$^{-/-}$ sperm the acrosome structure failed to develop into an arrow-like structure (Figure 30 I), as seen in the WT (Figure 30 G) and *Pfn4*$^{+/-}$ sperm (Figure 30 H). These suggest that loss of PFN4 partially impairs the biogenesis of acrosome starting from the first phase (Golgi phase) of acrosome development. Further, PNA-FITC labelling on mature sperm isolated from cauda epididymis of *Pfn4*$^{-/-}$ mice showed malformed acrosome, and in addition, aberrant head

morphology (Figure 30 J). In addition, PAS (periodic acid-Schiff) staining further confirms the abnormalities in acrosome development (Figure 30 K).

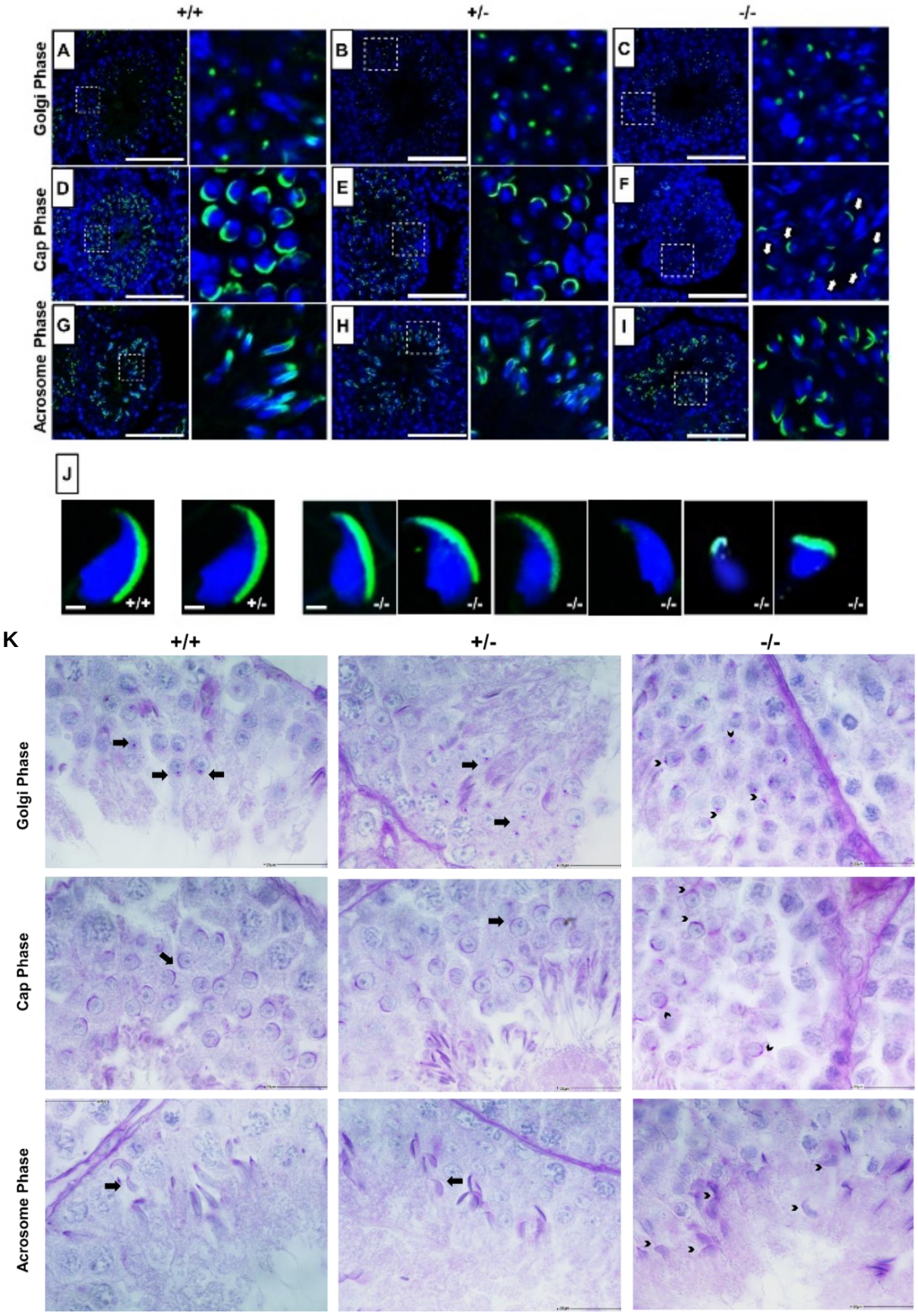

Figure 30: Immunofluorescence staining and PAS staining for acrosome biogenesis on testes sections and mature sperms of WT, *Pfn4*$^{+/-}$ and *Pfn4*$^{-/-}$ mice. In the Golgi phase, proacrosomal granule (green) labeled by PNA-FITC for **(A)** WT, **(B)** *Pfn4*$^{+/-}$ and **(C)** *Pfn4*$^{-/-}$ round spermatozoa. In the cap phase, acrosomal caps (green) stained for **(D)** WT, **(E)** *Pfn4*$^{+/-}$, and **(F)** *Pfn4*$^{-/-}$ round spermatozoa (white arrows show abnormal cap structures). In the acrosome phase, PNA-FITC-labeled acrosomal area on **(G)** WT, **(H)** *Pfn4*$^{+/-}$, and **(I)** *Pfn4*$^{-/-}$ elongated spermatids. Scale bar = 20µm. **(J)** Immunofluorescence staining using PNA-FITC (green) on epididymal sperm cells of WT, *Pfn4*$^{+/-}$ and *Pfn4*$^{-/-}$ mice (n= 3). Scale bar = 20µm. **(K)** PAS Staining on testes sections of WT, *Pfn4*$^{+/-}$ and *Pfn4*$^{-/-}$ mice. Black arrows indicating normal process of acrosome biogenesis and arrow heads indicating impaired acrosome biogenesis. Scale bar= 20µm.

Next, TEM (Transmission electron microscopy) was used for ultrastructural analysis of the developing sperm cells. In the Golgi phase, the *trans*-Golgi domain releases proacrosomal vesicles, which fuse to form a single, large, and dense acrosomal granule in the center at the marginal ring (red rectangular box) of the acroplaxome membrane (red arrow) on the nuclear surface as seen in WT (Figure 31 A) and *Pfn4*$^{+/-}$ sperm cells (Figure 31 B). Thus, in *Pfn4*$^{-/-}$ mice, the proacrosomal vesicles released from *trans*-Golgi network do not seem to gather and fuse as a single large and dense acrosomal vesicle on the apical face of developing spermatozoa. This suggests that the acrosomal vesicle formation is greatly delayed in the increase of acrosome volume for its proper development (Figure 31 C) which can be seen in subsequent stages. In the Cap phase, proacrosomal vesicle develops and flattens into the cap like structure over the nucleus in WT (Figure 31 D) and *Pfn4*$^{+/-}$ spermatids (Figure 31 E). However, in *Pfn4*$^{-/-}$ spermatids, the cap like structure did not spread out over the nucleus, but remained as a pinched granule (Figure 31 F). In the acrosomal and maturation phase this defect becomes more prominent, the cap develops further and forms a proper acrosome in WT (Figure 31 G, J) and *Pfn4*$^{+/-}$ spermatids (Figure 31 H, K), while in *Pfn4*$^{-/-}$ sperm proacrosomal vesicles fails to develop into a polarized cap and acrosome (Figure 31 I, L).

In order to investigate the acrosomal defect in mature sperm, we used TEM to analyze the mature sperm cells isolated from cauda epididymis of *Pfn4*$^{-/-}$ mice. Ultrastructural analysis showed lack of properly formed acrosomes in epididymal sperm of *Pfn4*$^{-/-}$ mice (Figure 31 M). While WT and *Pfn4*$^{+/-}$ sperm cells showed proper and intact acrosomes (Figure 31 M).

In addition, we performed IHC using Sp56 and acrosin antibodies on testes sections of WT, *Pfn4*$^{+/-}$ and *Pfn4*$^{-/-}$ mice. Sp56 and acrosin are markers of acrosomal vesicle and acrosomal matrix respectively (Xin et al., 2020). Sp56 is detectable as early (Golgi phase) as acrosome biogenesis starts (Kim et al., 2001). IHC showed that Sp56 and acrosin staining were not uniformly distributed in developing acrosome in *Pfn4*$^{-/-}$ as compared to WT and *Pfn4*$^{+/-}$ testes sections (Figure 31 N, O). These results further validate the impaired acrosome biogenesis in *Pfn4*$^{-/-}$ mice.

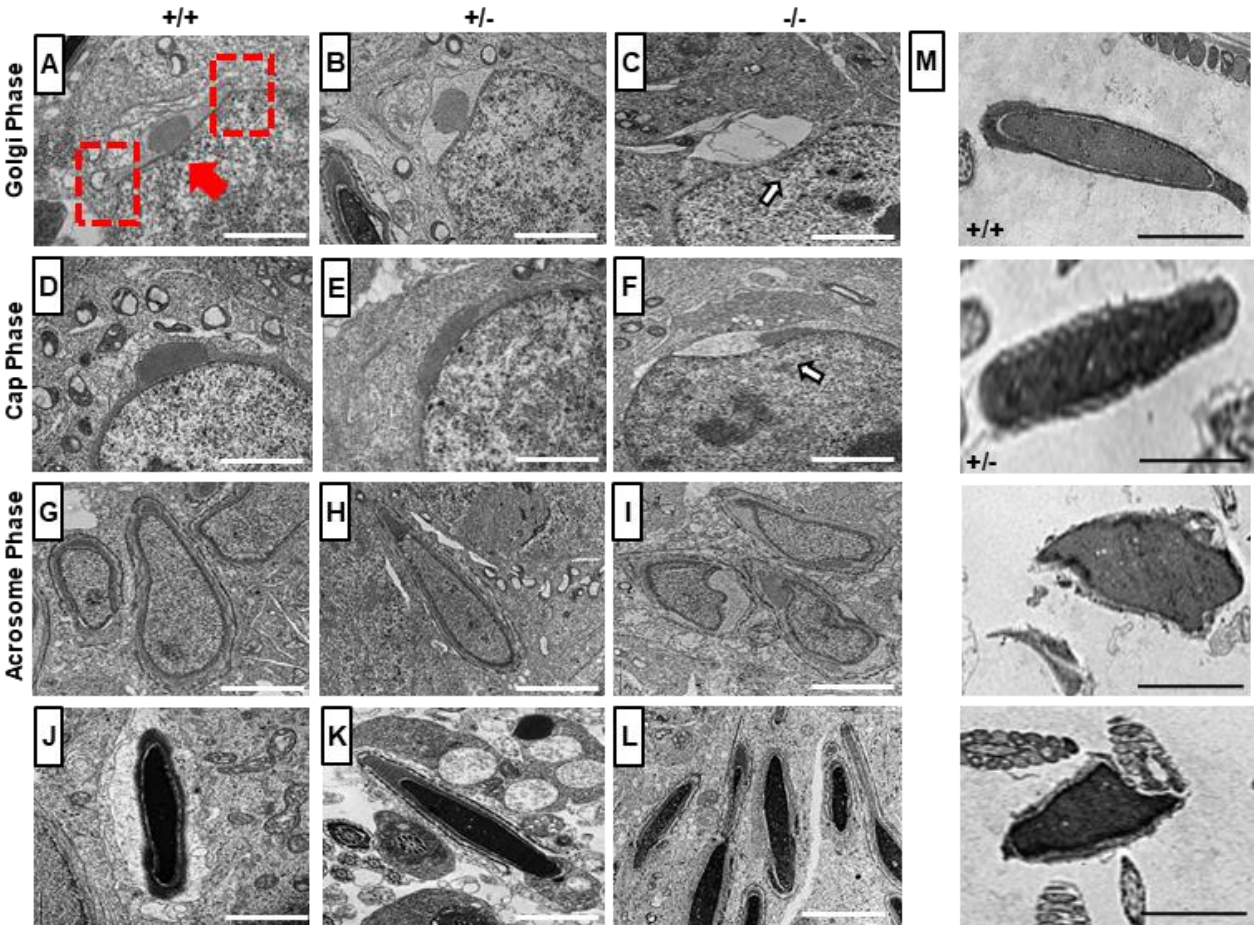

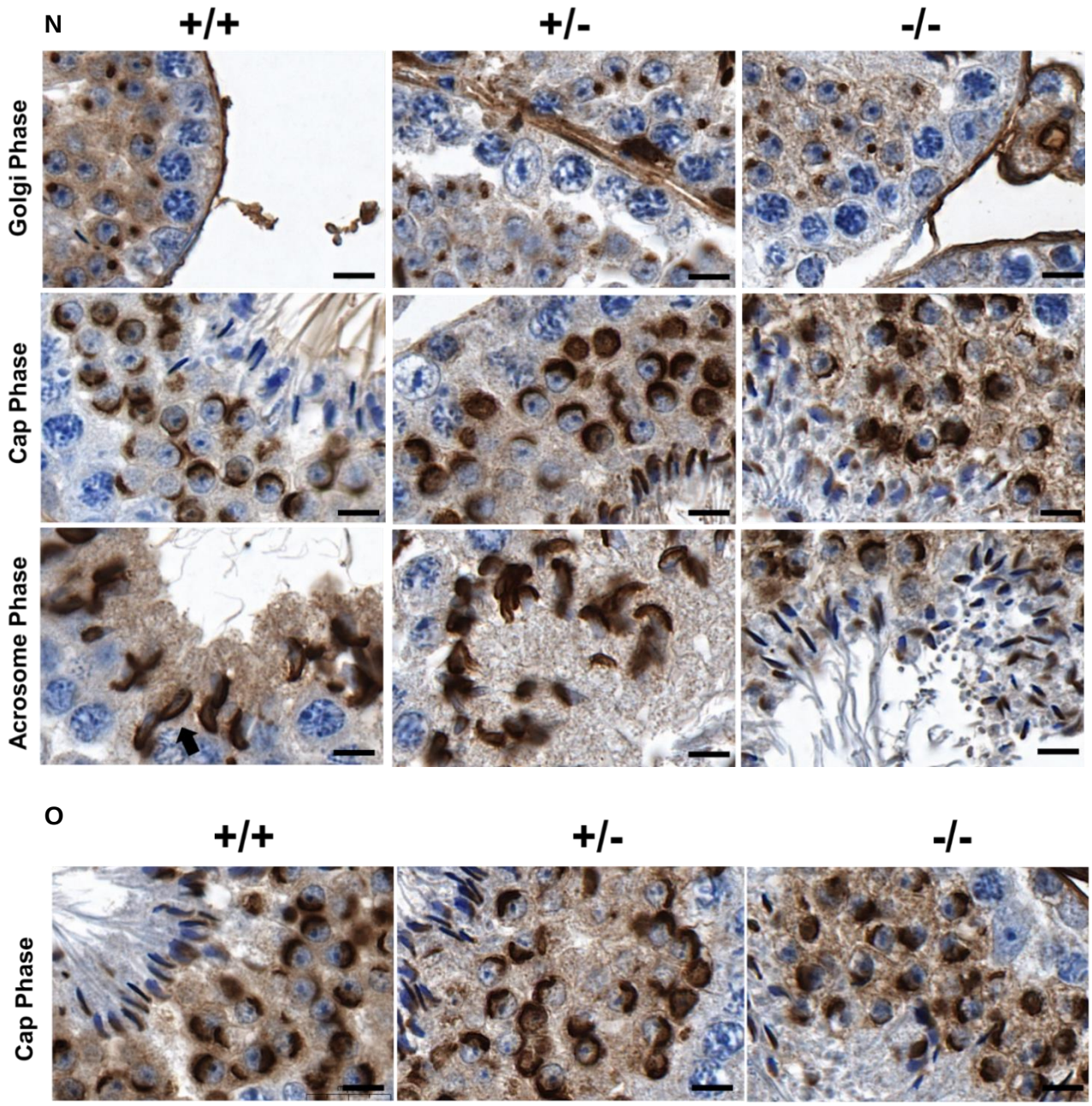

Figure 31: Ultrastructural analysis using TEM on testes sections of WT, *Pfn4*$^{+/-}$ and *Pfn4*$^{-/-}$ mice. Golgi phase spermatozoa of **(A)** WT, **(B)** *Pfn4*$^{+/-}$ **(C)** *Pfn4*$^{-/-}$ mice (arrow indicates deformed developing acrosome). Cap phase spermatozoa of **(D)** WT, **(E)** *Pfn4*$^{+/-}$ and **(F)** *Pfn4*$^{-/-}$ mice (arrow indicates deformed developing acrosome). Acrosome phase spermatids of **(G)** WT, **(H)** *Pfn4*$^{+/-}$ and **(I)** *Pfn4*$^{-/-}$ mice. Maturation phase spermatids of **(J)** WT , **(K)** *Pfn4*$^{+/-}$ and **(L)** *Pfn4*$^{-/-}$ mice. red arrow indicates the acroplaxome, red dotted rectangles indicate the marginal ring. **(M)** Ultrastructure analysis on cauda epididymal sperms of WT, *Pfn4*$^{+/-}$ and *Pfn4*$^{-/-}$ mice. Scale bar = 2µm. **(N)** IHC staining using anti-Sp56 antibody on testes sections of WT, *Pfn4*$^{+/-}$ and *Pfn4*$^{-/-}$ mice for Golgi, Cap and Acrosomal Phase. Scale bar= 20µm. **(O)** IHC

staining using anti-acrosin antibody on testes sections of WT, *Pfn4*$^{+/-}$ and *Pfn4*$^{-/-}$ mice. Scale bar= 20µm.

6.7 Loss of *Pfn4* resulted in fragmented Golgi network

The Golgi apparatus is responsible to release proacrosomal vesicles for the formation of acrosome during the Golgi phase of acrosome biogenesis (Tang, Lalli and Clermont, 1982). We therefore examined the orientation and morphology of the Golgi network domains. Immunofluorescence (IF) staining was performed using GM130 and TGN46 as markers for the *cis*- and *trans*-Golgi networks respectively. GM130 plays a crucial role in vesicle tethering, fusion and maintaining *cis*-Golgi structural integrity (Tiwari et al., 2019), while TGN46 is important for formation of exocytic vesicles and secretion from the *trans*-part of the Golgi network (Huang et al., 2019). Compared to WT (Figure 32 A, D) and *Pfn4*$^{+/-}$ (Figure 32 B, E) spermatids, IF staining showed defective and fragmented *cis*- (Figure 32 C) and *trans*-Golgi network (Figure 32 F) in *Pfn4*$^{-/-}$ testis sections. In *Pfn4*$^{-/-}$ testis sections, structural disruption and mild mis-localization of *cis*-Golgi network is observed, and *trans*-Golgi is fragmented and dispersed throughout the cytoplasm indicating impaired vesicle trafficking and transport unlike in WT and *Pfn4*$^{+/-}$ spermatids, where *cis- and trans*- Golgi are properly formed and aligned. These effects indicate that loss of PFN4 results in the disorganization of the Golgi sub-domains leading to malformed proacrosomal vesicles which seem to impair acrosome biogenesis.

Furthermore, we checked the localization of COPA (Coatomer *protein* complex subunit α), PICK1 (*Protein* Interacting with C Kinase - 1) and GOPC (Golgi Associated PDZ And Coiled-Coil Motif Containing) using IHC on testes sections of WT, *Pfn4*$^{+/-}$ and *Pfn4*$^{-/-}$ mice. COPA is essential for cargo transport of Golgi derived proteins (Lepelley et al., 2020), PICK1 and GOPC play an important role for vesicle trafficking released from Golgi network and further associated with the proacrosomal granule formation (Xiao et al., 2009). Our IHC showed that COPA is mis-localized (arrow heads) in localized *Pfn4*$^{-/-}$ spermatids, indicating the disrupted vesicle transport for acrosome biogenesis while in in WT and *Pfn4*$^{+/-}$ developing spermatids COPA is localized in Golgi apparatus (black arrows) (Figure 32 G). IHC using anti-PICK1 and anti-GOPC antibodies showed mis localization of Golgi in *Pfn4*$^{-/-}$ testes sections, while in WT and *Pfn4*$^{+/-}$ testes sections (black arrows) staining showed proper Golgi localization (Figure 32 H, I). These results further indicates that vesicle trafficking is affected in *Pfn4*$^{-/-}$ mice which ultimately result in abnormal formation of proacrosomal granules.

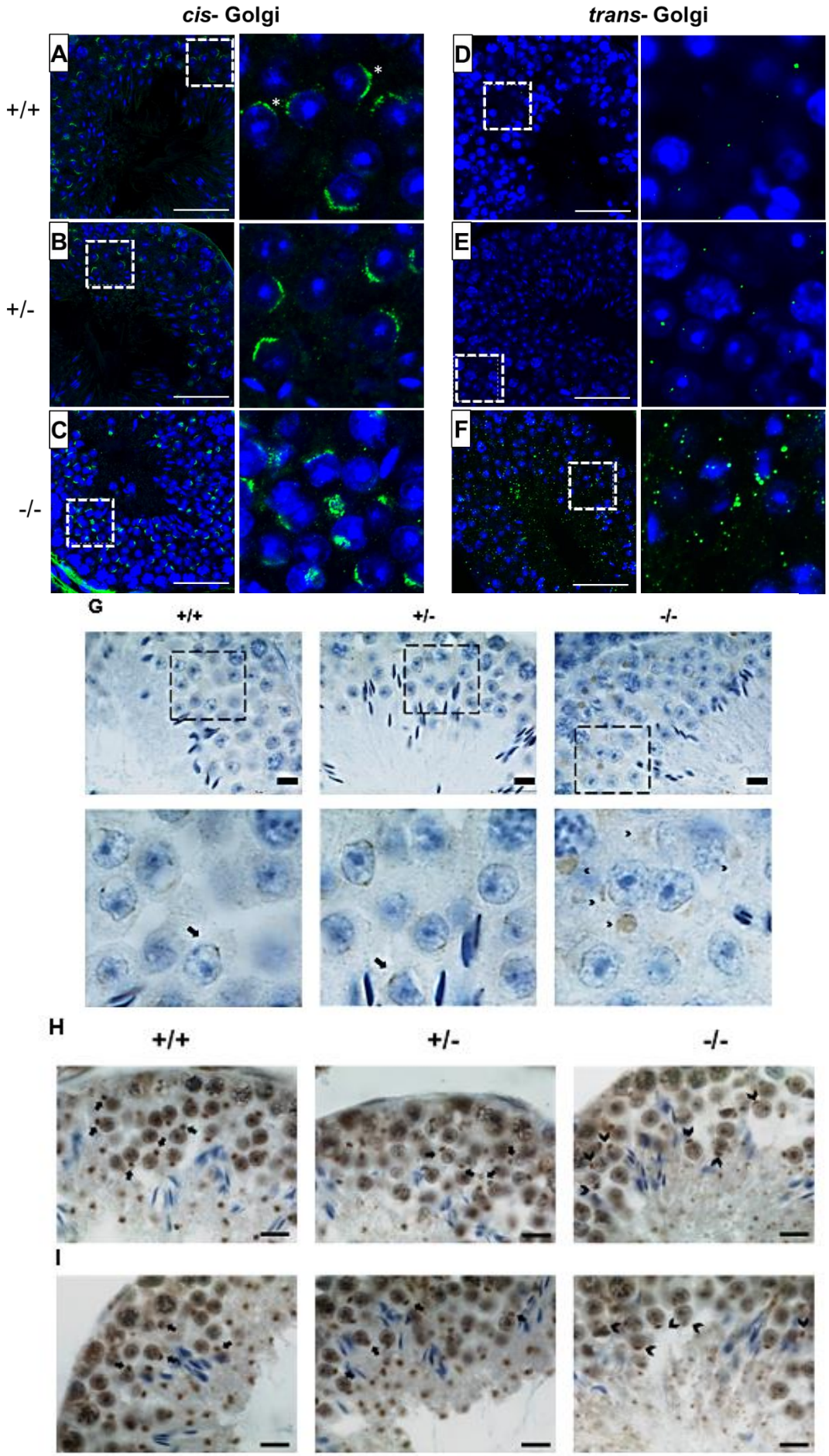
cis- Golgi
trans- Golgi
A
B
C
D
E
F
+/+
+/-
-/-
G
+/+
+/-
-/-
H
+/+
+/-
-/-
I

Figure 32: *Cis*-and *trans*-Golgi immunofluorescence staining using GM130 (green) and TGN46 (green) antibody and nuclei stained with DAPI (blue) on WT, *Pfn4*$^{+/-}$ and *Pfn4*$^{-/-}$ (n=3/genotype) testes sections. **(A)** WT and **(B)** *Pfn4*$^{+/-}$ and **(C)** *Pfn4*$^{-/-}$ spermatozoa stained for *cis*-Golgi compartment (asterisks). **(D)** WT, **(E)** *Pfn4*$^{+/-}$ and **(F)** *Pfn4*$^{-/-}$ spermatozoa stained for *trans*-Golgi network. Scale bar = 50µm. **(G)** anti-COPA, **(H)** anti-PICK1, and **(I)** anti-GOPC antibodies on WT, *Pfn4*$^{+/-}$ and *Pfn4*$^{-/-}$ testes sections. arrows indicate fine localization of Golgi; arrow heads indicate big Golgi clumps in **(G)** and miss localization in **(H, I)**. Scale bar= 20µm.

6.8 Disrupted PI3K/AKT and AMPK/mTOR signaling pathways leads to inhibited autophagy in *Pfn4*$^{-/-}$ mice

In order to gain insight into the molecular mechanisms affecting the process of Golgi vesicle trafficking, liquid chromatography- mass spectrometry (LC-MS) was performed on the protein lysates extracted from testes. A principal component analysis (PCA) performed on the top 5% proteins with highest variance across samples showed overall biological difference between all three genotypes (WT, *Pfn4*$^{+/-}$ and *Pfn4*$^{-/-}$) and the knockout replicates clustering apart from controls (Figure 33 A).

Eleven proteins were differentially abundant when comparing *Pfn4*$^{-/-}$ samples to *Pfn4*$^{+/-}$ samples, however, significantly differentially abundant proteins were not detected in *Pfn4*$^{-/-}$ samples compared to the WT (Figure 33 B). The effect of PFN4 deficiency is likely restricted to the round spermatid stages. Since proteins were extracted from the whole testis, the samples include proteins from a very heterogenous cell population. This could lead to difficulties in detecting signals of differential abundance due to PFN4 deficiency.

However, visualization of the data by heatmap showed that in *Pfn4*$^{-/-}$ extracts three proteins ARF2:ARF3, SPECC1L and FKBP1A were moderately more abundant compared to *Pfn4*$^{+/+}$and *Pfn4*$^{+/-}$ (Figure 33 C). These proteins are involved in the *trans*-Golgi network, vesicle tethering and are regulators of autophagy. To validate these results, Western Blots on protein lysates from testes were performed. Here, enhanced levels of ARF3, SPECCL1L and FKBP1 were detected in *Pfn4*$^{-/-}$ testes. (Figure 33 D). Further, pathways for autophagy, PI3K/AKT and mTOR signaling, protein processing in Endoplasmic reticulum (ER) and Golgi vesicle transport were enriched in *Pfn4*$^{-/-}$ (Figure 33 E). Next, we aimed to validate this upregulation of P13K/AKT and AMPK/mTOR signaling in PFN4-deficient mice. PI3K/AKT and mTOR/AMPK regulate the autophagic flux. mTOR and AMPK are negative and positive

regulators of autophagy respectively. Western blot analyses showed increased protein levels for AKT (total), AKT1 (phosphorylated), PI3K (total) and phospho-P13K (phosphorylated), mTOR and phospho-mTOR, while the level of phospho-AMPKα was reduced in *Pfn4*$^{-/-}$ testes (Figure 33 F). These results together indicate that loss of PFN4 affects autophagy-related signaling pathways PI3K/AKT, mTOR as well as protein processing in endoplasmic reticulum *trans*-Golgi network (ER-TGN).

Next, we investigated whether the altered levels of PI3K/AKT, and mTOR/AMPK affect the formation of the autophagosome. Therefore, levels of LC3B-I/II, a marker for autophagy activation, and SQSTM1 (p62), a marker for autophagic/lysosomal degradation were analyzed using Western blot. The immunoblot showed elevated protein levels of LC3B-I/II and P62 in PFN4-deficient testis (Figure 33 G). Furthermore, increased protein levels of LC3II, SQSTM1, AKT1 and ARF3 were also confirmed by IHC (Figure 33 H). Quantitating the western blots showed increased protein levels for LC3BI/II, SQSTM1, ARF3, FKBP1, SPECC1L, AKT1, AKT, mTOR, p-mTOR, p-PI3K, PI3K and decreased for AMPK (Figure 33 I). These results suggest that the autophagic flux is impaired leading to inhibition of autophagy.

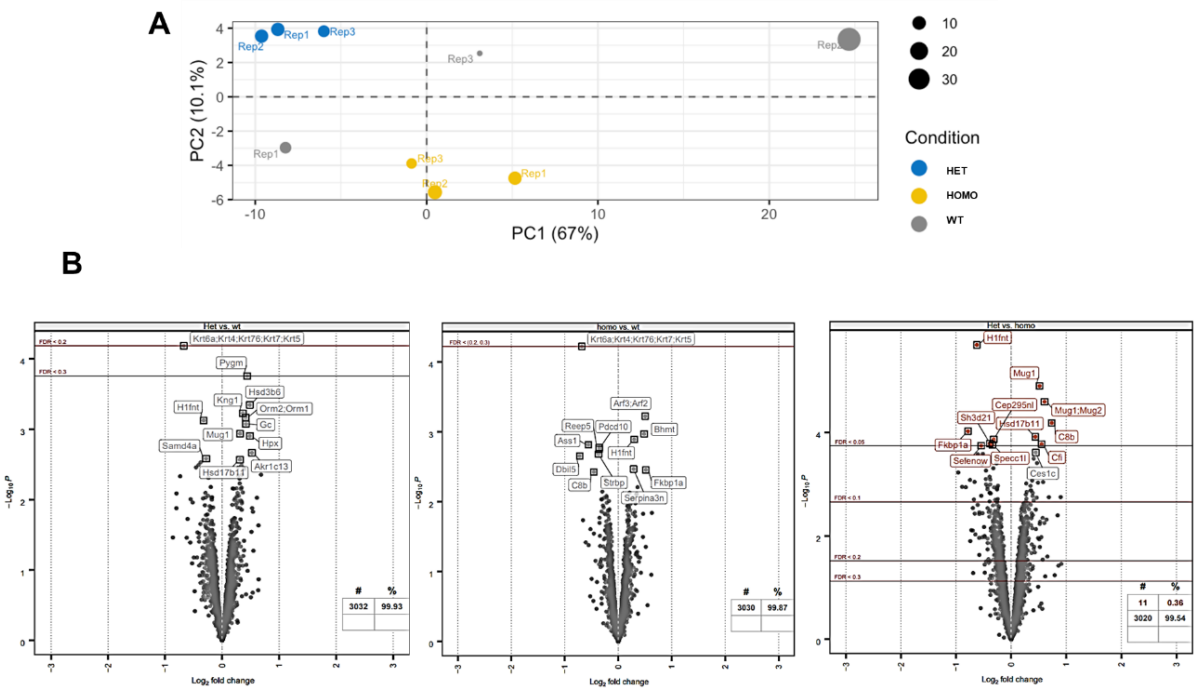

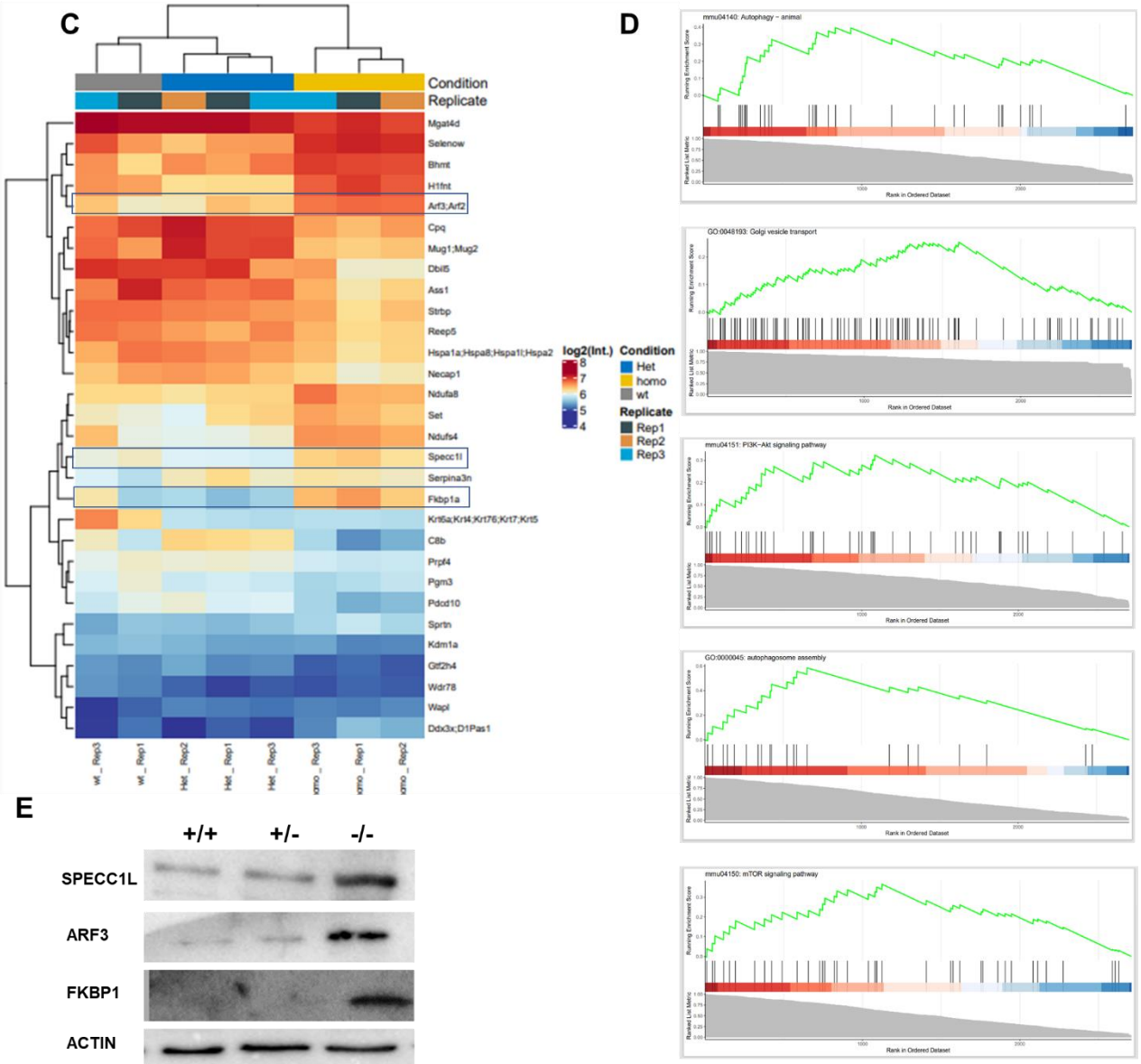
C
Condition
Replicate
Mgat4d
Selenow
Bhmt
H1fnt
Arf3;Arf2
Cpq
Mug1;Mug2
Dbil5
Ass1
Strbp
Reep5
Hspa1a;Hspa8;Hspa1l;Hspa2
Necap1
Ndufa8
Set
Ndufs4
Specc1l
Serpina3n
Fkbp1a
Krt6a;Krt4;Krt76;Krt7;Krt5
C8b
Prpf4
Pgm3
Pdcd10
Sprtn
Kdm1a
Gtf2h4
Wdr78
Wapl
Ddx3x;D1Pas1
wt_Rep3
wt_Rep1
Het_Rep2
Het_Rep1
Het_Rep3
homo_Rep3
homo_Rep1
homo_Rep2
log2(Int.)
8
7
6
5
4
Condition
Het
homo
wt
Replicate
Rep1
Rep2
Rep3
D
mmu04140: Autophagy - animal
GO:0048193: Golgi vesicle transport
mmu04151: PI3K-Akt signaling pathway
GO:0000045: autophagosome assembly
mmu04150: mTOR signaling pathway
Running Enrichment Score
Ranked List Metric
Rank in Ordered Dataset
E
+/+
+/-
-/-
SPECC1L
ARF3
FKBP1
ACTIN
F
+/+
+/-
-/-
AKT1
ACTIN
AKT
PI3K
p-PI3K
mTOR
p-mTOR
p-AMPK
ACTIN
G
+/+
+/-
-/-
LC3I
LC3II
SQSTM1
ACTIN

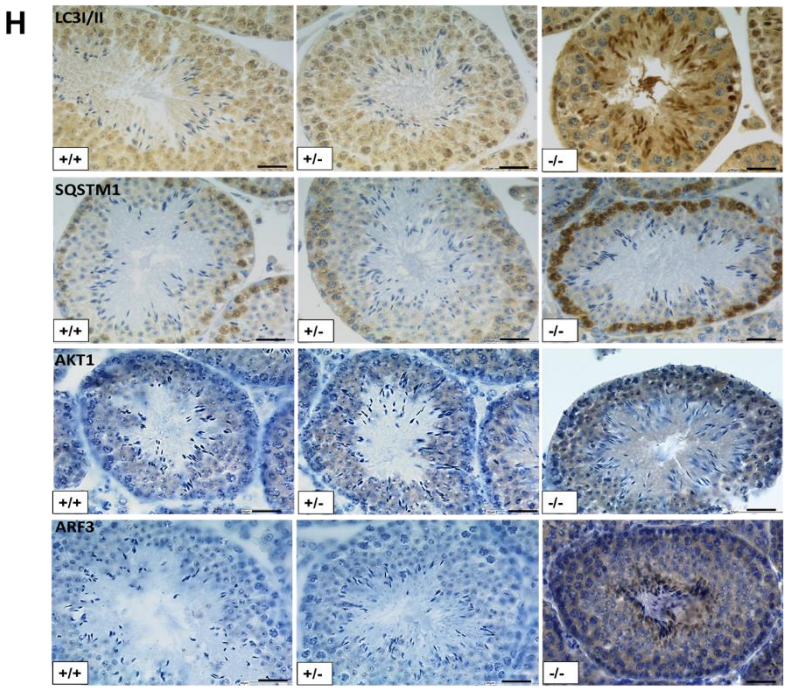

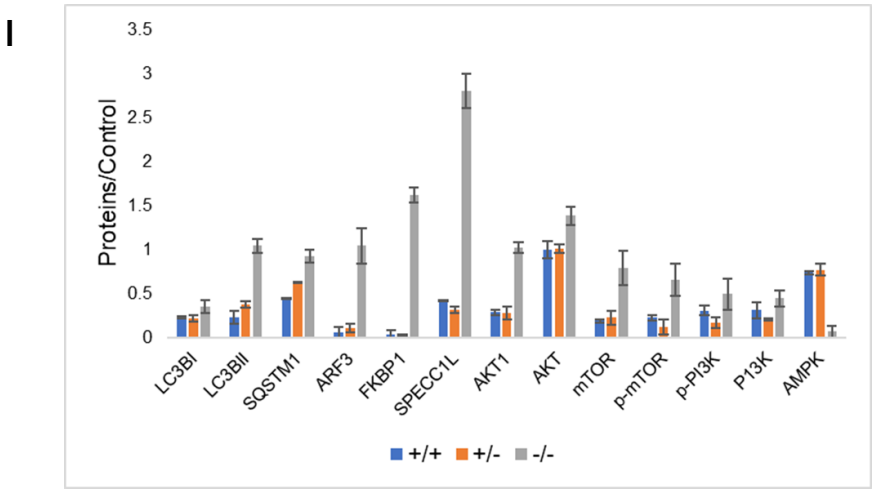

Figure 33: Mass spectrometry and western blot analyses. **(A)** Principal component analysis on mass spectrometry data of WT, *Pfn4*$^{+/-}$ and *Pfn4*$^{-/-}$ samples. Contribution of each data set in PCA represented by the dot size. **(B)** Volcano plots for WT and *Pfn4*$^{+/-}$, WT and *Pfn4*$^{-/-}$, *Pfn4*$^{+/-}$ and *Pfn4*$^{-/-}$ contrasts. **(C)** Heatmap visualization of 30 deregulated proteins between WT, *Pfn4*$^{+/-}$ and *Pfn4*$^{-/-}$ samples. **(D)** Enrichment pathway analysis of proteins on WT and *Pfn4*$^{-/-}$ samples. Western blot analysis and immunohistochemical staining on WT, *Pfn4*$^{+/-}$ and *Pfn4*$^{-/-}$ mice. **(E)** SPECC1L, ARF3 and FKBP1 antibody on protein extracts from WT, *Pfn4*$^{+/-}$ and *Pfn4*$^{-/-}$ testes. **(F)** WB using AKT, AKT1, PI3K, p-PI3K, mTOR, p-mTOR and p-AMPK antibody on protein extracts from WT, *Pfn4*$^{+/-}$ and *Pfn4*$^{-/-}$ testes. **(G)** WB using LC3I/II and SQSTM1 antibodies on protein extracts from WT, *Pfn4*$^{+/-}$ and *Pfn4*$^{-/-}$ testes. **(H)** IHC using LC3I/II, SQSTM1, AKT1,

and ARF3 antibodies on WT, *Pfn4*$^{+/-}$ and *Pfn4*$^{-/-}$ testes sections. Scale bar = 50µm. **(I)** Protein quantification of WT, *Pfn4*$^{+/-}$ and *Pfn4*$^{-/-}$. LC3BI/II, SQSTM1, ARF3, FKBP1, SPECC1L, AKT1, AKT, MTOR, P-MTOR, P-PI3K, PI3K protein levels are increased and similarly AMPK protein level are reduced in *Pfn4*$^{-/-}$ mice. Details

6.9 Acrosomal reaction significantly reduced in *Pfn4*$^{-/-}$ sperm

As a result of the impaired acrosome biogenesis, we expected that the acrosomal reaction to be affected. To induce the acrosomal reaction, we used A23187 and Coomassie staining to differentiate the acrosome-reacted sperm (acrosome is not present on sperm head) (Figure 34 A, black arrows) to non-acrosomal reacted sperm (acrosome is detectable as a crescent like shape (dark blue) on the sperm head) (Figure 34 A, black arrowheads). Using the bright field microscope 200 spermatozoa in triplicates for each genotype is accessed. Acrosomal reaction was assessed by the absence of acrosome (a dark blue crescent shape on sperm head). Upon exposure to A23187, more than 72% of sperm from WT mice and ~65% of sperm from *Pfn4*$^{+/-}$ mice (Figure 35 B) showed acrosomal exocytosis, whereas only 5-6% sperm of the *Pfn4*$^{-/-}$ underwent acrosome reaction (Figure 34 B). This finding demonstrates that sperm of *Pfn4*$^{-/-}$ males display significantly disturbed acrosome function.

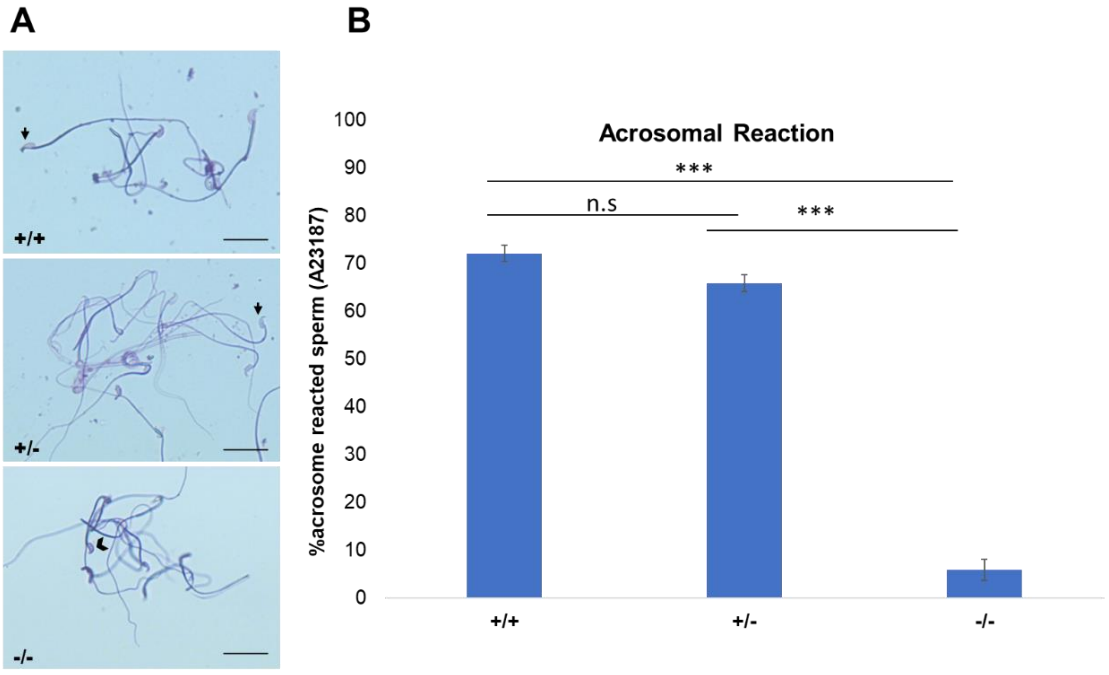

Figure 34: The acrosomal reaction (AR) using calcium ionophore WT, *Pfn4*$^{+/-}$ and *Pfn4*$^{-/-}$ sperm cells. **(A)** Coomassie-stained sperm cells of WT, *Pfn4*$^{+/-}$ and *Pfn4*$^{-/-}$ Black arrow indicate successful acrosomal reaction took place. A black arrowhead indicates a crescent-shape

acrosome on sperm head, indicating acrosomal reaction did not take place. **(B)** Percentage of acrosomal-reacted sperm WT, *Pfn4*$^{+/-}$ and *Pfn4*$^{-/-}$ (n= 3 biological replicates/genotype, ***p<0.0005, Student's t-test, one tail, paired).

6.10 *Pfn4* deficient sperm are able to fertilize zona-free oocytes

Since the PFN4-deficient sperm display defects in acrosome function, we performed IVF (in-vitro fertilization) on zona free oocytes to test the fertilizing ability of *Pfn4*$^{-/-}$ sperm.

Using *Pfn4*$^{-/-}$ sperm ~30% of oocytes developed into morula/blastocyst stage (Figure 35). Using wildtype sperm, ~70% of oocytes developed to morula stage. This result demonstrates that the acrosome is defective, but the DNA seems to be intact. This experiment was done without proper control; therefore, it is necessary to repeat the experiment with proper control.

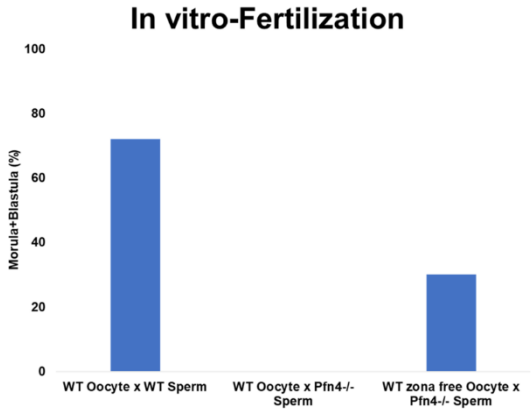

Figure 35: In-vitro fertilization performed on zona free oocytes with WT and *Pfn4*$^{-/-}$ sperms. Percentage of oocytes developing into blastocysts. Fertilizing oocytes with WT and *Pfn4*$^{-/-}$ sperm and zona-free oocytes with *Pfn4*$^{-/-}$ sperm.

6.11 Actin cytoskeletal organization is normal in *Pfn4*$^{-/-}$ seminiferous epithelium

In order to check whether loss of PFN4 also affects the actin cytoskeletal organization in testicular seminiferous tubules, we performed the phalloidin staining on testes section for WT, *Pfn4*$^{+/-}$ and *Pfn4*$^{-/-}$ mice. Actin cytoskeletal is important for migration of germ cell from apical to basal of seminiferous tubules, and maintenance of cell-cell (Sertoli-spermatids) interactions (Kanatsu-Shinohara et al., 2008). Interestingly, we found that the dynamic network of actin cytoskeleton is comparable for all three genotypes (Figure 36). This result suggests that loss of PFN4 didn't impede the actin assembly in seminiferous epithelium of testes.

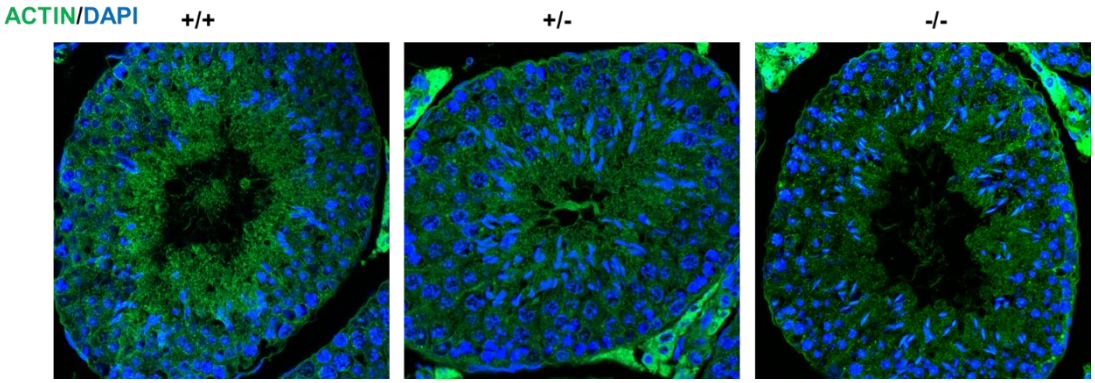

Figure 36: Phalloidin Staining on testes sections of WT, *Pfn4*$^{+/-}$ and *Pfn4*$^{-/-}$ mice. Scale bar= 20µm.

6.12 Apoptosis and phagocytosis are not observed in *Pfn4*$^{-/-}$ mice

To find whether the inhibited autophagy cause apoptosis in *Pfn4*$^{-/-}$ testes section, IHC was performed using apoptotic markers, cleaved caspase-3, -9 and active caspase 3. Upon apoptosis caspases are actively transported into nucleus and result in cell death. Interestingly, IHC showed no signal for germ cell death in *Pfn4*$^{-/-}$ testes, which is comparable to WT and *Pfn4*$^{-/-}$ sections (Figure 37 A). Further, we performed TEM analysis on testes section to find the phagocytosis of germ cells by Sertoli cells. Surprisingly, phagocytosis was not observed in *Pfn4*$^{-/-}$ Sertoli cells, which is comparable to WT and *Pfn4*$^{+/-}$ sections (Figure 37 B).

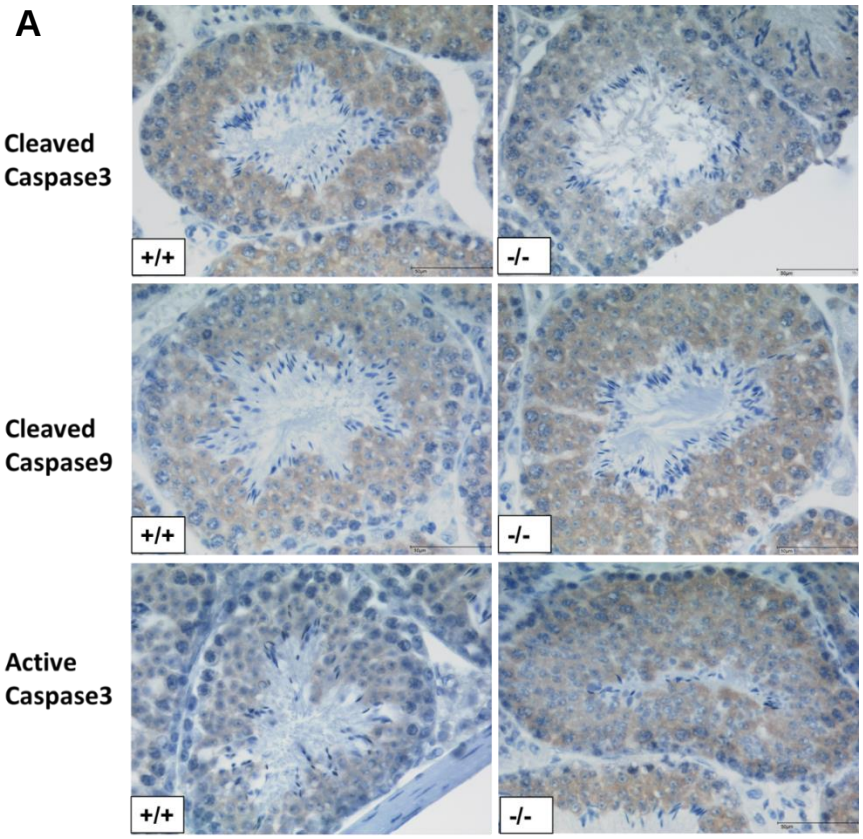

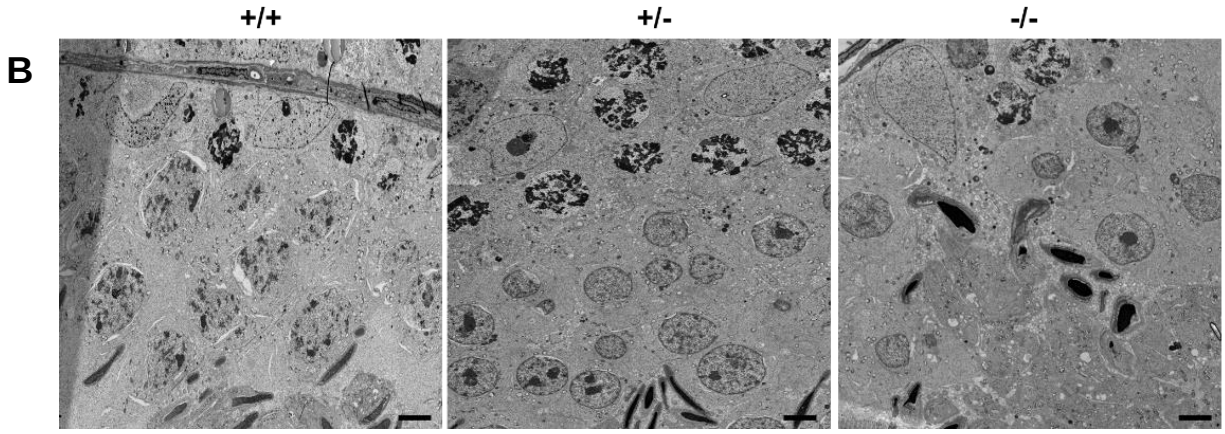

Figure 37: Apoptosis and phagocytosis analysis. **(A)** IHC of Caspase-3, -9 and active caspase-3 on testes sections of WT, *Pfn4*$^{+/-}$ and *Pfn4*$^{-/-}$ mice. Scale bar= 20µm. **(B)** Ultrastructure analysis using TEM on testes section of WT, *Pfn4*$^{+/-}$ and *Pfn4*$^{-/-}$ mice. Scale bar= 10µm.

7. DISCUSSION II

Here, we established and analyzed mouse lines deficient in PFN4 and demonstrate that lack of PFN4 leads to male infertility. We show that in PFN4-null spermatids showed malformed formation of manchette and flagella. Arrested manchette development is the main cause of abnormal formation of sperm heads, while flagellar defects contribute to reduced sperm motility and quantity. We further revealed that acrosome biogenesis is impaired. Defects in acrosome biogenesis seems to originate from a malfunctioning Golgi network, which is incapable of forming proper acrosomal vesicle. As a consequence, formation of large acrosomal vesicles is inhibited. Proteomic analysis revealed an enrichment of PI3K/AKT and mTOR pathways in *Pfn4*$^{-/-}$ mice which was confirmed by Western blot. Therefore, LC3I/II and SQSTM1 protein levels were increased, indicating inhibition of autophagy. Finally, we demonstrate that zona free oocytes treated with *Pfn4*$^{-/-}$ sperm develop up to morula stage suggesting that PFN4 is required for proper acrosome biogenesis and function.

The phenotype observed in PFN4-deficient mice correlates with PFN4 protein sub-cellular localization in acrosome and manchette (Behnen et al., 2009). We observed defects in manchette development which seems to result in the amorphous head shape of *Pfn4*$^{-/-}$ sperm. Further, we provide evidence, that the flagellar structure is affected by the impaired manchette. In addition, acrosome biogenesis is aberrant partially, starting from the Golgi phase in *Pfn4*$^{-/-}$ mice. Hence, we showed that PFN4 contributes to manchette formation, protein transport, flagellar structural integrity, sperm motility and acrosome biogenesis and sperm head morphology.

Pfn4$^{-/-}$ mice display severely reduced sperm viability due to severe defects in sperm membrane integrity. The infertility seems to be mainly caused by perturbation of manchette development and acrosome biogenesis.

PFN4 is localized in the manchette of spermatids during elongation steps (Behnen et al., 2009). Several studies on spermiogenesis related genes (e.g.: *Hook1* (Mendoza-Lujambio et al., 2002), *Itf 20* (Li et al., 2016), *Pfn3* (Umer et al., 2021), *spag17* (Kazarian et al., 2018) , *Lrguk1* (Okuda et al., 2017), *Spef2* (Lehti et al., 2017), *Gopc* (Yao et al., 2002) and *Cdc42* (Chapin et al., 2001)) showed aberrant manchette development resulting in altered sperm head shaping. The manchette and nucleus are connected with linkers, suggesting a structural relationship between

manchette and nucleus. Furthermore, clutching forces exerted by the manchette are responsible for the shaping of the sperm head (Kierszenbaum and Tres, 2004).

In addition, we observed the disrupted localization of HOOK1 and ARL3 in manchette of *Pfn4*$^{-/-}$ testes sections. Interestingly HOOK1 deficient males display a similar phenotype (impaired manchette and flagellar development, abnormal sperm head shape, reduced motility and malformed acrosome formation) as we observed in our *Pfn4*$^{-/-}$ males (Schwarz et al., 2017). Recently it has been reported that HOOK1 interacts with CCDC181 (coiled-coil domain containing protein 181) and plays a role in flagellar development and regulation (Schwarz et al., 2017). HOOK1 acts as cargo protein in intra-manchette transport (IMT) process for CCDC181 protein. ARL3 plays a role in cargo transport for axoneme formation and essential for ciliogenesis (Alkanderi et al., 2018**).** We speculate that PFN4 plays a role as structural and cargo protein, where it might participate in binding motor proteins and transport their cargo to specific locations during sperm development. We further hypothesize that PFN4 might interact directly or in a complex with HOOK1 and ARL3. Unfortunately, due to lack of PFN4-antibody, is needed to detail the localization of PFN4 Protein (at ultrastructural level) in sperm flagellar as well as lacking the Co-IP experiments to find its interacting partners. The localization of PFN4 to the manchette suggests a role in its organization and/or remodeling. PFN3 also localized in the manchette and *Pfn3*$^{-/-}$ mice showed amorphous sperm head morphology as a result of abnormal manchette development, which is comparable to the phenotype of *Pfn4*$^{-/-}$ mice.

As described previously, manchette also contributes to cargo of motor proteins before transporting them for tail formation through IMT. We observed flagellar defects which contributes to the reduced sperm motility in PFN4-deficient mice. The phenotypic similarities observed in other knockout mouse models i.e., LRGUK (Liu et al., 2015)**,** MEIG1 (Li et al., 2015), PACRG (Li et al., 2015), SUN4 (Calvi et al., 2015), HOOK1 (Mendoza-Lujambio et al., 2002), and GOPC (Yao et al., 2002), emphases the perpetuity of protein transport mechanism. This underlies the movement of proteins via acrosome-acroplaxome-manchette-tail association for manchette development, sperm head shaping, acrosome biogenesis, maintaining Golgi sub-domains, and flagella formation. Observed reduction in sperm count of *Pfn4*$^{-/-}$ males most probably is the result of reduced sperm motility. Of-note, we used the swim-out method for counting the sperm, which is the probable cause of reduced sperm count. However, to elucidate the role of PFN4 in IFT during late steps of development of sperm tail needs further studies.

Ultrastructural examination of *Pfn4*$^{-/-}$ sperm revealed that round spermatids fail to properly fuse proacrosomal granules/vesicles to form the acrosome. Further analysis using *cis*- and *trans*-Golgi markers indicate that the structural disorganization of Golgi sub domains might be the reason for aberrant proacrosomal vesicle formation and fusion during acrosome biogenesis. IHC using Sp56 and acrosin also showed disturbed acrosome biogenies in PFN4-deficient mice. These results suggest a role of PFN4 in vesicle trafficking and protein transport from Golgi network for acrosome biogenesis. Interestingly, PICK1, GM130, and PFN3 proteins, have been shown to localize to the Golgi apparatus as well. Mice deficient for these genes also displayed a fragmented Golgi network resulting in impaired acrosome development due to failure of proacrosomal granule fusion, as observed in PFN4 knockouts.

In addition, several proteins such as COPA, PICK1, and GOPC plays a role in vesicle trafficking and transport. It has been reported that mutations in COPA led to aberrant protein trafficking (Lepelley et al., 2020). We observed mis-localization of COPA, PICK1 and GOPC in PFN4-deficient mice which suggest the disturbed vesicle trafficking and transport and result in arrested acrosome formation. We hypothesis that PFN4 might interacts directly or indirectly with other proteins such as COPA, PICK1, and GOPC which is crucial for protein transport and trafficking, and loss of PFN4 might disturb this complex. However, further experiments are needed to be done to find PFN4 interacting partners.

We reported (Umer *et al*., 2021) that PFN3 is located in Golgi-apparatus, acrosome, and manchette, and hence is similar to PFN4 in sub-cellular localization (Behnen et al., 2009). Both *Pfn3*$^{-/-}$ and *Pfn4*$^{-/-}$ male mice displayed impaired acrosome biogenesis with disrupted Golgi sub-domains. However, *Pfn4*$^{-/-}$ mice showed more dramatic phenotype in terms of sperm viability, acrosome biogenesis and fertility compared to *Pfn3*$^{-/-}$ mice. We speculate, that this is due to PFN4 affecting the main signaling pathway of autophagy (PI3K/AKT), while PFN3 affects only downstream targets (mTOR/AMPK) of autophagy (Umer *et al*., 2021).

Protein trafficking from Golgi network is vital throughout the process of sperm differentiation. During acrosome development, proacrosomal vesicles are released from the *trans*-Golgi network and fuse to form the acrosome (Tang, Lalli and Clermont, 1982). In acrosome biogenesis components of the autophagy network play a role (Umer et al., 2021). They modulate proacrosomal formation, and support transport and fusion towards nucleus for acrosome development (Shang et al., 2016). Key regulators of autophagy are P13K/AKT and mTOR. Imbalance in these factors leads to inhibition of autophagy (Xu et al., 2020). We

demonstrate that protein levels of P13K, p-PI3K, AKT and AKT1 were increased in PFN4 knockouts, likely leading to the activation of mTOR, p-mTOR and suppression of AMPK, resulting in autophagy inhibition. The increase of LC3BI/II and SQSTM1 protein levels in *Pfn4*$^{-/-}$ males suggests, that autophagosomes accumulate. Ultimately, this seems to result in a blockage of autophagic flux and impaired acrosome biogenesis in PFN4-deficient mice.

SIRT1(Liu et al., 2017) and ATG7 (Wang et al., 2014) deficient mice showed inhibited autophagy, resulting in LC3BI/II and SQSTM1 accumulation and failure of proacrosomal granule formation and fusion. Our study on *Pfn3*$^{-/-}$ shows disturbance in mTOR/AMPK pathway along with the accumulation of autophagosomes (Umer et al., 2021). This suggest that SIRT1 and ATG7 proteins play a role in downstream cascade, while PFN3 protein is essential for regulating the central player (mTOR) of autophagy. However, PFN4 seems to play a role in the upstream PI3K/AKT signaling mechanism of autophagy.

Proteomics analysis of *Pfn4*$^{-/-}$ mice indicated moderate deregulation of SPECC1L, ARF2:3 and FKBP1 proteins. They play a role in PI3K signaling, *trans*-Golgi network and vesicle tethering and transport. SPECC1L (Sperm Antigen with Calponin Homology and Coiled-Coil Domains 1 Like) known as a novel modulator of PI3K/AKT signaling (Wilson et al., 2016), which is essential for autophagy regulation. *Specc1l* mutants showed reduced PI3K/AKT signaling (Wilson et al., 2016). We observed increased protein levels of SPECC1L in *Pfn4*$^{-/-}$ mice which seem to lead to the activation of PI3K/AKT signaling, as confirmed by enrichment and western blot analysis. Increased protein levels of AKT leads to activation of mTOR which results in the inhibition of autophagy (Hahn-Windgassen et al., 2005). ARF2:3 (ADP-ribosylation factor) and FKBP1 (FKBP Prolyl Isomerase 1A) localized in *trans*-Golgi network, play a role in post-Golgi trafficking and act as a sorting station from Golgi to plasma membrane (Manolea et al., 2010). Enrichment analysis further showed biological processes for protein transport are altered in *Pfn4*$^{-/-}$ mice. This suggest that loss of PFN4 might disturb the autophagy mechanism responsible for acrosome biogenesis, Golgi structural organization, vesicle formation, transport, and fusion.

Aberrant acrosome biogenesis is likely to responsible for disrupted acrosome reaction and inability of sperm to fertilize oocyte. Indeed, *Pfn4*$^{-/-}$ sperm showed a very low acrosomal exocytosis rate as compared to controls, but *Pfn4*$^{-/-}$ sperm were still able to fertilize oocytes after the removal of zona pellucida. Thus, impaired acrosome biogenesis seems to be at least

partly causal to the *Pfn4*$^{-/-}$ male infertility. In contrast to PFN3-deficient mice (Umer et al., 2021), acrosomal exocytosis is affected more severely in the PFN4-deficient mouse model.

In addition, we didn't observe any organizational defects in actin cytoskeletal in *Pfn4*$^{-/-}$ testes.This could be because of PFN4 does not retain the actin binding site, and actin organization and polymerization are affected only when F-actin capping, or cross-linking proteins junction get disturb. It has been also reported that actin filaments are clearly present on areas of Sertoli cell, most prominently at the adherent junction of Sertoli cell to the elongating spermatids and participate in spermatids movement when they released from Sertoli cells (Dunleavy et al., 2019).

Interestingly, we didn't observe male germ cell apoptosis and phagocytosis by Sertoli cells in our PFN4-deficient mice. This suggest that inhibited autophagy caused by disrupted signaling pathways does not contribute to apoptosis in testicular germ cells of *Pfn4*$^{-/-}$ males.

Our results suggest that PFN4 plays a role in vesicle trafficking from the Golgi network for acrosome biogenesis. In addition, we showed the deregulation of PI3K/AKT and mTOR/AMPK signaling pathways which results in the autophagy inhibition during acrosome biogenesis in *Pfn4*$^{-/-}$ mice. Furthermore, defects in manchette developments were observed, which seems to result in abnormal sperm head morphology.

8. REFERENCES

1. Abada, A., Elazar, Z., 2014. Getting ready for building: signaling and autophagosome biogenesis. EMBO reports 15, 839–852. https://doi.org/10.15252/embr.201439076
2. Agarwal, A., Mulgund, A., Hamada, A., Chyatte, M.R., 2015. A unique view on male infertility around the globe. Reproductive Biology and Endocrinology 13. https://doi.org/10.1186/s12958-015-0032-1
3. Akhmanova, A., Mausset-Bonnefont, A. L., van Cappellen, W., Keijzer, N., Hoogenraad, C. C., Stepanova, T., Drabek, K., van der Wees, J., Mommaas, M., Onderwater, J., van der Meulen, H., Tanenbaum, M. E., Medema, R. H., Hoogerbrugge, J., Vreeburg, J., Uringa, E. J., Grootegoed, J. A., Grosveld, F., & Galjart, N., 2005. The microtubule plus-end-tracking protein CLIP-170 associates with the spermatid manchette and is essential for spermatogenesis. *Genes & development*, *19*(20), 2501–2515. https://doi.org/10.1101/gad.344505
4. Alkanderi, S., Molinari, E., Shaheen, R., Elmaghloob, Y., Stephen, L.A., Sammut, V., Ramsbottom, S.A., Srivastava, S., Cairns, G., Edwards, N., Rice, S.J., Ewida, N., Alhashem, A., White, K., Miles, C.G., Steel, D.H., Alkuraya, F.S., Ismail, S. and Sayer, J.A., 2018. ARL3 Mutations Cause Joubert Syndrome by Disrupting Ciliary Protein Composition. *American Journal of Human Genetics*, 103(4), pp.612–620. https://doi.org/10.1016/j.ajhg.2018.08.015.
5. Alquézar-Baeta, C., Gimeno-Martos, S., Miguel-Jiménez, S., Santolaria, P., Yániz, J., Palacín, I., Casao, A., Cebrián-Pérez, J. Á., Muiño-Blanco, T., & Pérez-Pé, R., 2019. OpenCASA: A new open-source and scalable tool for sperm quality analysis. *PLoS Computational Biology*. doi: 10.1371/journal.pcbi.1006691
6. Allais-Bonnet, A., Pailhoux, E., 2014. Role of the prion protein family in the gonads. Frontiers in Cell and Developmental Biology 2. https://doi.org/10.3389/fcell.2014.00056
7. Amaral, A., Lourenço, B., Marques, M., Ramalho-Santos, J., 2013. Mitochondria functionality and sperm quality. Reproduction. https://doi.org/10.1530/REP-13-0178
8. Avella, M.A., Dean, J., 2011. Fertilization with acrosome-reacted mouse sperm: Implications for the site of exocytosis. Proceedings of the National Academy of Sciences of the United States of America. https://doi.org/10.1073/pnas.1118234109

9. Bansal, S.K., Gupta, N., Sankhwar, S.N., Rajender, S., 2015. Differential genes expression between fertile and infertile spermatozoa revealed by transcriptome analysis. PLoS ONE 10, 1–21. https://doi.org/10.1371/journal.pone.0127007
10. Behnen, M., Murk, K., Kursula, P., Cappallo-Obermann, H., Rothkegel, M., Kierszenbaum, A.L., Kirchhoff, C., 2009. Testis-expressed profilins 3 and 4 show distinct functional characteristics and localize in the acroplaxome-manchette complex in spermatids. BMC Cell Biology 10. https://doi.org/10.1186/1471-2121-10-34
11. Berruti, G., & Paiardi, C., 2015. USP8/UBPy-regulated sorting and the development of sperm acrosome: The recruitment of MET. *Reproduction*, *149*(6), 633–644. doi: 10.1530/REP-14-0671
12. BIGGERS, J.D., FINN, C.A., McLAREN, A., 1962. Long-term reproductive performance of female mice. I. Effect of removing one ovary. Journal of reproduction and fertility.
13. Bisht, S., Faiq, M., Tolahunase, M., Dada, R., 2017. Oxidative stress and male infertility. Nature Reviews Urology. https://doi.org/10.1038/nrurol.2017.69
14. Bourgon, R., Gentleman, R., Huber, W., 2010. Reply to Talloen et al.: Independent filtering is a generic approach that needs domain specif c adaptation. Proceedings of the National Academy of Sciences of the United States of America. https://doi.org/10.1073/pnas.1011698107
15. Bozic, M., van den Bekerom, L., Milne, B.A., Goodman, N., Roberston, L., Prescott, A.R., Macartney, T.J., Dawe, N., McEwan, D.G., 2020. A conserved ATG2-GABARAP family interaction is critical for phagophore formation. EMBO reports. https://doi.org/10.15252/embr.201948412
16. Calvi, A., Wong, A.S.W., Wright, G., Wong, E.S.M., Loo, T.H., Stewart, C.L., Burke, B., 2015. SUN4 is essential for nuclear remodeling during mammalian spermiogenesis. Developmental Biology 407, 321–330. https://doi.org/10.1016/j.ydbio.2015.09.010
17. Chapin, R.E., Wine, R.N., Harris, M.W., Borchers, C.H., Haseman, J.K., 2001. Structure and Control of a Cell-Cell Adhesion Complex Associated With Spermiation in Rat Seminiferous Epithelium, Journal of Andrology.
18. Custer, S.K., Foster, J.N., Astroski, J.W., Androphy, E.J., 2019. Abnormal Golgi morphology and decreased COPI function in cells with low levels of SMN. Brain Research. https://doi.org/10.1016/j.brainres.2018.11.005
19. Di Rienzo, M., Romagnoli, A., Antonioli, M., Piacentini, M., Fimia, G.M., 2020. TRIM proteins in autophagy: selective sensors in cell damage and innate immune responses. Cell Death and Differentiation. https://doi.org/10.1038/s41418-020-0495-2

20. Dong, J., Radau, B., Otto, A., Müller, E.C., Lindschau, C., Westermann, P., 2000. Profilin I attached to the Golgi is required for the formation of constitutive transport vesicles at the trans-Golgi network. Biochimica et Biophysica Acta - Molecular Cell Research 1497, 253–260. https://doi.org/10.1016/S0167-4889(00)00056-2
21. Durinck, S., Moreau, Y., Kasprzyk, A., Davis, S., De Moor, B., Brazma, A., Huber, W., 2005. BioMart and Bioconductor: A powerful link between biological databases and microarray data analysis. Bioinformatics. https://doi.org/10.1093/bioinformatics/bti525
22. Ernst, C., Eling, N., Martinez-Jimenez, C.P., Marioni, J.C., Odom, D.T., 2019. Staged developmental mapping and X chromosome transcriptional dynamics during mouse spermatogenesis. Nature Communications 10. https://doi.org/10.1038/s41467-019-09182-1
23. Fawcett, D.W., 1975. The mammalian spermatozoon. Developmental biology 44, 394–436. https://doi.org/10.1016/0012-1606(75)90411-x
24. Feng, Y., Yao, Z., Klionsky, D.J., 2015. How to control self-digestion: Transcriptional, post-transcriptional, and post-translational regulation of autophagy. Trends in Cell Biology. https://doi.org/10.1016/j.tcb.2015.02.002
25. Gareus, R., Di Nardo, A., Rybin, V., Witke, W., 2006. Mouse profilin 2 regulates endocytosis and competes with SH3 ligand binding to dynamin 1. Journal of Biological Chemistry. https://doi.org/10.1074/jbc.M503528200
26. Gervasi, M.G., Xu, X., Carbajal-Gonzalez, B., Buffone, M.G., Visconti, P.E., Krapf, D., 2018. The actin cytoskeleton of the mouse sperm flagellum is organized in a helical structure. Journal of Cell Science. https://doi.org/10.1242/jcs.215897
27. Gnoth, C., Godehardt, E., Frank-Herrmann, P., Friol, K., Tigges, J., Freundl, G., 2005. Definition and prevalence of subfertility and infertility. Human Reproduction 20, 1144–1147. https://doi.org/10.1093/humrep/deh870
28. Gu, Z., Eils, R., Schlesner, M., 2016. Complex heatmaps reveal patterns and correlations in multidimensional genomic data. Bioinformatics 32, 2847–2849. https://doi.org/10.1093/bioinformatics/btw313
29. Gunes, S., Sengupta, P., Henkel, R., Alguraigari, A., Sinigaglia, M.M., Kayal, M., Joumah, A., Agarwal, A., 2020. Microtubular dysfunction and male infertility. World Journal of Men's Health. https://doi.org/10.5534/wjmh.180066
30. Hahn-Windgassen, A., Nogueira, V., Chen, C.C., Skeen, J.E., Sonenberg, N., Hay, N., 2005. Akt activates the mammalian target of rapamycin by regulating cellular ATP level

and AMPK activity. Journal of Biological Chemistry. https://doi.org/10.1074/jbc.M502876200

31. Hamasaki, M., Shibutani, S.T., Yoshimori, T., 2013. Up-to-date membrane biogenesis in the autophagosome formation. Current Opinion in Cell Biology. https://doi.org/10.1016/j.ceb.2013.03.004
32. Hara, Y., Yamagata, K., Oguchi, K., Baba, T., 2008. Nuclear localization of profilin III-ArpM1 complex in mouse spermiogenesis. FEBS Letters. https://doi.org/10.1016/j.febslet.2008.07.058
33. Hirsh, A. 2003. Male subfertility. BMJ. 327:1165a. doi:10.1136/bmj.327.7416.669.
34. Huang, Q., Liu, Y., Zhang, S., Yap, Y.T., Li, W., Zhang, D., Gardner, A., Zhang, L., Song, S., Hess, R.A., Zhang, Z., 2020. Autophagy core protein ATG5 is required for elongating spermatid development, sperm individualization and normal fertility in male mice. Autophagy. https://doi.org/10.1080/15548627.2020.1783822
35. Huang, Y., Ma, T., Lau, P.K., Wang, J., Zhao, T., Du, S., Loy, M.M.T., Guo, Y., 2019. Visualization of Protein Sorting at the Trans-Golgi Network and Endosomes Through Super-Resolution Imaging. Frontiers in Cell and Developmental Biology 7, 1–13. https://doi.org/10.3389/fcell.2019.00181
36. Huber, W., von Heydebreck, A., Ultmann, H.S.¨, Poustka, A., Vingron, M., 2002. Variance stabilization applied to microarray data calibration and to the quantification of differential expression, BIOINFORMATICS.
37. Ikawa, M., Inoue, N., Benham, A.M., Okabe, M., 2010. Fertilization: A sperm's journey to and interaction with the oocyte. Journal of Clinical Investigation. https://doi.org/10.1172/JCI41585
38. Kanatsu-Shinohara, M., Takehashi, M., Takashima, S., Lee, J., Morimoto, H., Chuma, S., Raducanu, A., Nakatsuji, N., Fässler, R. and Shinohara, T., 2008. Homing of Mouse Spermatogonial Stem Cells to Germline Niche Depends on β1-Integrin. *Cell Stem Cell*, 3(5), pp.533–542. https://doi.org/10.1016/j.stem.2008.08.002.
39. Kazarian, E., Son, H.Y., Sapao, P., Li, W., Zhang, Z., Strauss, J.F., Teves, M.E., 2018. SPAG17 is required for male germ cell differentiation and fertility. International Journal of Molecular Sciences 19. https://doi.org/10.3390/ijms19041252
40. Kierszenbaum, Abraham L., Tres, L.L., 2004. The acrosome-acroplaxome-manchette complex and the shaping of the spermatid head. Archives of Histology and Cytology 67, 271–284. https://doi.org/10.1679/aohc.67.271

41. Kim, D., Langmead, B., Salzberg, S.L., 2015. HISAT: A fast spliced aligner with low memory requirements. Nature Methods. https://doi.org/10.1038/nmeth.3317
42. Kim, K. S., Cha, M. C., & Gerton, G. L. 2001. Mouse sperm protein sp56 is a component of the acrosomal matrix. *Biology of reproduction*, *64*(1), 36–43. https://doi.org/10.1095/biolreprod64.1.36
43. Krausz, C., Chianese, C., Giachini, C., Guarducci, E., Laface, I., Forti, G., 2011. The Y chromosome-linked copy number variations and male fertility. Journal of Endocrinological Investigation. https://doi.org/10.3275/7612
44. Lepelley, A., Martin-Niclós, M.J., Bihan, M. le, Marsh, J.A., Uggenti, C., Rice, G.I., Bondet, V., Duffy, D., Hertzog, J., Rehwinkel, J., Amselem, S., Khalifi, S.B. el, Brennan, M., Carter, E., Chatenoud, L., Chhun, S., L'Hermine, A.C., Depp, M., Legendre, M., MacKenzie, K.J., Marey, J., McDougall, C., McKenzie, K.J., Molina, T.J., Neven, B., Seabra, L., Thumerelle, C., Wislez, M., Nathan, N., Manel, N., Crow, Y.J. and Frémond, M.L., 2020. Mutations in COPA lead to abnormal trafficking of STING to the Golgi and interferon signaling. *Journal of Experimental Medicine*, 217(11).
45. Lê, S., Josse, J., Husson, F., 2008. FactoMineR: An R package for multivariate analysis. Journal of Statistical Software 25, 1–18. https://doi.org/10.18637/jss.v025.i01
46. LEBLOND, C.P., CLERMONT, Y., 1952. Definition of the stages of the cycle of the seminiferous epithelium in the rat. Annals of the New York Academy of Sciences 55, 548–573. https://doi.org/10.1111/j.1749-6632.1952.tb26576.x
47. Lehti, M.S., Kotaja, N., Sironen, A., 2013. KIF3A is essential for sperm tail formation and manchette function. Molecular and Cellular Endocrinology. https://doi.org/10.1016/j.mce.2013.06.030
48. Lehti, M.S., Sironen, A., 2017. Formation and function of sperm tail structures in association with sperm motility defects. Biology of Reproduction 97, 522–536. https://doi.org/10.1093/biolre/iox096
49. Lehti, M.S., Zhang, F.-P., Kotaja, N., Sironen, A., 2017. SPEF2 functions in microtubule-mediated transport in elongating spermatids to ensure proper male germ cell differentiation. Journal of Cell Science 130, e1.2-e1.2. https://doi.org/10.1242/jcs.208710
50. Levine, H., Jørgensen, N., Martino-Andrade, A., Mendiola, J., Weksler-Derri, D., Mindlis, I., Pinotti, R., Swan, S.H., 2017. Temporal trends in sperm count: A systematic review and meta-regression analysis. Human Reproduction Update 23, 646–659. https://doi.org/10.1093/humupd/dmx022

51. Li, J., Qi, W., Chen, G., Feng, D., Liu, J., Ma, B., Zhou, C., Mu, C., Zhang, W., Chen, Q., Zhu, Y., 2015. Mitochondrial outer-membrane E3 ligase MUL1 ubiquitinates ULK1 and regulates selenite-induced mitophagy. Autophagy. https://doi.org/10.1080/15548627.2015.1017180
52. Li, W., Tang, W., Teves, M.E., Zhang, Z., Zhang, L., Li, H., Archer, K.J., Peterson, D.L., Williams, D.C., Strauss, J.F. and Zhang, Z., 2015. A MEIG1/PACRG complex in the manchette is essential for building the sperm flagella. *Development (Cambridge)*, 142(5), pp.921–930. https://doi.org/10.1242/dev.119834.
53. Li, W., Zhang, Y., Zhang, L., Tevesb, M.E., Liu, H., Strauss, J.F., Pazour, G.J., Foster, J.A., Hess, R.A., Zhang, Zhibing, Zhang, Zhengang, 2016. Intraflagellar transport protein IFT20 is essential for male fertility and spermiogenesis in mice. Molecular Biology of the Cell 27, 3705–3716. https://doi.org/10.1091/mbc.E16-05-0318
54. Li, Y., Liu, R., Wu, J., & Li, X., 2020. Self-eating: friend or foe? The emerging role of autophagy in fibrotic diseases. *Theranostics*, *10*(18), 7993–8017. https://doi.org/10.7150/thno.47826
55. Liang, P., Jiang, B., Li, Y., Liu, Z., Zhang, P., Zhang, M., Huang, X., Xiao, X., 2018. Autophagy promotes angiogenesis via AMPK/Akt/mTOR signaling during the recovery of heat-denatured endothelial cells. Cell Death and Disease. https://doi.org/10.1038/s41419-018-1194-5
56. Liu, C., Song, Z., Wang, L., Yu, H., Liu, W., Shang, Y., Xu, Z., Zhao, H., Gao, Fengyi, Wen, J., Zhao, L., Gui, Y., Jiao, J., Gao, Fei, Li, W., 2017. Sirt1 regulates acrosome biogenesis by modulating autophagic flux during spermiogenesis in mice. Development (Cambridge). https://doi.org/10.1242/dev.147074
57. Liu, Y., DeBoer, K., de Kretser, D.M., O'Donnell, L., O'Connor, A.E., Merriner, D.J., Okuda, H., Whittle, B., Jans, D.A., Efthymiadis, A., McLachlan, R.I., Ormandy, C.J., Goodnow, C.C., Jamsai, D. and O'Bryan, M.K., 2015. LRGUK-1 Is Required for Basal Body and Manchette Function during Spermatogenesis and Male Fertility. *PLoS Genetics*, 11(3). https://doi.org/10.1371/journal.pgen.1005090.
58. Long, F.J., Cook, S., 1991. Formation of the Perinuclear Theca in Spermatozoa of Diverse Mammalian Species: Relationship of the Manchette and Multiple Band Polypeptides, MOLECULAR REPRODUCTION AND DEVELOPMENT.
59. Lotti, F., Maggi, M., 2018. Sexual dysfunction and male infertility. Nature Reviews Urology. https://doi.org/10.1038/nrurol.2018.20

60. Love, M.I., Huber, W., Anders, S., 2014. Moderated estimation of fold change and dispersion for RNA-seq data with DESeq2. Genome Biology. https://doi.org/10.1186/s13059-014-0550-8
61. Manolea, F., Chun, J., Chen, D.W., Clarke, I., Summerfeldt, N., Dacks, J.B., Melançon, P., 2010. Arf3 Is Activated Uniquely at the trans-Golgi Network by Brefeldin A-inhibited Guanine Nucleotide Exchange Factors. Molecular Biology of the Cell 21, 1836–1849. https://doi.org/10.1091/mbc.E10
62. Martínez-Menárguez, J.A., Geuze, H.J., Ballesta, J., 1996. Evidence for a nonlysosomal origin of the acrosome. Journal of Histochemistry and Cytochemistry 44, 313–320. https://doi.org/10.1177/44.4.8601690
63. Mashiko, D., Fujihara, Y., Satouh, Y., Miyata, H., Isotani, A., Ikawa, M., 2013. Generation of mutant mice by pronuclear injection of circular plasmid expressing Cas9 and single guided RNA. Scientific Reports 3. https://doi.org/10.1038/srep03355
64. Mellacheruvu, D., Wright, Z., Couzens, A.L., Lambert, J.P., St-Denis, N.A., Li, T., Miteva, Y. v., Hauri, S., Sardiu, M.E., Low, T.Y., Halim, V.A., Bagshaw, R.D., Hubner, N.C., Al-Hakim, A., Bouchard, A., Faubert, D., Fermin, D., Dunham, W.H., Goudreault, M., Lin, Z.Y., Badillo, B.G., Pawson, T., Durocher, D., Coulombe, B., Aebersold, R., Superti-Furga, G., Colinge, J., Heck, A.J.R., Choi, H., Gstaiger, M., Mohammed, S., Cristea, I.M., Bennett, K.L., Washburn, M.P., Raught, B., Ewing, R.M., Gingras, A.C., Nesvizhskii, A.I., 2013. The CRAPome: A contaminant repository for affinity purification-mass spectrometry data. Nature Methods 10, 730–736. https://doi.org/10.1038/nmeth.2557
65. Mendoza-Lujambio, I., Burfeind, P., Dixkens, C., Meinhardt, A., Hoyer-Fender, S., Engel, W. and Neesen, J., 2002. The Hook1 gene is non-functional in the abnormal spermatozoon head shape (azh) mutant mouse. *Human Molecular Genetics*, 11(14), pp.1647–1658. https://doi.org/10.1093/hmg/11.14.1647.
66. Miyamoto, T., Tsujimura, A., Miyagawa, Y., Koh, E., Namiki, M., Sengoku, K., 2012. Male Infertility and Its Causes in Human. Advances in Urology. https://doi.org/10.1155/2012/384520
67. Mizushima, N., Levine, B., 2010. Autophagy in mammalian development and differentiation. Nature Cell Biology. https://doi.org/10.1038/ncb0910-823
68. Mizushima, N., Yoshimori, T., Ohsumi, Y., 2011. The role of atg proteins in autophagosome formation. Annual Review of Cell and Developmental Biology 27, 107–132. https://doi.org/10.1146/annurev-cellbio-092910-154005

69. Mochida, K., Tres, L.L. and Kierszenbaum, A.L., 1991. *Structural and Biochemical Features of Fractionated Spermatid Manchettes and Sperm Axonemes of the Azh/Azh Mutant Mouse*.
70. Moreno, R. D., & Schatten, G., 2000. Microtubule configurations and post-translational alpha-tubulin modifications during mammalian spermatogenesis. *Cell motility and the cytoskeleton*, *46*(4), 235–246. https://doi.org/10.1002/1097-0169(200008)46:4<235::AID-CM1>3.0.CO;2
71. Nishimura, H., L'Hernault, S.W., 2017. Spermatogenesis. Current Biology. https://doi.org/10.1016/j.cub.2017.07.067
72. OAKBERG E. F., 1956. Duration of spermatogenesis in the mouse and timing of stages of the cycle of the seminiferous epithelium. *The American journal of anatomy*, *99*(3), 507–516. https://doi.org/10.1002/aja.1000990307
73. Obermann, H., Raabe, I., Balvers, M., Brunswig, B., Schulze, W., Kirchhoff, C., 2005. Novel testis-expressed profilin IV associated with acrosome biogenesis and spermatid elongation. Molecular Human Reproduction 11, 53–64. https://doi.org/10.1093/molehr/gah132
74. O'Donnell, L., Rhodes, D., Smith, S.J., Merriner, D.J., Clark, B.J., Borg, C., Whittle, B., O'Connor, A.E., Smith, L.B., McNally, F.J., de Kretser, D.M., Goodnow, C.C., Ormandy, C.J., Jamsai, D., O'Bryan, M.K., 2012. An essential role for Katanin p80 and microtubule severing in male gamete production. PLoS Genetics 8. https://doi.org/10.1371/journal.pgen.1002698
75. Okuda, H., DeBoer, K., O'Connor, A.E., Merriner, D.J., Jamsai, D., O'Bryan, M.K., 2017. LRGUK1 is part of a multiprotein complex required for manchette function and male fertility. FASEB Journal. https://doi.org/10.1096/fj.201600909R
76. Pertea, M., Pertea, G.M., Antonescu, C.M., Chang, T.C., Mendell, J.T., Salzberg, S.L., 2015. StringTie enables improved reconstruction of a transcriptome from RNA-seq reads. Nature Biotechnology. https://doi.org/10.1038/nbt.3122
77. Plachot, M., Belaisch-Allart, J., Mayenga, J.-M., Chouraqui, A., Tesquier, L., Serkine, A.M., 2002. Outcome of conventional IVF and ICSI on sibling oocytes in mild male factor infertility, Human Reproduction.
78. Qin, W., Dion, S.L., Kutny, P.M., Zhang, Y., Cheng, A.W., Jillette, N.L., Malhotra, A., Geurts, A.M., Chen, Y.G., Wang, H., 2015. Efficient CRISPR/cas9-mediated genome editing in mice by zygote electroporation of nuclease. Genetics 200, 423–430. https://doi.org/10.1534/genetics.115.176594

79. Qi, Y., Jiang, M., Yuan, Y., Bi, Y., Zheng, B., Guo, X., Huang, X., Zhou, Z. and Sha, J., 2013. Adp-ribosylation factor-like 3, a manchette-associated protein, is essential for mouse spermiogenesis. *Molecular Human Reproduction*, 19(5), pp.327–335. https://doi.org/10.1093/molehr/gat001.
80. Ramalho-Santos, J., Schatten, G., Moreno, R.D., 2002. M i n i rev i ew Control of Membrane Fusion During Spermiogenesis and the Acrosome Reaction 1. BIOLOGY OF REPRODUCTION 67, 1043–1051. https://doi.org/10.1095/biolreprod.102.005967
81. Rato, L., Alves, M.G., Socorro, S., Duarte, A.I., Cavaco, J.E., Oliveira, P.F., 2012. Metabolic regulation is important for spermatogenesis. Nature Reviews Urology. https://doi.org/10.1038/nrurol.2012.77
82. Ritchie, M.E., Phipson, B., Wu, D., Hu, Y., Law, C.W., Shi, W., Smyth, G.K., 2015. Limma powers differential expression analyses for RNA-sequencing and microarray studies. Nucleic Acids Research 43, e47. https://doi.org/10.1093/nar/gkv007
83. Russell, L.D., Russell, J.A., MacGregor, G.R., Meistrich, M.L., 1991. Linkage of manchette microtubules to the nuclear envelope and observations of the role of the manchette in nuclear shaping during spermiogenesis in rodents. American Journal of Anatomy 192, 97–120. https://doi.org/10.1002/aja.1001920202
84. Shang, Y., Wang, H., Jia, P., Zhao, H., Liu, C., Liu, W., Song, Z., Xu, Z., Yang, L., Wang, Y., Li, W., 2016. Autophagy regulates spermatid differentiation via degradation of PDLIM1. Autophagy 12, 1575–1592. https://doi.org/10.1080/15548627.2016.1192750
85. Schwarz, T., Prieler, B., Schmid, J.A., Grzmil, P. and Neesen, J., 2017. Ccdc181 is a microtubule-binding protein that interacts with Hook1 in haploid male germ cells and localizes to the sperm tail and motile cilia. *European Journal of Cell Biology*, 96(3), pp.276–288. https://doi.org/10.1016/j.ejcb.2017.02.003.
86. Shen, Y., Zhang, F., Li, F., Jiang, X., Yang, Y., Li, X., Li, W., Wang, X., Cheng, J., Liu, M., Zhang, X., Yuan, G., Pei, X., Cai, K., Hu, F., Sun, J., Yan, L., Tang, L., Jiang, C., Tu, W., Xu, J., Wu, H., Kong, W., Li, S., Wang, K., Sheng, K., Zhao, X., Yue, H., Yang, X., Xu, W., 2019. Loss-of-function mutations in QRICH2 cause male infertility with multiple morphological abnormalities of the sperm flagella. Nature Communications. https://doi.org/10.1038/s41467-018-08182-x
87. Skinner, B. M., Rathje, C. C., Bacon, J., Johnson, E. E. P., Larson, E. L., Kopania, E. E. K., Good, J. M., Yousafzai, G., Affara, N. A., & Ellis, P. J. I., 2019. A high-throughput method for unbiased quantitation and categorization of nuclear morphology. *Biology of Reproduction*. doi: 10.1093/biolre/ioz013

88. Sleutels, F., Soochit, W., Bartkuhn, M., Heath, H., Dienstbach, S., Bergmaier, P., Franke, V., Rosa-Garrido, M., Van De Nobelen, S., Caesar, L., Van Der Reijden, M., Bryne, J.C., Van Ijcken, W., Grootegoed, J.A., Delgado, M.D., Lenhard, B., Renkawitz, R., Grosveld, F., Galjart, N., 2012. The male germ cell gene regulator CTCFL is functionally different from CTCF and binds CTCF-like consensus sites in a nucleosome composition-dependent manner. Epigenetics and Chromatin. https://doi.org/10.1186/1756-8935-5-8
89. Sun, T.T., Chung, C.M., Chan, H.C., 2011. Acrosome reaction in the cumulus oophorus revisited: Involvement of a novel sperm-released factor NYD-SP8. Protein and Cell. https://doi.org/10.1007/s13238-011-1022-5
90. Tang, F.L., Liu, W., Hu, J.X., Erion, J.R., Ye, J., Mei, L., Xiong, W.C., 2015. VPS35 Deficiency or Mutation Causes Dopaminergic Neuronal Loss by Impairing Mitochondrial Fusion and Function. Cell Reports. https://doi.org/10.1016/j.celrep.2015.08.001
91. Tang, X.M., Lalli, M.F., Clermont, Y., 1982. A cytochemical study of the Golgi apparatus of the spermatid during spermiogenesis in the rat. The American journal of anatomy 163, 283–294. https://doi.org/10.1002/aja.1001630402
92. Tang, Z., Takahashi, Y., Chen, C., Liu, Y., He, H., Tsotakos, N., Serfass, J.M., Gebru, M.T., Chen, H., Young, M.M., Wang, H.G., 2017. Atg2A/B deficiency switches cytoprotective autophagy to non-canonical caspase-8 activation and apoptosis. Cell Death and Differentiation. https://doi.org/10.1038/cdd.2017.133
93. Teves, M. E., Roldan, E., Krapf, D., Strauss, J. F., III, Bhagat, V., & Sapao, P., 2020. Sperm Differentiation: The Role of Trafficking of Proteins. *International journal of molecular sciences*, *21*(10), 3702. https://doi.org/10.3390/ijms21103702
94. The, M., MacCoss, M.J., Noble, W.S., Käll, L., 2016. Fast and Accurate Protein False Discovery Rates on Large-Scale Proteomics Data Sets with Percolator 3.0. Journal of the American Society for Mass Spectrometry 27, 1719–1727. https://doi.org/10.1007/s13361-016-1460-7
95. Theriot', J.A., Mitchisont, T.J., 1993. The Three Faces of Profilin, Cell.
96. Theriot, J.A., Rosenblatt, J., Portnoy, D.A., Goldschmidt-Clermont, P.J., Mitchisont, T.J., 1994. Involvement of Profilin in the Actin-Based Motility of L. monocytogenes in Cells and in Cell-Free Extracts, Cell.
97. Tiwari, N., Graham, M., Liu, X., Yue, X., Zhu, L., Meshram, D., Choi, S., Qian, Y., Rothman, J.E., Lee, I., 2019. Golgin45-Syntaxin5 Interaction Contributes to Structural Integrity of the Golgi Stack. Scientific Reports. https://doi.org/10.1038/s41598-019-48875-x

98. Tolahunase, M., Sagar, R., Dada, R., 2017. Impact of Yoga and Meditation on Cellular Aging in Apparently Healthy Individuals: A Prospective, Open-Label Single-Arm Exploratory Study. Oxidative Medicine and Cellular Longevity 2017. https://doi.org/10.1155/2017/7928981

99. Tourmente, M., Villar-Moya, P., Rial, E., Roldan, E.R.S., 2015. Differences in ATP generation via glycolysis and oxidative phosphorylation and relationships with sperm motility in mouse species. Journal of Biological Chemistry. https://doi.org/10.1074/jbc.M115.664813

100. Umer, N., Arévalo, L., Phadke, S., Lohanadan, K., Kirfel, G., Sons, D., Sofia, D., Witke, W., Schorle, H., 2021. Loss of Profilin3 Impairs Spermiogenesis by Affecting Acrosome Biogenesis, Autophagy, Manchette Development and Mitochondrial Organization. Frontiers in Cell and Developmental Biology 9. https://doi.org/10.3389/fcell.2021.749559

101. Wang, H., Wan, H., Li, X., Liu, W., Chen, Q., Wang, Y., Yang, L., Tang, H., Zhang, X., Duan, E., Zhao, X., Gao, F., Li, W., 2014. Atg7 is required for acrosome biogenesis during spermatogenesis in mice. Cell Research. https://doi.org/10.1038/cr.2014.70

102. Wickstead, B., Gull, K., 2011. The evolution of the cytoskeleton. Journal of Cell Biology. https://doi.org/10.1083/jcb.201102065

103. Wilson, N.R., Olm-Shipman, A.J., Acevedo, D.S., Palaniyandi, K., Hall, E.G., Kosa, E., Stumpff, K.M., Smith, G.J., Pitstick, L., Liao, E.C., Bjork, B.C., Czirok, A., Saadi, I., 2016. SPECC1L deficiency results in increased adherens junction stability and reduced cranial neural crest cell delamination. Scientific Reports 6. https://doi.org/10.1038/srep17735

104. Wioland, H., Guichard, B., Senju, Y., Myram, S., Lappalainen, P., Jégou, A., Romet-Lemonne, G., 2017. ADF/Cofilin Accelerates Actin Dynamics by Severing Filaments and Promoting Their Depolymerization at Both Ends. Current Biology 27, 1956-1967.e7. https://doi.org/10.1016/j.cub.2017.05.048

105. Wu, A.T.H., Sutovsky, P., Xu, W., van der Spoel, A.C., Platt, F.M., Oko, R., 2007. The postacrosomal assembly of sperm head protein, PAWP, is independent of acrosome formation and dependent on microtubular manchette transport. Developmental Biology 312, 471–483. https://doi.org/10.1016/j.ydbio.2007.08.051

106. Xin, A., Qu, R., Chen, G., Zhang, L., Chen, J., Tao, C., Fu, J., Tang, J., Ru, Y., Chen, Y., Peng, X., Shi, H., Zhang, F., & Sun, X., 2020. Disruption in *ACTL7A* causes acrosomal ultrastructural defects in human and mouse sperm as a novel male factor inducing early

embryonic arrest. *Science advances*, *6*(35), eaaz4796. https://doi.org/10.1126/sciadv.aaz4796

107. Xin, Y., Wang, Y., Zhong, L., Shi, B., Liang, H., Han, J., 2019. Slc25a36 modulates pluripotency of mouse embryonic stem cells by regulating mitochondrial function and glutathione level. Biochemical Journal. https://doi.org/10.1042/BCJ20190057
108. Xiao, N., Kam, C., Shen, C., Jin, W., Wang, J., Lee, K. M., Jiang, L., & Xia, J. 2009. PICK1 deficiency causes male infertility in mice by disrupting acrosome formation. *The Journal of clinical investigation*, *119*(4), 802–812. https://doi.org/10.1172/JCI36230
109. Xu, F., Na, L., Li, Y., Chen, L., 2020. Roles of the PI3K/AKT/mTOR signalling pathways in neurodegenerative diseases and tumours. Cell and Bioscience. https://doi.org/10.1186/s13578-020-00416-0
110. Yang, H., Wang, H., Jaenisch, R., 2014. Generating genetically modified mice using CRISPR/Cas-mediated genome engineering. Nature protocols 9, 1956–1968. https://doi.org/10.1038/nprot.2014.134
111. Yao, R., Ito, C., Natsume, Y., Sugitani, Y., Yamanaka, H., Kuretake, S., Yanagida, K., Sato, A., Toshimori, K., Noda, T. and Simons, K., 2002. *Lack of acrosome formation in mice lacking a Golgi protein, GOPC*. [online] Available at: <www.pnas.orgcgidoi10.1073pnas.162027899>.
112. Yefimova, M., Buschiazzo, A., Burel, A., Lavault, M.T., Pimentel, C., Jouve, G., Jaillard, S., Jegou, B., Bourmeyster, N., Ravel, C., 2019. Autophagy is increased in cryptorchid testis resulting in abnormal spermatozoa. Asian Journal of Andrology. https://doi.org/10.4103/aja.aja_12_19
113. Zhang, Y., Feng, Y., Ji, D., Wang, Q., Qian, W., Wang, S., Zhang, Z., Ji, B., Zhang, C., Sun, Y., Fu, Z., 2018. TRIM27 functions as an oncogene by activating epithelial-mesenchymal transition and p-AKT in colorectal cancer. International Journal of Oncology. https://doi.org/10.3892/ijo.2018.440